POLITECNICO DI TORINO
Repository ISTITUZIONALE

Bubble dynamics in liquid metals under external magnetic field

(Article begins on next page)

19 April 2024

Bubble dynamics in liquid metals under external magnetic field

Master Thesis

Marino Corrado

August 16, 2021

Academic supervisor: Prof. Dr. Horst-Michael Prasser at ETH Zürich

Supervisor: Dr. Yohei Sato at PSI

Abstract

In this study, Computational Fluid Dynamics (CFD) simulation was used to derive full understanding of a bubble rising in liquid metals with and without the presence of an external magnetic field. The major aim of the study was to develop new correlations for bubble velocity and bubble deformation in liquid metals.

In house code PSI-BOIL has been used for the simulations. Single bubble rising in quiescent liquid is simulated for three different set of materials (Nitrogen+Mercury, Argon+GaInSn, Argon+Steel). The influence of external horizontal magnetic field on bubble dynamics is analyzed, vertical magnetic field is not considered in this study.

On overall, the computed results show that horizontal magnetic field reduces bubble rising velocity, straightens the bubble trajectory and enhances bubble interface stability.

Acknowledgements

I would like to thank my supervisor Dr. Yohei Sato for his guidance and help throughout this master project. His advice and assistance helped me to tackle the various encountered challenges of computational multiphase flow dynamics.

I would also like to thank Prof. Dr. H.M. Prasser for assuming the role of the responsible teacher at ETH and taking part in the corresponding administrative matters.

Finally, I want to deeply thank my family and my friends for their help and support during all my university studies.

Contents

Nomenclature

B [T]   magnetic field

c [m/s]   velocity of light

E [V/m]   electric field

Eo [−]   Eotvos number

g [m/s^2]   gravitational acceleration

J [A/m^2]   electric current density

Mo [−]   Morton number

N [−]   Stuart number

p [Pa]   pressure

Re [−]   Reynolds number

t [s]   time

u [m/s]   velocity

We [−]   Weber number

X [−]   bubble aspect ratio

γ [N/m]   surface tension coefficient

ε [F/m]   electrical permittivity

μ [Pa$\cdot$s]   dynamic viscosity

μ_B [H/m]   magnetic permeability

ρ [kg/m^3]   density

σ [1/$\Omega\cdot$m]   electric conductivity

ϕ [V]   electric potential

χ [1/m]   bubble local curvature

1 Introduction

Bubble motion in liquid metals plays a determining role in many engineering processes. In fact, liquid metal is an excellent type of energy carrier and it is largely used in many nuclear reactors type such as fast reactors, spallation source devices and fusion reactors. Gas bubbles are commonly inserted in the liquid metal to improve the heat transfer of the liquid and to enhance the mixing process that takes place in the liquid phase.

Bubbly flow in liquid metal is widely used in industrial processes such as metal stirring and purification, continuum casting and liquid metal chemical reactions with the purpose to increase the efficiency. Plenty of the scientific research has been carried out in this field. In continuum casting, for example, bubbles are injected in the liquid metal in order to avoid clogging of the flow and make the process more continuum as possible. Furthermore, it has been demonstrated that the application of an external magnetic field, B_{ext}, in the liquid metal environmental strongly influence the dynamics of bubble motion. Under the right condition, a proper application of B_{ext} can stabilize the bubbly flow and enhances the process.

Bubble flow in liquid metal under strong external magnetic field is also an opening issues in the TOKAMAK fusion reactor. Here, the presence of $B_{ext} = 6\sim8$ T suppresses the turbulence behavior of the cooling flow reducing drastically the heat transfer. Bubble are so injected in order to increase the mixing of the liquid and counterbalance B_{ext} effect, increasing the heat transfer. The most promising blanket also uses a bi-phase flow of liquid lithium and helium bubble. The tritium is produced by neutron irradiation of the lithium and it is carried out by helium bubbles.

Because of its innumerable industrial applications, bubble motion in liquid metal has been a central topic for the scientific community in the past 70 years. Nevertheless, important questions still remain unclear and the bubble rising problem remain an open issue in multi-phase fluid mechanics.

1.1 Rising bubble in liquid metal without magnetic field

Bubble rising in quiescent liquid is a well-known problem in multiphase-fluid mechanics. From the dimensionless analysis of the problem, it has been found out that the system is characterized by three dimensionless numbers. In literature the most common used are: Reynolds number $\left(Re = \dfrac{\rho \cdot u \cdot D}{\mu} \right)$, Eotvos number $\left(Eo = \dfrac{\Delta\rho \cdot g \cdot D^2}{\gamma} \right)$ and Morton number $\left(Mo = \dfrac{g \cdot \mu_c^4 \cdot \Delta\rho}{\rho_c^2 \cdot \gamma^3} \right)$. By the bubble balance

equation, it has been found that these three numbers are correlated $F\left(\Pi_{1},\Pi_{2},\Pi_{3}\right)=0$. The whole system is therefore fully characterize by only a combination of two of them.

Correlations between these numbers have been produced in literature for wide range of Eotvos and Reynolds numbers, while a universal correlation is not been found yet. Nevertheless, many correlations, valid in their own ranges, have been derived or produced in the past.

Levich [1] analytically derived a drag coefficient valid Eq. (1.1) for enough inviscid flow ($\mu \to 0$) for spherical bubble ($X \to 1$) in which the viscous component for the drag force is negligible (high Re).

$$C_{\mathrm{D}} = \frac{48}{Re}$$

(1.1)

For creepy flow ($Re < 1, X \to 1$) Hadamart [2] derived a drag coefficient as Eq. (1.2), considering the pressure component by the wake negligible.

$$C_{\mathrm{D}} = \frac{16}{Re}$$

(1.2)

Mei and Klausner [3] extended Hadamart correlation for spherical bubble at arbitrary Reynolds number.

$$C_{D} = \frac{16}{Re} \cdot \left[1 + \left(\frac{8}{Re} + \frac{1}{2}\left(1 + 3.315 Re^{-0.5}\right) \right)^{-1} \right]$$

(1.3)

Mendelson [4] studied the bubble rising problem in inviscid liquid and approximates the bubble velocity to the propagation wave velocity of the gas-liquid interface. The phase velocity c_{phase} is assumed to be the sum of the velocity resulting from the surface tension and the gravitational term.

$$c_{phase}{}^{2} = \frac{2\pi\gamma}{\rho\lambda} + \frac{\left(\rho_{l} - \rho_{g}\right)g\lambda}{2\pi\rho_{l}}$$

(1.4)

By determining that the principal wavelength $\lambda = \pi d$, he computed the bubble rising velocity.

$$u = \sqrt{\frac{2\gamma}{\rho_{l}D} + \frac{\Delta\rho g D}{2\rho_{l}}}$$

(1.5)

Tomiyama [3] generalized the drag correlation for a wide range, ($10^{-2} < Eo < 10^{3}$, $10^{-14} < Mo < 10^{7}$, $10^{-3} < Re < 10^{5}$) providing the most general correlation possible. First, he unified Levich and Hadamart correlation for a wide range of Reynolds number.

$$C_D = \min\left[\frac{16}{Re}\left(1 + 0.15\,Re^{0.687}\right), \frac{48}{Re}\right] \tag{1.6}$$

Secondly, he calculated the drag coefficient using Mendelson theory providing a drag coefficient dependent only on the initial conditions.

$$C_D = \frac{8}{3}\cdot\frac{Eo}{Eo + 4} \tag{1.7}$$

Since for higher Eotvos the bubble tends to be not spherical anymore but ellipsoidal, the terminal velocity will be lower than a spherical case. Taking into account this effect, the maximum of the two drag coefficients is considered.

$$C_D = \max\left\{\min\left[\frac{16}{Re}\left(1 + 0.15\,\mathrm{Re}^{0.687}\right), \frac{48}{Re}\right], \frac{8}{3}\cdot\frac{Eo}{Eo + 4}\right\} \tag{1.8}$$

The main issue in finding a universal correlation is the big scale of change of the dimensionless numbers (*Re*, *Eo*, *Mo*) of several order of magnitudes. In each region in the Grace diagram, the viscous, inertia and tension forces have different importance and the bubble behavior is strongly changed. Thanks to experiment and CFD simulations, a map has been created which predicts the terminal Reynolds number, knowing the initial conditions. Generally, the bubble terminal Reynolds number increases with Eotvos number and decreases with Morton number.

As it can be seen in Figure 1 the liquid metal is a region in which not a universal correlation has been found yet. The main obstacle is the opacity of the metal that makes optical inspection of the bubble almost impossible. In the past, techniques such as the electrical triple probe [5] have been adopted to determine bubble rising velocity. Nevertheless, due to the instrumentations inaccuracies, bubble velocity was not able to be precisely predicted but only overall estimates could be done. Modern techniques as UDV (Ultrasound Doppler Velocimetry) and Neutron tomography [6] seem to be the best tool to experimentally investigate in this environment. Since today, experiments have been insufficient to produce a robust correlation for the bubble rising velocity u_∞ and aspect ratio X in liquid metals. These modern techniques manage to have a much higher accuracy in detecting the bubble velocity and shape compared to old-fashion ones but they still turn out to be expensive and their use is somewhat limited.
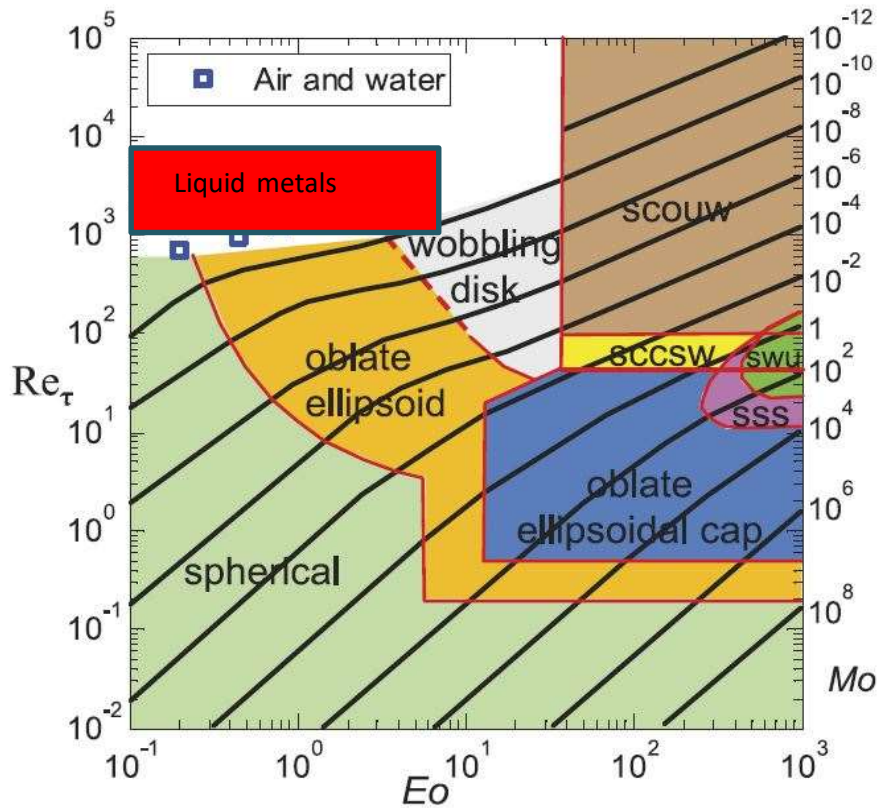
Figure 1 "Grace diagram.[7] Bubble shape: scouw—spherical cap with open unsteady wake sccsw—spherical cap with closed steady wake; swu—skirt with wavy unsteady skirt; sss—skirt with smooth steady skirt."

1.2 Rising bubble in liquid metal under external magnetic field

Rising bubble in liquid metal under the presence of an external magnetic field is relatively new research topic compared to a bubble in water, thus the phenomena are not fully understood in the scientific community mainly because of the difficulty of optical measurement due to opacity of liquid metal. Nevertheless, several researches have been conducted in the past.

Mori et al. [5] report experimental results of a single nitrogen bubble rising in quiescent mercury under a horizontal magnetic field using the electrical triple probe method. For strong magnetic field ($B >$ 1.5 T) bubble velocity is decreased for all bubble sizes. For small bubble ($D = 2$mm), a weak horizontal magnetic field ($B < 0.5$ T) increases the rising velocity which was considered to be caused by the suppression of spiral trajectory of bubble due to the magnetic field.

Zhang et al. [8]&[9] experimentally studied a single bubble rise in quiescent liquid metal using UDV technique (Ultrasound Doppler Velocimetry). The applied vertical magnetic field was varied up to

0.3 T, corresponding to a magnetic interaction parameter $N\left(=\dfrac{B^2 \cdot D \cdot \sigma}{\rho \cdot u}\right)$ equals to unity. It was observed that the drag coefficient is increased by the magnetic field for small bubble ($D \leq 4.6$ mm) but reduced for large bubble ($D > 4.6$ mm).

Shibasaki et al. [10] simulated single bubble rising in quiescent liquid metal under vertical magnetic field, and found good agreement with Zhang et al. measurement. The bubble rising velocity is mainly controlled by the Hartmann number. For $0 < Ha < 75$ $\left(Ha = B \cdot D \cdot \sqrt{\dfrac{\sigma}{\mu}}\right)$ the magnetic field increased the rising velocity, while for $Ha > 75$ the bubble velocity was decreased by the magnetic field. Furthermore it was shown that the flow field is considerably different compared to a conventional bubble rising problem without magnetic field.

Zhang and Ni [11] performed a direct numerical simulation of an argon bubble rising in quiescent liquid metal, GaInSn, under the presence of a vertical magnetic field. It was discovered that magnetic field has a non-monotonic influence on the bubble rising velocity. A moderate magnetic field increases the velocity, while a strong one leads to a reduction of the velocity. Therefore, there is an optimum magnetic field that can maximize the bubble velocity, and it depends on bubble diameter. Generally, this non-monotonic change takes place at lower magnetic field for smaller bubble.

Jin at al.[7] performed a CFD simulation of an argon bubble in quiescent liquid GaInSn under horizontal magnetic field ($B = 0, 0.2$ T, 0.5 T) for different bubble sizes ($D = 3$ mm, 5 mm, 7 mm). Instable bubble motions were efficiently suppressed if a strong magnetic field ($B > 0.5$ T) is applied. The application of a horizontal magnetic field leads to a decrease of the rising velocity. This result does not qualitatively agree with Mori's measurement; the increase of the velocity for weak magnetic field was not observed.

Wang and Ni [6] experimentally studied a single bubble rise in quiescent liquid metal GaInSn using UDV technique. An external horizontal magnetic field up to 1.97 T was applied to bubble with diameters of 3.2-5.6 mm. Results were in good agreement with Mori's measurement; the rising velocity was discovered to be not monotonic respect to B. For the Stuart number $N < 1$ $\left(N = \dfrac{Ha^2}{Re}\right)$ magnetic field lead to an increase of the velocity, while for $N > 1$ the velocity is decreased by the magnetic field. More specifically, the maximum rising velocity for all bubbles is found for the condition at $N = 1$. Wang generalized Mendelson velocity formula valid for horizontal magnetic field, Eq. (1.9), and a correlation for the drag coefficient, Eq. (1.10), in the presence of a horizontal magnetic field ($N > 1$):

$$u_{TLM} = 0.932 \cdot \sqrt{\frac{2\gamma_l}{\rho_l D} + \frac{gD}{2}} \cdot N^{-0.254}$$

(1.9)

$$C_{dLM} = 1.07 \left(\frac{4\Delta\rho Dg}{3u^2_T \rho_l} \right) N^{0.508}$$

.

(1.10)

Summarizing previous works found in literature, it has been shown that an application of a horizontal/transverse magnetic field generally decreases the bubble rising velocity, straightens the rising trajectory and suppresses velocity oscillations.

1.3   Objectives of present study

In this study, Computational Fluid Dynamics (CFD) simulation was used to derive full understanding of a bubble rising in liquid metals with and without the presence of an external magnetic field. More precisely, the bubble rising velocity and the bubble deformation were investigated using the CFD code, PSI-BOIL.

For the rising bubble without magnetic field, a new drag coefficient is proposed for the liquid metal based on CFD simulation results, and it is compared to existing correlations in the literatures. A semi-analytical model for the bubble shape deformation is also derived by me for liquid metal, and it is compared with CFD results. Moreover, a new stability criterion is proposed for bubbles in liquid metal.

Furthermore, bubble rise in liquid metal under the presence of external magnetic field is analyzed. The conditions studied in this study is a single rising bubble in quiescent liquid metal under an external horizontal magnetic field; vertical magnetic field is not studied. First, a detailed explanation of all the physical phenomena which take place around the bubble is provided based on the CFD results. Then, rising bubble under the presence of an external magnetic field is simulated for different working fluids. A generalized rising velocity correlation is proposed by modifying Mendelson equation. An analytical correlation for the bubble aspect ratio is derived and compared with experiments in order to explain how shape deformation is influenced by the bubble size and by the applied magnetic field. The influence of the magnetic field on the bubble stability is studied by basic principles. Simulations show that external magnetic field enhances the stability of the bubble and straits the bubble trajectory, reducing the velocity and shape oscillation.

2 Governing equations and numerical methods

2.1 Governing Equations

The problem studied in this thesis is the single bubble rising in a quiescent liquid metal under the application of transverse magnetic field (parallel to the x-axis). The governing equations for the incompressible flow are defined as:

$$\nabla \cdot u = 0 \, , \tag{2.1}$$

$$\frac{\partial (\rho u)}{\partial t} + \nabla \cdot (\rho u \otimes u) = -\nabla p + \nabla \cdot \left(\mu \left(\nabla u + (\nabla u)^T \right) \right) + \rho g + \gamma \kappa n + J \times B \, , \tag{2.2}$$

where u [m/s] is the fluid velocity vector, p [Pa] the pressure, t [s] the time, ρ [kg/m³] the density, μ [Pa s] the dynamics viscosity, g [m/s²] the gravitational acceleration, J [A/m²] is electric current density vector, B [T] the magnetic field vector, γ [N/m] the surface tension coefficient between the gas and the liquid, κ [N/m] the local curvature of the interface, and n the normal vector of the interface.

The energy conservation equation was not solved since the thermal energy exchange can be considered negligible. Thus, the temperature field is assumed to be constant, and the material proprieties of the gas and the liquid are kept constants.

In order to compute material proprieties, a linear interpolation between liquid and gas has been made using the volume fraction H.

$$\mu = H \mu_1 + (1 - H) \mu_2 \tag{2.3}$$

$$\rho = H \rho_1 + (1 - H) \rho_2 \tag{2.4}$$

$$\sigma = H \sigma_1 + (1 - H) \sigma_2 \tag{2.5}$$

The governing equation for the transport of the volume fraction is written as Eq.(2.6), and it is solved with Volume Of Fluid (VOF) method:

$$\frac{\partial H}{\partial t} + \nabla \cdot (uH) = 0 \tag{2.6}$$

The continuity and momentum conservation equations are solved using the fractional step method. An adaptive time-step is used, the time step being defined as: $\Delta t = \min\{\Delta t_{CFL}, \Delta t_\gamma\}$, where

$$\Delta t_{CFL} = C_{CFL} \frac{\Delta}{|u_{max}|} \tag{2.7}$$

10

$$\Delta t_\gamma = 5 \cdot \sqrt{\frac{0.5 \cdot \rho_{GAS} \cdot \Delta^3}{2\pi\gamma}} \ .$$

(2.8)

C_{CFL} is the Courant-Friedrichs-Lewy (CFL) number and it is set to 0.25 in this study. *u, v* and *w* are the velocity component in the x-, y- and z-directions, respectively, and *Δ* is the grid spacing.

2.2   Electric potential method

We know by theory that an external magnetic field B_{ext} applied to a liquid metal, can produced an induced magnetic field, B_{ind}, which can alter the total value; $B_{tot} = B_{ext} + B_{ind}$. In general, in order to find a connection between magnetic and velocity field the magnetic induction method is used.

The Maxwell equations and the generalized Ohm's law are defined in Eqs. (2.9) and (2.10), respectively.

$$\frac{\partial B}{\partial t} = -\nabla \times E$$

(2.9)

$$J = \sigma\left(E + u \times B\right)$$

(2.10)

Using these two equations, the next equation which directly connects the velocity and the magnetic field can be obtained:

$$\frac{\partial B}{\partial t} = -\nabla \times \left(\frac{J}{\sigma} - u \times B\right) \ .$$

(2.11)

By dimensionless analysis of the Faraday law Eq. (2.13), it can deduced Eq. (2.14), where *U* is the characteristic velocity of the system, which is the bubble rising velocity in the current problem.

$$\nabla \times E = -\frac{\partial B}{\partial t}$$

(2.12)

$$\frac{E}{L} \cdot \nabla^* \times E^* = -\frac{B}{T} \cdot \frac{\partial B^*}{\partial t^*}$$

(2.13)

$$\frac{E}{L} \sim \frac{B}{T} \rightarrow \frac{E}{B} \sim \frac{L}{T} = U \ .$$

(2.14)

Next, the dimensionless Ampere-Maxwell law is considered, Eq. (2.16).

$$\nabla \times B = \mu_B J + \frac{1}{c^2} \cdot \frac{\partial E}{\partial t} \tag{2.15}$$

$$\frac{B}{L} \cdot \nabla^* \times B^* = J \cdot \mu J^* + \frac{1}{c^2} \cdot \frac{E}{T} \frac{\partial E^*}{\partial t^*} \tag{2.16}$$

The current density in the Ampere-Maxwell law Eq. (2.15) is the sum of a magnetic field and electric field dependent components. The relative importance of the two terms can be expressed as:

$$\frac{E/T}{D/L} \sim \frac{\mu \varepsilon E L}{BT} \sim \frac{U^2}{c^2} \tag{2.17}$$

Since the characteristic velocity is much small than the speed of light $\left(\frac{U^2}{c^2} \ll 1 \right)$, the term $\frac{\partial E}{\partial t}$ is considered to be a negligible component, and the Ampere-Maxwell equation can be simplified as:

$$\nabla \times B = \mu J \tag{2.18}$$

By substituting Eq. (2.18) in Eq. (2.11) we obtain Eq. (2.19).

$$\frac{\partial B}{\partial t} = \nabla \times (u \times B) - \frac{1}{\sigma \mu} \nabla \times (\nabla \times B) \tag{2.19}$$

Using the vector identity $\nabla \times (\nabla \times B) = \nabla(\nabla \cdot B) - \nabla^2 B$ and the Gauss theorem $\nabla \cdot B = 0$, the final magnetic induction equation Eq. (2.20) is found.

$$\frac{\partial B}{\partial t} = \nabla \times (u \times B) + \frac{1}{\sigma \varepsilon} \nabla^2 B \tag{2.20}$$

Finally, the magnetic induction equation is resized in order to find the relative importance of all terms, Eq. (2.21).

$$\frac{B}{T} \cdot \frac{\partial B^*}{\partial t^*} = \frac{uB}{L} \cdot \nabla^* \times (u^* \times B^*) + \frac{1}{\sigma \varepsilon} \cdot \frac{B}{L^2} \cdot \nabla^{*2} B^* \tag{2.21}$$

$$\frac{\partial B^*}{\partial t^*} = \nabla^* \times (u^* \times B^*) + \frac{1}{\text{Re}_m} \cdot \nabla^{*2} B^* \tag{2.22}$$

The magnetic Reynolds number Re_m is defined as $\frac{induction}{diffusion} \simeq \mu \cdot \sigma \cdot D \cdot u$. In case study Re_m is very small $O(10^{-3})$ which means advection is relatively unimportant, and so the magnetic field will tend to

relax towards a purely diffusive state, determined by the boundary conditions rather than the flow. Induced magnetic field is therefore irrelevant and $B_{tot} \approx B_{ext}$. The total magnetic field can be approximated with the external one without loss of generalities.

Since the magnetic field is a constant value, the only unknown is the electric current density J. In order to obtain the electric current density, an electric potential method is introduced. Since we are dealing with a conductive material, we consider the system as a succession of quasi-static equilibrium. At each time-step the local charge density has to remain zero in each point of the system. For Gauss theorem, Eq. (2.23) is found. Using Eq. (2.23) a constitutive equation between the electrical potential and the velocity field can be found as described in Eq. (2.24). Once the electrical potential field is computed, the electric current density is computed by Eq. (2.25).

$$\nabla \cdot J = 0 \tag{2.23}$$

$$\nabla^2 \phi = \nabla \cdot (u \times B) \tag{2.24}$$

$$J = \sigma(-\nabla \phi + u \times B) \tag{2.25}$$

2.3 Discretisation and solution algorithm

The in-house CFD code, PSI-BOIL, was used in this study. The Navier–Stokes equations are discretized using a semi-implicit projection method in time [12]. The diffusion term is discretized according to the Crank–Nicolson scheme in time, and the advection terms using the Adams–Bashforth scheme. For the spatial discretization, the Cartesian finite-volume method is used in the staggered variable arrangement [13]. The second-order-accurate, central-difference scheme is used for the diffusion term, and a second-order scheme with flux limiter [14] for the advection term.

The algorithm for solving the equations is:

1. Electric Potential ϕ is computed from the velocity vector field u at the N time-step.

$$\nabla^2 \phi^N = \nabla \cdot (u^N \times B) \tag{2.26}$$

2. Electric current density is computed explicitly from the Ohm's equation.

$$J^N = \sigma\left(-\nabla\phi^N + u^N \times B\right)$$

(2.27)

3. Lorentz, gravitational and surface tension forces are computed.

$$\mathcal{F}^N = J^N \times B + \rho g + \gamma\kappa n$$

(2.28)

4. Velocity field and pressure field at the new time-step *N*+1 is computed using a fractional step method.

5. Update volume fraction by solving Eq. (2.6) using VOF method.

3 Verification and validation

3.1 Validation of single phase flow under magnetic field

Single phase magneto fluid dynamics (MHD) simulation has been performed with PSI-BOIL in order to validate the code. The system studied is a square duct ($2L \times 2L \times 0.25L$) at which is applied a constant pressure gradient delta p. Furthermore, an external magnetic field B is applied perpendicular to the flow direction (y direction). The computational system studied consists in a 0.25 L thick layer at which periodic boundary conditions are applied for all the governing variables. No-slip boundary condition are set on the walls. The system is studied under steady state conditions. This is one of the few MHD problems which has an analytical solution. Therefore, PSI-BOIL MHD results are compare to the exact solution without any need of making experimental tests.
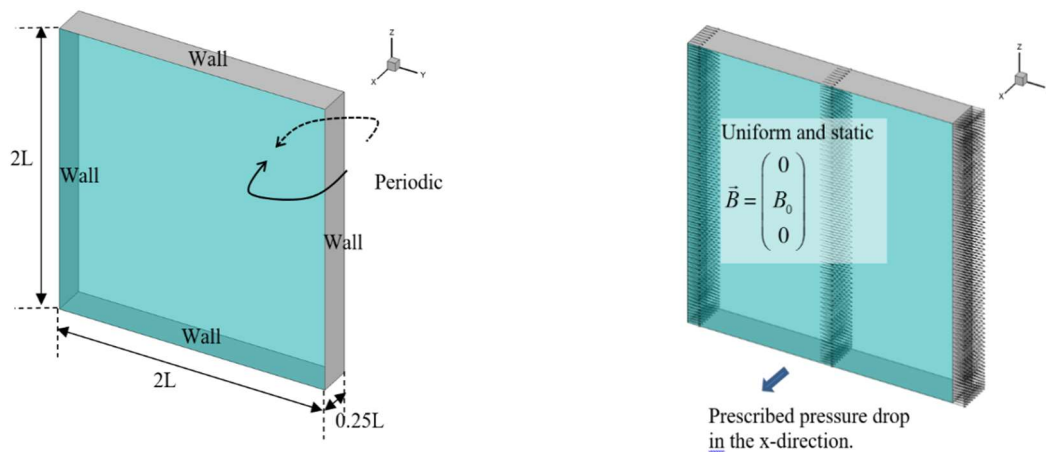

Figure 2"Computational domain and boundary condition (left). The applied magnetic field and the pressure drop direction (right).''

Axial velocity, electric potential and current density fields are studied inside the duct for different external magnetic fields. The whole problem is independent of the liquid density since the liquid is in steady state condition. For simplicity all material proprieties are set to 1. Velocity profile is strongly influence by external magnetic field presence. The profile becomes more flatten in the center and decreases to zero only in the surrounding of the walls. Shear stresses between liquid and walls are strongly increased with the consequence of increasing the pressure losses. It can be noted that the velocity flattening is not axisymmetric but it is more prominent in the magnetic field direction (y).
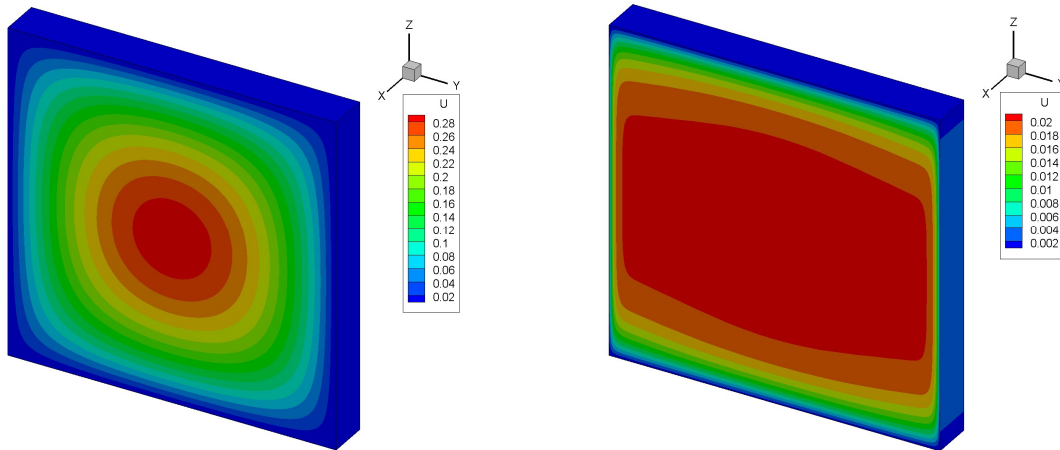
Figure 3 "Distribution of axial velocity of B0 (left) and B=50 t (right) Unit : m/s."

Let define k as the pressure drop $\left(\dfrac{\partial p}{\partial x}\right)$, v_0 as the average velocity $\left(\dfrac{V}{(2L)^2}\right)$ and $2a$ as the channel thickness. It can be see that PSI-BOIL results are in perfect agreement with the general analytical solution for all the Hartmann number $\left(Ha = BD \cdot \sqrt{\dfrac{\sigma}{\mu}}\right)$. Therefore, the single phase MHD validation can be considered successful. PSI-BOIL is able to precisely simulate single phase MHD problem.
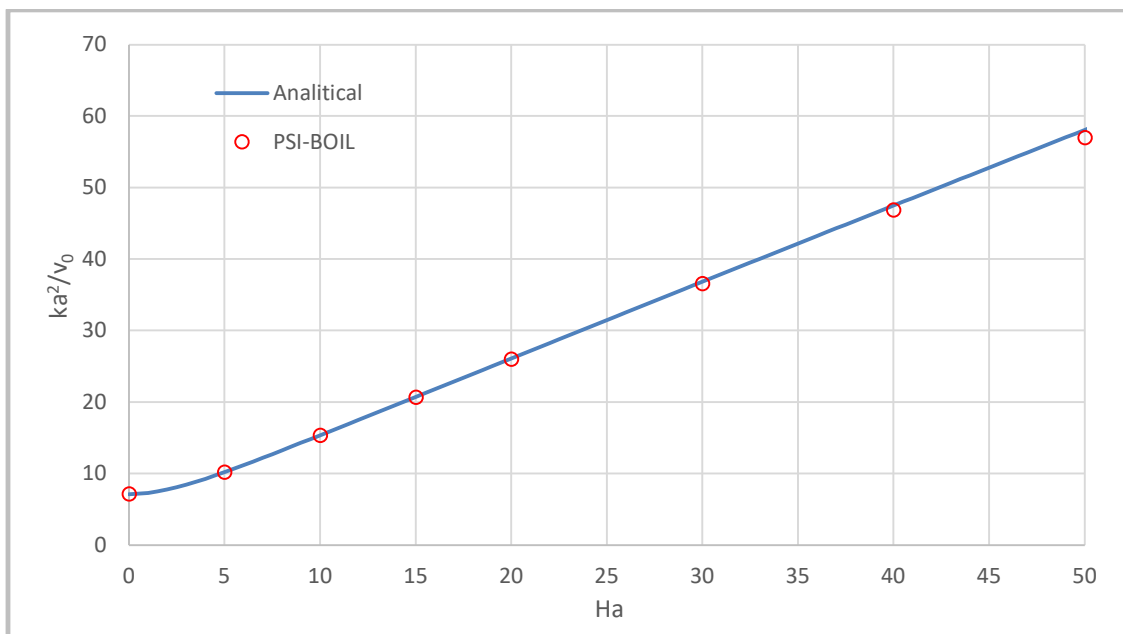
"Figure 4 "ka2/v0 for different Hartmann numbers."

3.2 Verification and validation of two-phase flow: code-code comparison

A code-code comparison has been performed for multiphase flow with magnetic field by comparing the results of PSI-Boil and Zhang et al. [15]. The simulation case considered here is a single argon bubble (D=3 mm) rising in quiescent liquid iron.

Table 1 "Argon & Iron material proprieties."

	μ [Pa s]	ρ [kg/m^3]	σ [S/m]	γ [N/m]
Argon	$7.42{\times}10^{-5}$	0.56	$1{\times}10^{-15}$	1.20
Iron	$6.30{\times}10^{-3}$	7000	$7.14{\times}10^{5}$	

A 3D rectangular computational domain with the dimensions of $6D \times 6D \times 24D$ is used with the uniform cube mesh of the width dx. A spherical argon bubble is placed at $2D$ distance from the bottom. The liquid is quiescent at the beginning. The boundary surfaces surrounding the computational domain are set to the electrically insulated, non-slip wall. The height of $24D$ is sufficient for all the bubble to reach terminal velocity without having deceleration due to the upper wall influence.

In order to study the influence of the grid size on the results, four cases of computational mesh with different grid spacing have been used for the simulation (D/dx = 10.67, 16.0, 21.34 and 32.0), and the terminal rising velocity is compared. Studies with and without external magnetic field, have been conducted.

As it can be seen in Figure 5, the difference of the Reynolds number based on the terminal velocity between PSI-Boil (finer grid) and Zhang et al. [15] is less than 3% , which is considered to be good agreement. On the other hand, For the case with the magnetic field, the discrepancy between PSI-BOIL (finer grid) and Zhang et al. [15] is large (29%); $Re_{psi\text{-}boil}$ = 1352 and Re_{Zhang} = 1048. The reason for the discrepancy is unclear, but it might be caused by the different discretization scheme used in the codes.

The grid sensitivity study shows that the difference of the rising velocity between D/dx = 16 and 21.34 is 1.9% for the case B = 0 and 2.3% for the case B = 0.5 T, which is considered to be small enough for this study. Therefore the grid spacing of D/dx = 16 is used as a default grid all the simulations reported hereafter.
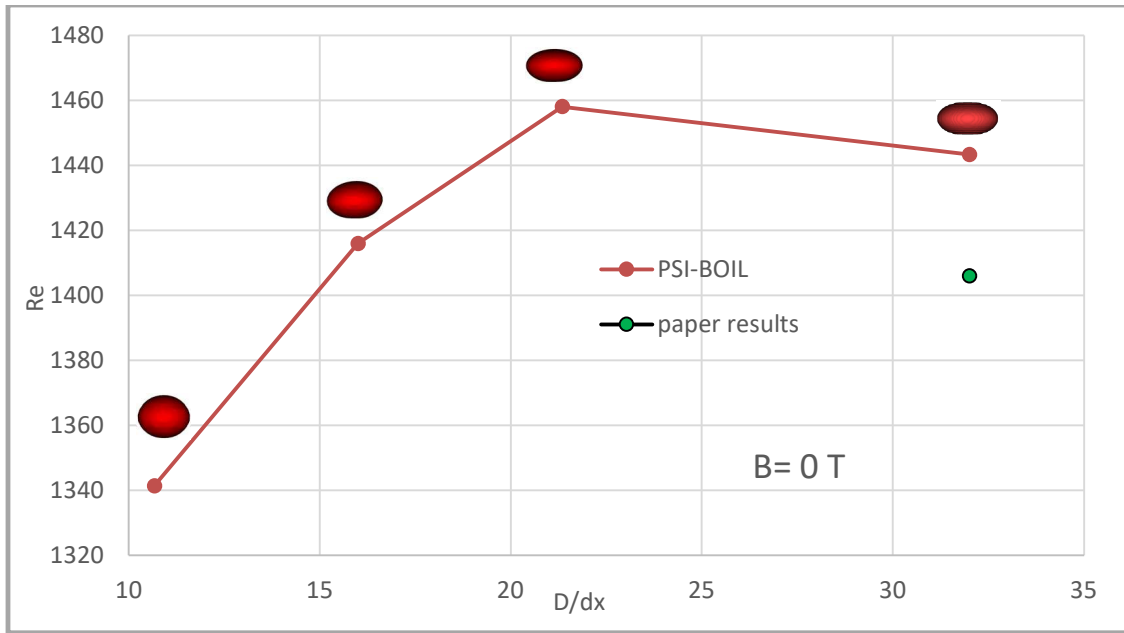
Figure 5 "Comparison between PSI-Boil and Zhang et al. [15] for the case without magnetic field."
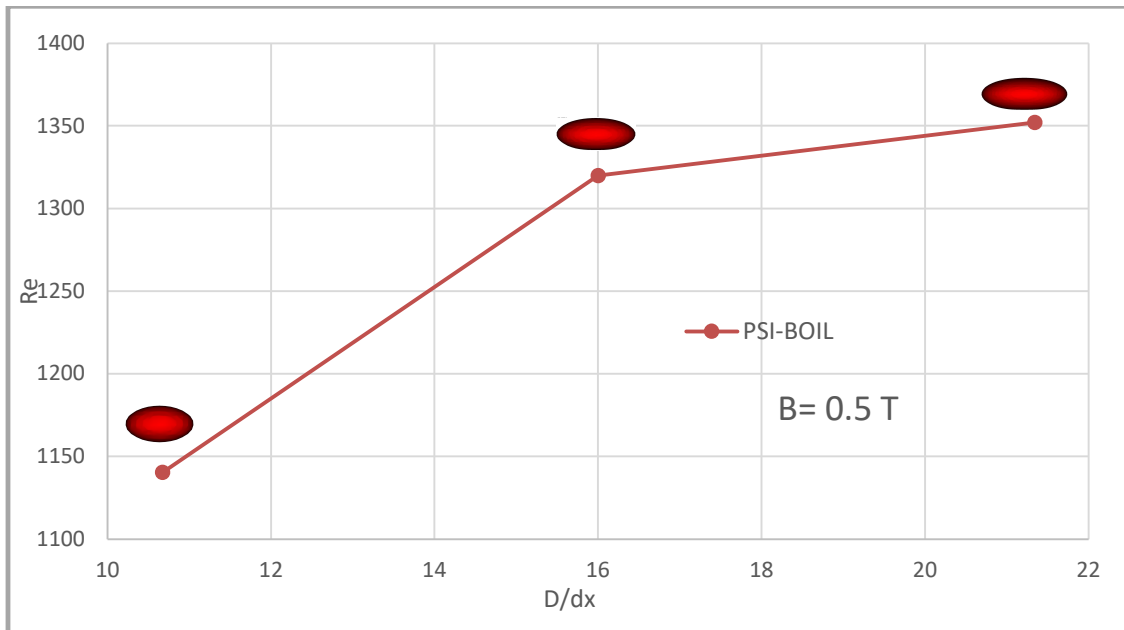

Figure 6 "Comparison between PSI-Boil and Zhang et al. [15] for the case with magnetic field (B = 0.5 T)."

4 Conditions of simulations

A 3D rectangular computational domain with the dimensions of 6D x 6D x 24D (both lateral directions and the height) is used, which is discretized with a uniform cube mesh (dx=D/16). The liquid is quiescent at the beginning. The height of 24D is sufficient enough for all the bubble to reach terminal velocity. The width of 6*D* makes the flow independent from the influence of surrounding walls.

The simulations with different bubble sizes (0.1 < *Eo* < 2) and external magnetic field (*B* =0, 0.5 T, 1.0 T, 1.5 T) have been conducted. Three cases of systems with different combination of material have been used: Argon-GaInSn, Nitrogen-Mercury, Argon-iron. The material properties are listed in Table 2.

Table 2 "Material proprieties for three systems with different combination of gas and liquid phases."

	μ [Pa s]	ρ [kg/m^3]	σ [S/m]	γ [N/m]
Argon	1.176e-5	1.654	1.00e-15	0.5330
GaInSn	2.20e-3	6.36e3	3.27e6	
Nitrogen	1.77e-5	1.17	1.00e-15	0.4535
Mercury	1.50e-3	1.35e4	1.02e6	
Argon	1.176e-5	1.654	1.00e-15	1.200
Iron	6.30e-3	7.00e3	7.14e5	

4.1   Boundary conditions

The non-slip Boundary Condition (BC) is set to all the walls. For the electric potential ϕ, a Neumann BC is set to the walls. The static magnetic field (*B*, 0, 0) is set to the whole computational domain. For the electric current field, the component of $J(J_\perp)$ perpendicular to the wall is set to zero because the tank is assumed to be made of an insulant. For the parallel component of $J(J_\parallel)$ instead, a Neumann BC is applied.

4.2   Initial conditions

At the beginning of the simulation, the velocity field, the electric current density field, the electric potential field are zero. The pressure field follows Stevino's law and increases linearly with the depth. A spherical bubble placed at the center in the x- and y-directions and 2D distance from the bottom as shown in Figure 7.
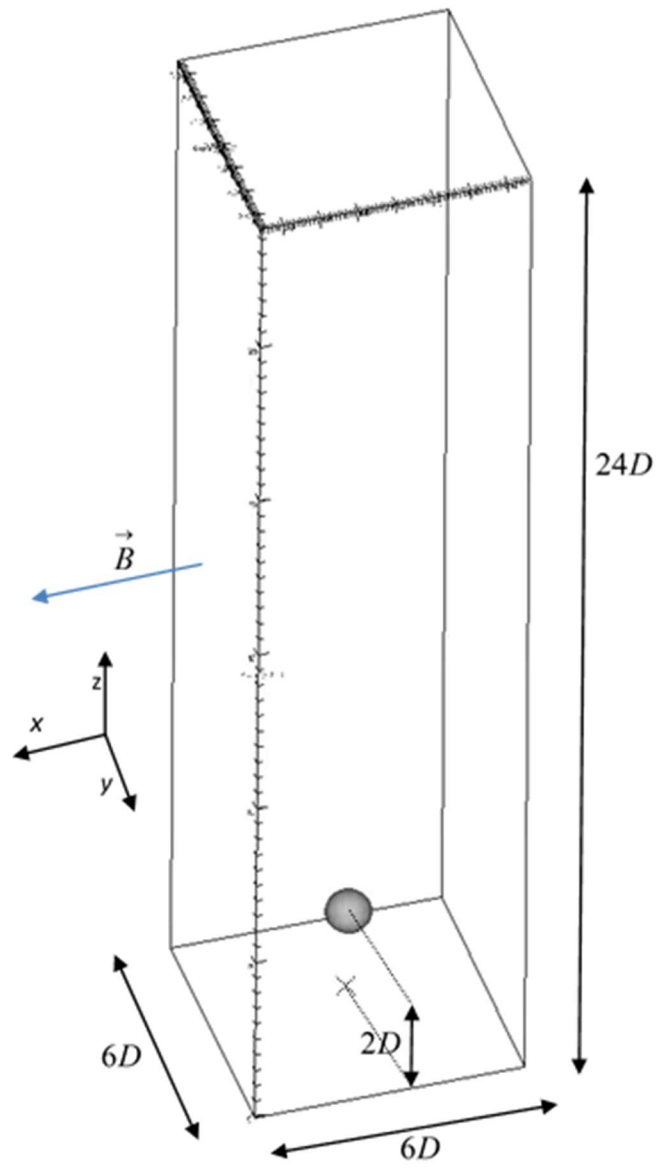
Figure 7 "Computational domain and the initial bubble."

5 Bubble dynamics in liquid metal without magnetic field

5.1 Analytical Description

5.1.1 Governing parameters

A single bubble rising in liquid metal is characterized by high Reynolds number Eq. (5.1) and considerably low Morton numbers Eq. (5.2). The Reynolds number which is on the order of thousand due to the high liquid metal density compared to water, suggests that inertia forces are predominant compared to viscous forces $\left(\mathrm{Re} \gg 1\right)$. The Morton number is considerably low $\left(\simeq 10^{-13}\right)$ which means that Archimedes Eq. (5.4) and surface tension forces are more dominant compared to viscous forces. The two driving factors which characterize the bubble rising in liquid metal are the inertia and superficial forces while the viscous term, still present, does not play any substantial role.

$$\mathrm{Re} = \frac{F_{inertia}}{F_{viscous}} \simeq 10^4$$

(5.1)

$$Mo = \frac{F_{viscous}}{F_{surf.tens} \cdot F_{archimede}} \simeq 10^{-13}$$

(5.2)

The system will be characterized by only two dimensionless parameters Eq. (5.3) in which the viscosity in absent since it has no more driving power. In this analysis the Eotvos number and the Weber number $\left(We = \frac{\rho \cdot v^2 \cdot D}{\gamma}\right)$ have been used.

$$F\left(\Pi_1, \Pi_2, \Pi_3\right) = 0 \rightarrow F\left(We, Eo\right) = 0 \rightarrow We = F(Eo)$$

(5.3)

Under this, approximation a 2 variable function fully characterizes the problem. Furthermore, since the Eotvos is not velocity dependent the bubble rising velocity can be explicitly express as a function of material and geometry proprieties.

5.1.2 Negligible shear stress field

In Newtonian fluid the stress tension is proportional to the velocity gradient $\tau = \mu \cdot \nabla u$. In solid sphere, since inner bubble recirculation does not happen, the liquid velocity on sphere surface is zero and the $\tau \cong \mu \cdot \dfrac{u_\infty}{L}$ with L equal to the characteristic decreasing length.

Bubbles rising in liquid metal regime experiment a reduced viscous effect. Surface shear stress field on the bubble surface is significantly reduced by two phenomena:

- First, inner gas recirculation takes place and the bubble surface velocity in not zero anymore. Since there is a huge difference in gas-liquid density, the outermost layer of gas is carried by the external liquid which has an higher inertia. Therefore, the velocity gradient and the shear stress are significantly reduced $\tau \cong \mu \cdot \dfrac{u_\infty - u_{surf}}{L}$. This effect is relevant for enough big bubble for which there is enough space inside in order to create convective gas movement.

- Secondly, if the liquid is pure enough (which is the case of our CFD simulation), it has the possibility to slip along the surface of the bubble (inviscid approximation), furthering decreases the local velocity gradient. Both this two contributions significantly reduces the tension stress field across the bubble interface.
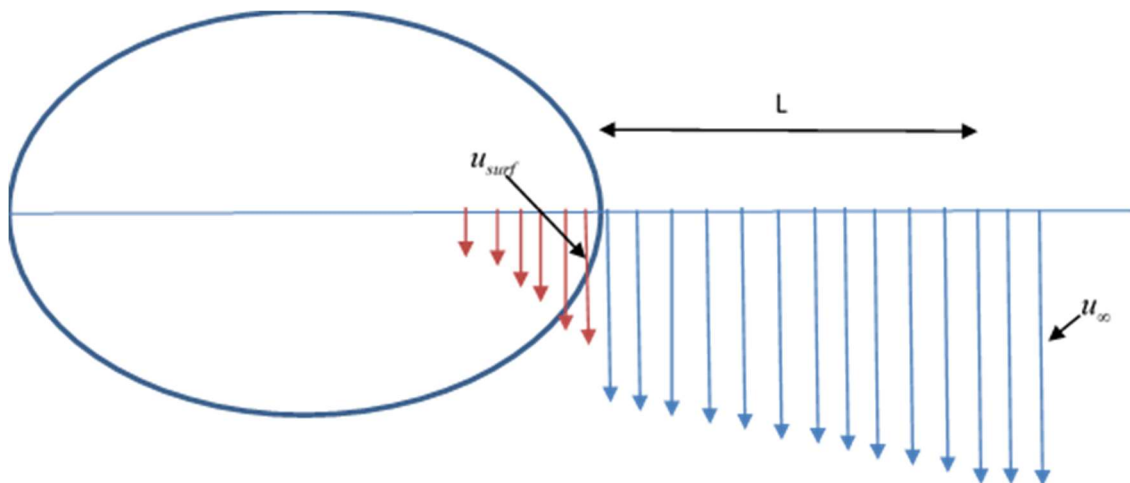

Figure 8 "Lagrangian velocity field close to the interface of a spherical-shape bubble."

5.1.3 Bubble force balance

At the equilibrium the buoyancy force which are velocity independent Eq. (5.4), are balanced by the drag force Eq. (5.5) which generally increases with the velocity. Buoyancy force is the sum of the gravitational force and the surface integral of the static pressure $\rho g h$ acting on the bubble. The drag force is computed by the integration of the pressure $\left(p_{tot} - p_{static} \right)$ and tension field.

In this analysis, the system considered is the whole bubble which is the sum of the interface and the inner gas. Since the surface tension is a mutual force which acts between the surface and the inner gas, it does not have to be considered since it is an internal force of the system.

$$F_{buoyancy} = -mg + \oiint p_{static} \cdot \vec{dA} = -\rho_g Vg + \rho_l Vg = \Delta\rho \cdot V \cdot g = \Delta\rho \cdot \frac{\pi D^3}{6} \cdot g \qquad (5.4)$$
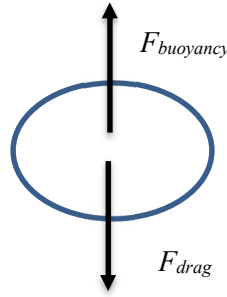
$$F_{drag} = \oiint \left(p_{tot} - p_{static} \right) \cdot \vec{dA} + \oiint \tau_{//} \cdot \vec{dA} \qquad (5.5)$$

In order to compute the drag, velocity and pressure distribution all over the bubble surface has to be known. Generally, the pressure and the tension terms are equally important and needed to be both computed. Pressure field across the bubble is computed resolving the Navier-Stokes equations Eq. (5.6) along a streamline from a distant point to the surface Eq. (5.7). The pressure on the bubble surface is the sum of a gravitational, kinematic and viscous term. The gravitation term is not processed since it is already considered in the buoyancy force. The $p_{tot} - p_{static}$ field on bubble interface is the sum of a kinematic and viscous pressure, Eq. (5.8).

$$\rho\left[\frac{\partial u}{\partial t} + u \cdot \nabla u\right] = -\nabla p + \mu\nabla^2 u + \rho g \cdot dz \qquad (5.6)$$

$$\rho\int_{\infty}^{s}(u \cdot \nabla)u \cdot dr = -\int_{\infty}^{s}\nabla p \cdot dr + \mu\int_{\infty}^{s}\nabla^2 u \cdot dr + \int_{\infty}^{s}\rho g \cdot dr \qquad (5.7)$$

$$p_{tot} - p_{static} = \frac{\rho}{2} \cdot \left(u^2(s) - u_\infty^2\right) + \mu \int_\infty^s \nabla^2 u \cdot dr \qquad (5.8)$$

In the upper part of the bubble, the kinematic pressure is much bigger than the viscous pressure $\left(\frac{1}{2}\rho u_\infty^2 >> \mu \int_\infty^s \nabla^2 u \cdot dr\right)$ because of the high density of liquid metals and because of the little stress tensor field $\tau = \nabla u$.

$\vec{r}$ represents the streamline of the flow and $\vec{s}$ the position on the bubble surface.

$$\Delta p_{viscous} = \mu \int_\infty^s \nabla \cdot \overline{\overline{\tau}} \cdot dr = \mu \int_\infty^s \frac{\partial}{\partial s} \tau_s \cdot dr = \mu \int_\infty^s \tau_s(r) \cdot dr$$

- $\tau(\infty)$ is zero and it increases approaching point A in which τ reaches its maximum value.

- Tension stress field $\tau(A)$ is negligible since the velocity changes almost linearly on the side of the bubble due to the efficient inner bubble recirculation [Chap.4]

- Therefore, also $\int_s^\infty \tau_s(r) \cdot dr$ is negligible and the viscous overpressure is zero.

- Viscous pressure is negligible for each point in the upper part of the bubble
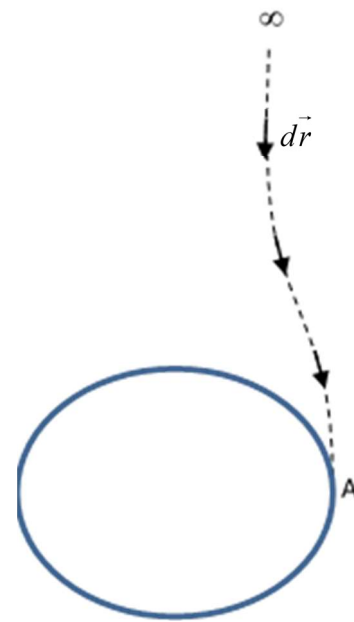
Before the bubble detachment point, the fluid can be considered inviscid, there are not any momentum dissipations and all the liquid momentum energy is transferred into pressure. The Bernoulli equation Eq. (5.9) in its simplicity definitely describes the relation between the pressure and the velocity field. When the liquid is approaching the bubble surface, the velocity is decreased and the kinematic energy is transferred into pressure energy. The stagnation point of the bubble (top point) has the highest pressure while approaching the sides of the bubble the pressure monotonously decreases. Therefore, the inviscid model is used to model the pressure on the bubble surface. Boundary layer does not exist and on the bubble surface only the tangential component of the velocity $u_{//}$ is present.

$$\Delta\left(p_{tot}-p_{static}\right)+\frac{1}{2}\rho\Delta u^2=0 \tag{5.9}$$

How the pressure change from the stagnation point to the bubble sides depend on bubble shape (X) which is in turn dependent on the acting pressure on the surface. Nevertheless, it can be established that the surface pressure field is proportional to the stagnation point pressure which is, according to Bernoulli, equal to $\frac{1}{2}\rho_l u_\infty^2$. Therefore, the kinematic overpressure Eq. (5.10) depends on the bubble velocity u_∞ and on the local tangential velocity to the surface $u(s)$.

$$p_{kinematic}\left(s\right)=\frac{1}{2}\rho\left(u_\infty^2-u^2(s)\right) \tag{5.10}$$

After the detachment point, the inviscid approximation is not anymore reasonable (Figure 9). On the bottom of the bubble the fluid is not anymore irrotational and dissipation phenomena take place. The pressure on the bottom of the bubble is significantly reduced because all the liquid momentum is dissipated by the viscosity friction and not converted into pressure energy. From the Lagrangian point of view, the fluid particles which is approaching the bubble surface decelerates and decreases its kinematic energy. In an ideal case pressure is increases in order to conserve kinetic energy but due to viscous force, most of the energy is dissipated and the liquid pressure is drastically reduced compared the non-viscous case. How much energy is transferred into pressure and how much is lost depends on the velocity field. In this analysis, a total dissipation model is used for simplicity. Therefore, all kinematic energy of the liquid is dissipated and the pressure field after the detachment point can be approximated to zero Eq. (5.11) and has not impact for the drag force (Figure 10).

$$p_{tot}\left(s\right)-p_{static}\left(s\right)=\frac{1}{2}\rho\left(u_\infty^2-u^2(s)\right)+\mu\int_\infty^s\nabla^2 u\cdot ds\simeq0 \tag{5.11}$$
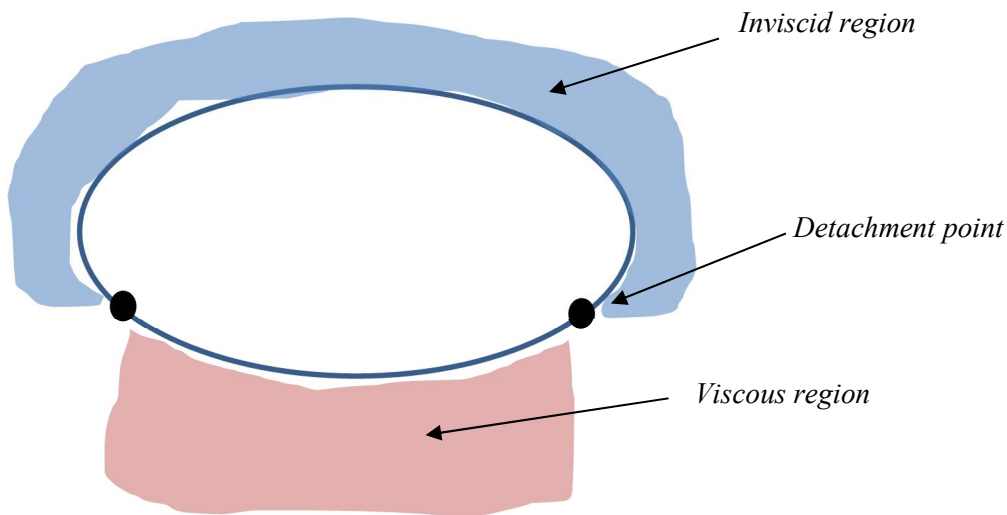
Figure 9 "Top and Bottom of the bubble modeled respectively with inviscid and viscous model."

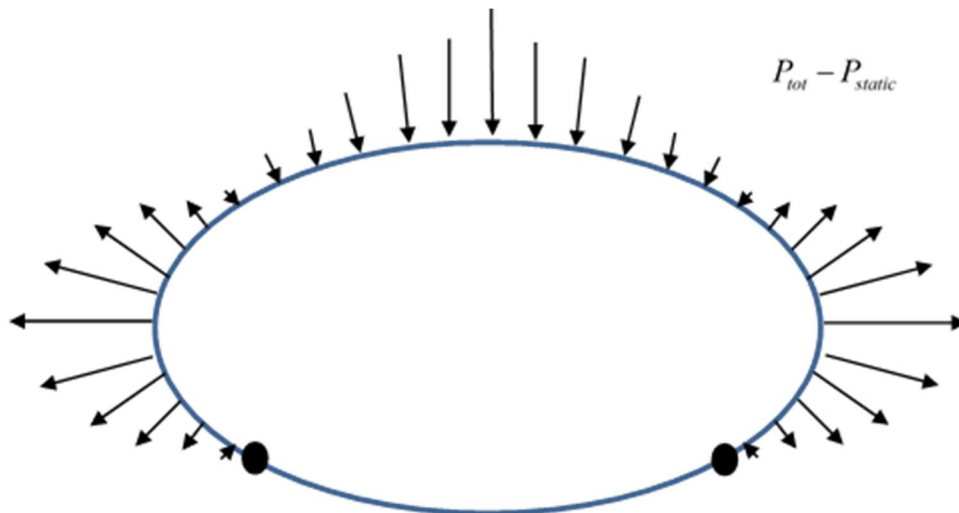*Figure 10 Pressure field (P.tot-P.static) on bubble surface."*

For computing the drag force, the shear stress component is neglected since much lower compared to the pressure component. Moreover pressure field is integrated only in the "inviscid region" since pressure on the bottom is assumed to be zero due to dissipation, Eq. (5.12). The $p_{tot} - p_{static}$ in the inviscid region is the kinematic pressure.

Clearly, the viscous pressure is physically the main cause of the drag force but, due to the fully dissipation model used in the bottom of the bubble, liquid viscosity coefficient does not influence the bubble dynamics and the drag force depends only on the kinematic pressure in the upstream of the detachment point.

The detachment point of the liquid from the liquid surface depends on the bubble shape and on the specific kinematic energy of the liquid$\left(\rho u^2 \right)$. Since the bubble is assumed to be ellipsoidal, it can be

assumed with any loss of generality that the detachment point depends on the bubble aspect ratio and on the bubble Weber number.

$$F_{DRAG} = \oiint (p_{tot} - p_{static}) \cdot \vec{dA} + \oiint \tau_{//} \cdot \vec{dA} \simeq \oiint p_{kinematic} \cdot \vec{dA} = \oiint \frac{1}{2} \rho (u_\infty^2 - u^2(s)) \cdot \vec{dA} \quad (5.12)$$

The final balance equation is Eq. (5.13):

$$\Delta\rho \cdot \frac{\pi D^3}{6} \cdot g = \oiint \frac{\rho}{2} \cdot (u_\infty^2 - u^2(s)) \cdot \vec{dA} \tag{5.13}$$

The liquid velocity on the bubble surface has only the component tangential $u_{//}$ to the surface while the normal component u_n is zero in order to conserve the flowrate $(\nabla \cdot u = 0)$ We assume the local velocity on the surface of the bubble is proportional to the rising bubble velocity. $u*(\vec{s})$ is a unknown function which represents the dependency of the velocity on the local position Eq. (5.14).

$$u(s) = u*(s) \cdot u_\infty \tag{5.14}$$

$$\Delta\rho \cdot \frac{\pi D^3}{6} \cdot g = \oiint \frac{\rho \cdot u_\infty^2}{2} \cdot (1 - u*^2(s)) \cdot \vec{dA} \tag{5.15}$$

$$\Delta\rho \cdot \frac{\pi D^3}{6} \cdot g = \frac{\rho \cdot u_\infty^2}{2} \cdot \overline{1 - u*^2(s)} \cdot \pi D^2 \tag{5.16}$$

$$Eo = 3 \cdot We \cdot \overline{1 - u*^2(s)} \tag{5.17}$$

$$\overline{1 - u*^2(s)} = g(X(We)) = g(We) \tag{5.18}$$

$$Eo = 3 \cdot We \cdot g(We) \tag{5.19}$$

$$F(We, Eo) = 0 \tag{5.20}$$

As it can be seen in Eq.(5.19), the whole system is characterized by only two dimensionless numbers which are connected.

The $\overline{1 - u*^2(s)}$ is the surface average of the function $1 - u*^2(s)$ in the inviscid region before the detachment point. It can be exactly known only resolving the flow and pressure field around the bubble. Nevertheless, assuming the bubble is ellipsoidal shaped, it can be said that $\overline{1 - u*^2(s)}$ is a function of

the aspect ratio of the ellipsoid $\left(X = \dfrac{a}{c} \right)$. It is demonstrated in the next chapter that the aspect ratio is

a function of the Weber parameter only. This means that Eotvos and Weber numbers are univocally

connected in "rising bubble problem in liquid metals".

5.2 Terminal rising velocity

5.2.1 Comparison against Tomiyama's correlation

The computed Reynolds number based on the terminal rising velocity is compared with Tomiyama's correlation Eq. (5.21) in Figure 11 as the function of Eotvos number. The range simulated here corresponds to the Mendelson's formula in the Tomiyama's correlation, in which the velocity is controlled only by the Eotvos number. It can be observed that on first approximation, the Tomiyama's correlation and therefore the Mendelson equation predicts well the bubble behavior giving the right order of magnitude for the terminal Reynolds number.

$$C_D = \max\left\{\min\left[\frac{16}{\mathrm{Re}}\left(1+0.15\,\mathrm{Re}^{0.687}\right),\frac{48}{\mathrm{Re}}\right],\frac{8}{3}\cdot\frac{Eo}{Eo+4}\right\} \tag{5.21}$$
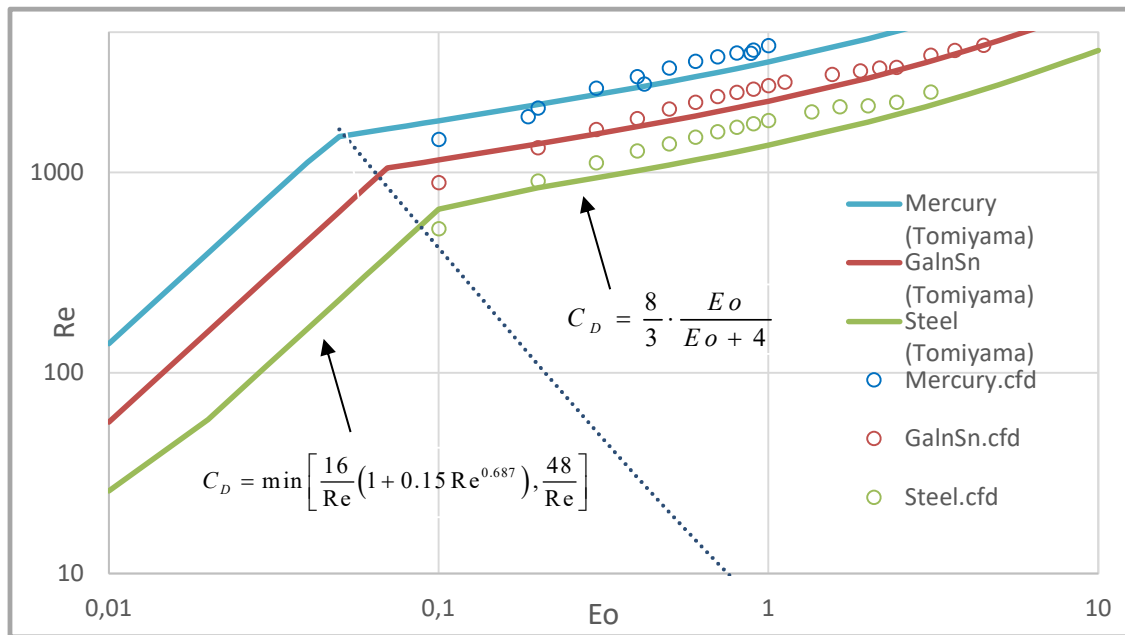

Figure 11 "Comparison between Tomiyama's correlation and PSI-BOIL simulation results."

In Tomiyama's correlation (Figure 11), there is a rapid change of the velocity profile when we pass from the Eotvos dependent region $\left(C_D = \frac{8}{3}\cdot\frac{Eo}{Eo+4}\right)$ to the Reynolds number dependent region $\left(C_D = \frac{48}{\mathrm{Re}}\right)$. As we take smaller bubbles, the Reynolds number acquires more importance while the Eotvos loses importance in determining the drag coefficient. In simulations, the change from *Eo* to *Re* regions is gradually and the velocity slope is changed smoothly from negative to positive.

Unfortunately, due to parasitic current, it was impossible to simulate bubbles with *Eo* < 0.05. Therefore, the C_D = 48/Re dependency region cannot be demonstrated by simulations.

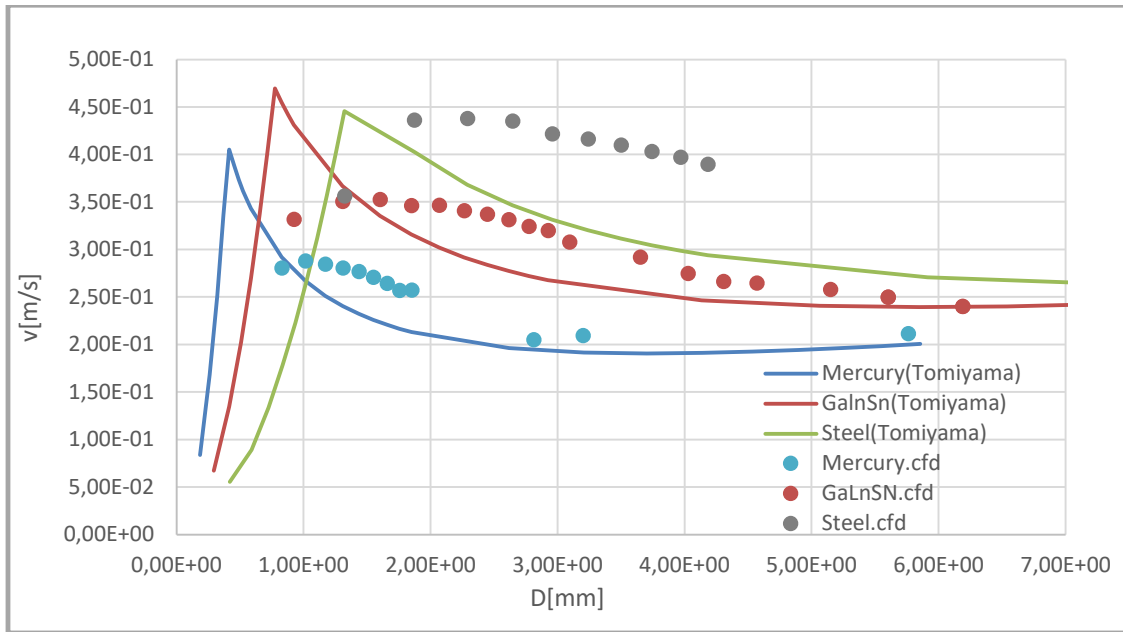Figure 12 shows the comparison of the terminal rising velocity as the function of the bubble diameter.

Figure 12 "Comparison of terminal velocity as the function of bubble diameter between Tomiyama's correlation and PSI-BOIL. "
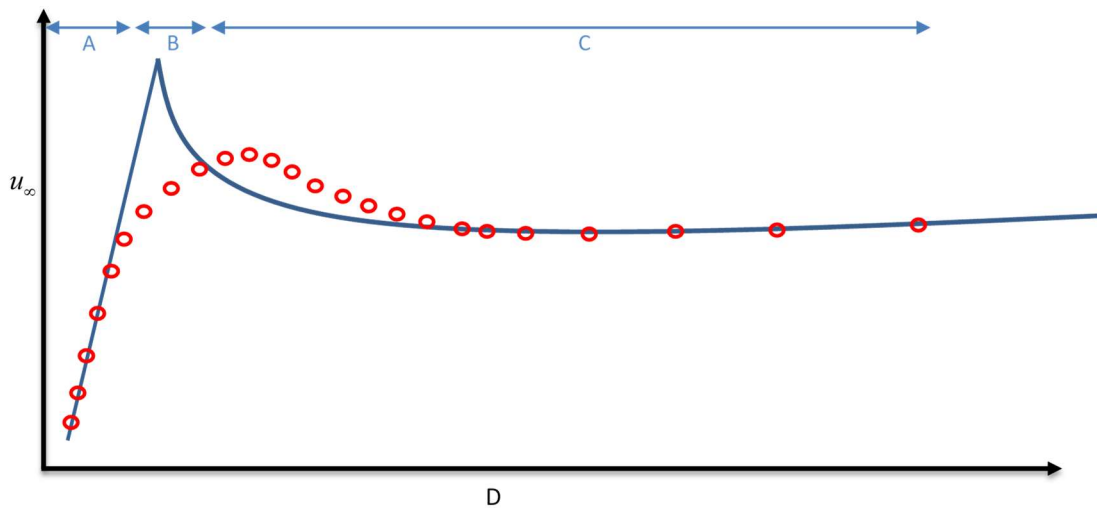

Figure 13 "A sketch of qualitative comparison between Tomiyama's correlation and PSI-BOIL result."

In the A-region depicted in Figure 13, a bubble is considered to be almost spherical. The aspect ratio is unity and the bubble behaves like a rigid sphere especially for the smaller diameter. Circulation of air flow inside the bubble is not induced because of the little size of the bubble $V \sim D^3$. Therefore, the shear stress field across the bubble is not negligible. The inertia and the viscous forces are the dominant
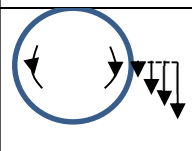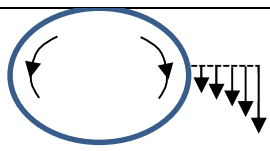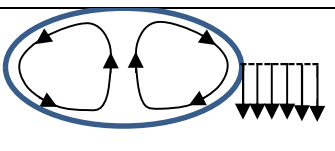
parameters with respect to the rising velocity and the drag coefficient depends on only Reynolds number; $C_D = \dfrac{48}{Re}$.

In the C-region, as discussed before, the flow may be assumed to be inviscid, and the influence of the viscosity on the rising velocity is considered to be small. The surface tension and inertia forces are the dominant parameters which characterize the bubble dynamics and the drag coefficient depends only on the Eotvos number; $C_D = F(Eo)$.

In B region, logically, the system cannot be characterized by only one number because viscous and surface tension forces are both important. These bubbles will experience both a shape deformation and a viscous stress field on the surface. The drag coefficient depends on two independent dimensionless number $C_D = F(Eo, Mo)$. The use of Tomiyama's correlation in this region leads to an overestimation of the rising velocity.

Our focus is in the inviscid region (region C).

Table 3 "Schematic description of the main parameters affecting the bubble dynamics for different bubble sizes."

Case	A	B	C
Flow pattern			
Recirculation	weak	intermediate	strong
Boundary Layer	present	weak	not present
Governing Effect	Viscosity	Viscosity, surface tension and gravity	Surface tension and gravity
Governing Dimensionless Numbers	Reynolds	Reynolds & Eotvos	Eotvos

5.2.2 A new correlation

In order to fine this governing correlation, many simulations with different liquid metals and initial bubble dimension has been carried out.

A grid sensitivity study has been conducted for all three metals. Overall using a grid of $D/dx = 16$ a relative error on the final velocity of less than 3 % has been observed. It has been noted that a coarse grid will generally lead to an underestimation of the rising velocity. The grid sensitivity study has been conducted for the biggest bubble for which the biggest shape deformation in expected. Therefore, considering the same R.E. for smaller bubbles, our analysis can be considerate conservative.

5.2.2.1   0.1 < Eo < 1

As it can be seen in Figure 14, the terminal Weber is a function of the Eotvos number only. Logically the Weber monotonously increases with the Eotvos since the inertia force are becoming more important than the superficial forces. Simulation of different metals with different viscosity coefficient and terminal velocity follow exactly the same trend. This is a proof of the irrelevance of the viscous forces acting on the bubble in this regime. The correlation which best fits the point is Eq. (5.22):
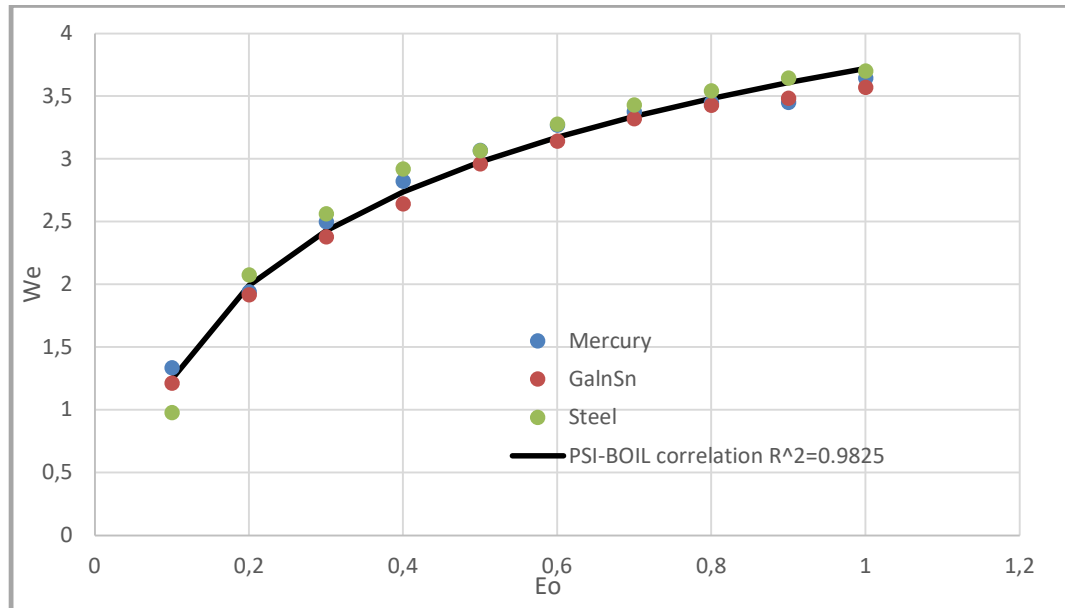
$$We = 1.0749 In(Eo) + 3.7212$$

(5.22)

$$R^2 = 0.9825$$

Figure 14 "Bubble terminal Weber vs. Eotvos (0.1<Eo<1)."

Once the velocity is known, the drag coefficient is calculated by the Lagrangian momentum balance equation, Eq. (5.24). In stationary condition, the bubble rise is determined by a balance between gravity, buoyancy and drag force.

$$\Delta\rho \cdot g \cdot \frac{\pi D^3}{6} = \frac{1}{2} C_D \cdot \rho \cdot u^2 \cdot \frac{\pi D^2}{4}$$

(5.23)

$$C_D = \frac{4}{3} \cdot \frac{\Delta\rho \cdot g \cdot D}{\rho \cdot u^2} = \frac{4}{3} \cdot \frac{Eo}{We} \tag{5.24}$$

In general the drag coefficient is a function of two dimensionless number, but since in liquid metals regime the Weber and Eotvos number are coupled, the drag coefficient is determined by 1 parameter only, Eq. (5.25).

$$C_D = \frac{4}{3} \cdot \frac{Eo}{We} = \frac{4}{3} \cdot \frac{Eo}{We(Eo)} = f(Eo) \tag{5.25}$$

From the CFD data, a correlation for the drag coefficient C_D is proposed (Figure 15) which tends to be strongly linear with the Eotvos, Eq. (5.26).

$$C_D = \frac{4}{3} \cdot \frac{Eo}{We(Eo)} \simeq \frac{4}{3} \cdot \frac{Eo}{1.0749\,In(Eo) + 3.7212} \simeq 0.2692 \cdot Eo + 0.0848 \tag{5.26}$$
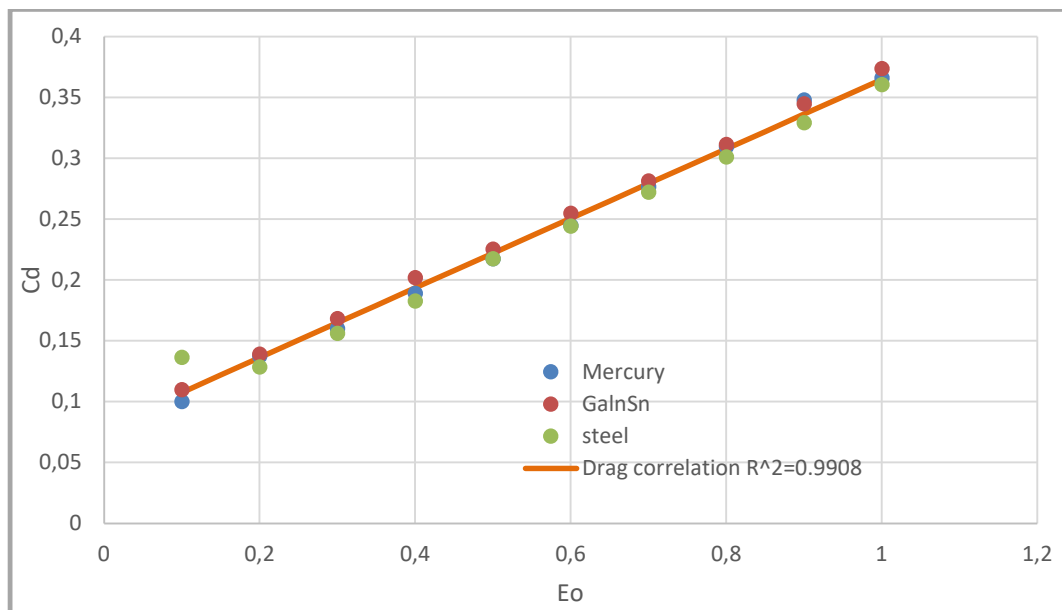
$$R^2 = 0.9908$$

Figure 15 "Bubble terminal Weber vs. Eotvos (0.1 < Eo < 1)."

All bubble considered (*Eo* < 1.2) are stable bubbles which reach a constant terminal velocity and whose shape progressively change from an initial sphere to an ellipsoid. Nevertheless, high Eotvos bubble (*Eo* > 1.2) tend to become unstable and to assume a wobbling disk shape. Their trajectory is not straight anymore, the terminal velocity is averagely constant but it experiments oscillation and the bubble shape is continuously deformed as a direct cause of the instable velocity. These bubbles act differently compared to stable bubble and the correlation mentioned above is not accurate anymore.

5.2.2.2   1<Eo<4

Simulation suggests that in $1 < Eo < 4$ region, the Weber number is weakly influenced by the Eotvos number, Eq. (5.27) and it is equal to 4.

$$We = 4 \qquad (5.27)$$

$$C_D = \frac{4}{3} \cdot \frac{Eo}{We} = \frac{1}{3} \cdot Eo \qquad (5.28)$$

5.2.2.3   E o> 4

For Eotvos number greater than 4, Mendelson's equation predicts pretty well the rising bubble velocity. Mendelson's equation tells that the bubble velocity is equal to gas-interface propagation wave velocity. This velocity is the sum of a surface tension and gravitational term.

$$u = \sqrt{\frac{2\gamma}{\rho_l D} + \frac{\Delta \rho g D}{2\rho_l}} \qquad (5.29)$$

Once we approach bigger bubble, the contribution of the gravity term becomes bigger and the surface tension smaller. At $Eo = 4$, the two terms count 50 % each and the Mendelson equation has it minimum point. For $Eo > 4$, the bubble is strongly flattened and the top of the bubble looks like more a gas-liquid interface. Therefore, the wave and bubble velocity are more likely to be the same and Mendelson theory precisely predict bubble velocity.

Mendelson theory is not able to predict carefully the terminal velocity for $Eo < 4$ because in this region, the surface tension term is the dominating parameter $\frac{2\gamma}{\rho_l D} > \frac{\Delta \rho g D}{2\rho_l}$ but the bubble is not completely spherical as described in the theory because it experiments axial compression. The surface tension wave velocity does not reflect real bubble velocity because bubble deformation is not taken into account in Mendelson theory.

$$C_D = \begin{cases} 0.2692 Eo + 0.0848 & for \ \ 0.1 < Eo < 1 \\ \dfrac{1}{3} Eo & for \ \ \ 1 < Eo < 4 \\ \dfrac{8}{3} \dfrac{Eo}{Eo + 4} & for \ \ \ \ \ \ Eo > 4 \end{cases}$$

5.2.3 Comparison between PSI-BOIL and experiments

Figure 16 and Figure 17 show the comparison of the terminal rising velocity between PSI-BOIL and the experiment of Mori [5] and Wang [6], respectively. On overall, the velocities predicted by PSI-BOIL are slightly higher than the experiments. This is considered to be caused by the presence of impurities in the metal, which is accumulated to the gas-liquid interface and reduces the rising velocity. A simulation, which can take into account the impurity, must be developed to obtain good agreement, but it is beyond the scope of this study.
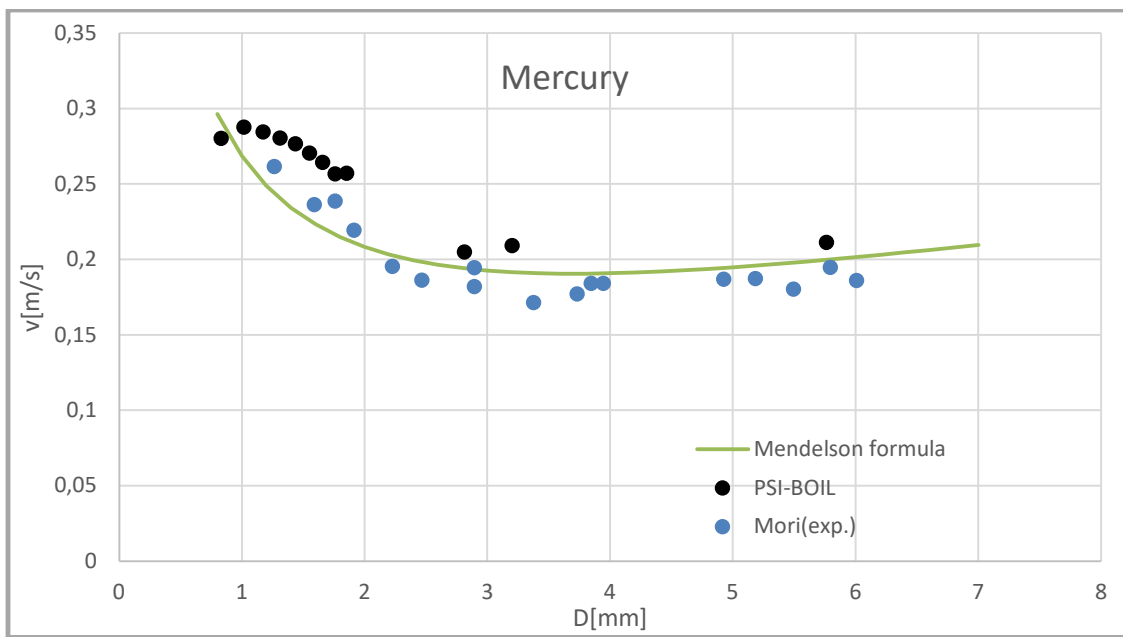

Figure 16 " Nitrogen bubble rising in Mercury. Analytic, numeric and computational comparison of the terminal velocity."
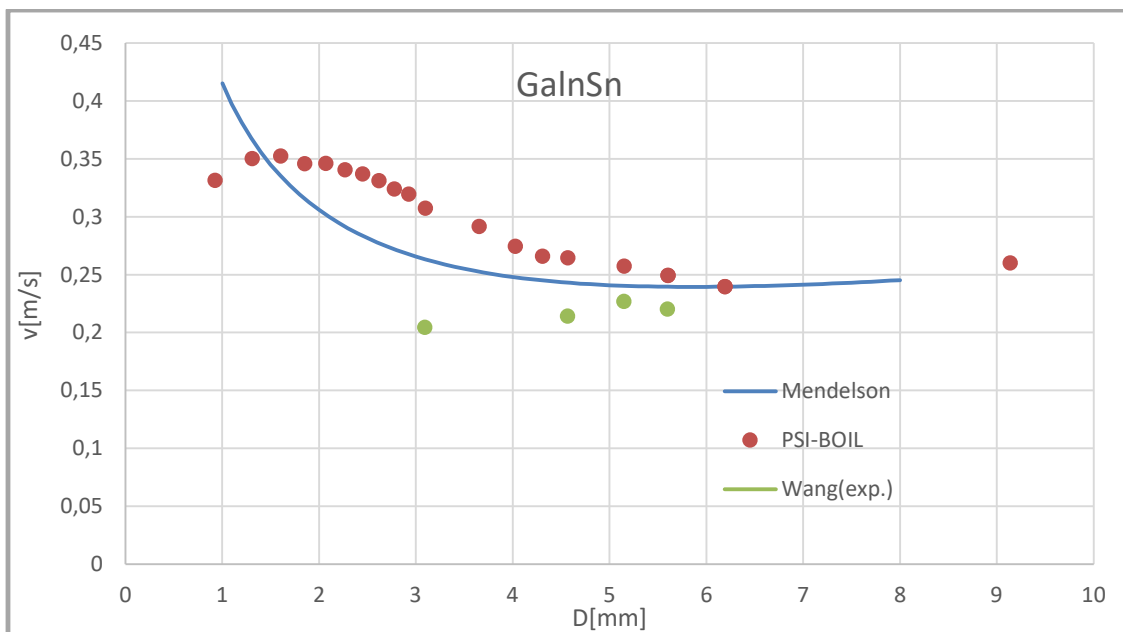

Figure 17 "Argon bubble rising in GaInSn. Analytic, numeric and computational comparison of the terminal velocity."

5.3 Instabilities of bubble

Enough larges bubbles tend to have instable behavior at some point in the raise (Figure 18). The trajectory in not anymore straight and the rising vertical velocity consequently decreased. No uniform velocity oscillation are present as a direct consequence of the bubble shape oscillation. The flow, therefore tends to be not axisymmetric anymore.
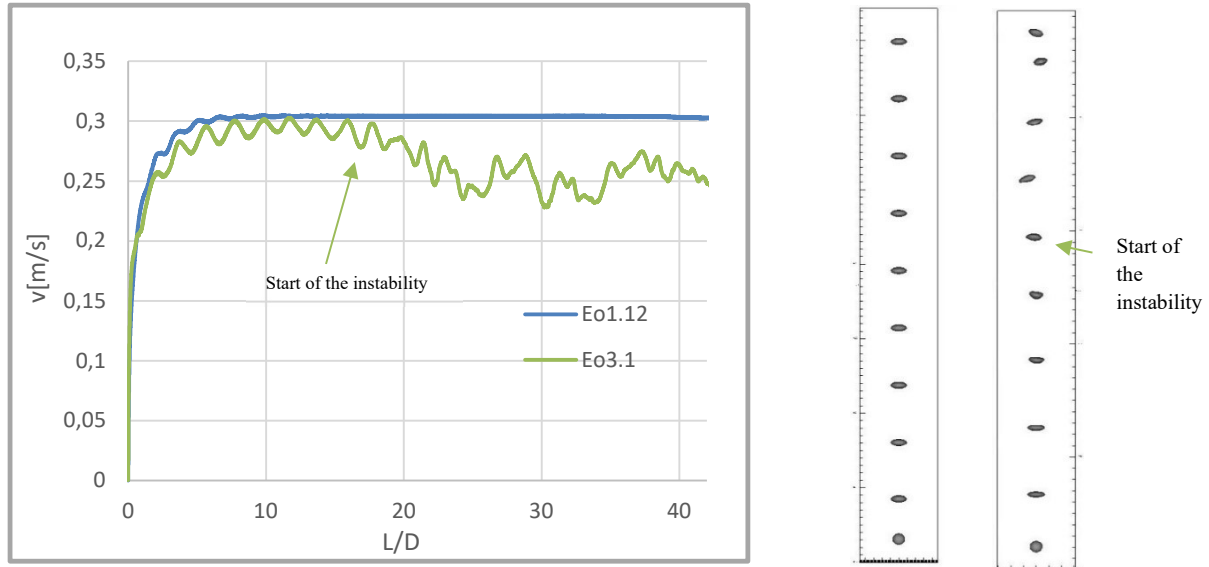

Figure 18 "Right: Velocity for Eo =1.12 and 3.1 bubbles without magnetic field. Left: x-z section of bubble trajectory (left: Eo= 1.12 right: Eo =3.1)."

In Grace diagram the line which separate the stable and unstable bubble region has a negative slope. This mean that for high Morton number, instabilities will occur for bigger Eotvos number while for low Morton materials instabilities happens earlier. Morton number can be consider a good parameter to quantify the stability of set of materials. From the definition, Morton number can be assumed as a ratio between viscous force over inertia and superficial forces. It is clear visible that the viscous forces tend to keep the system stable.

$$Mo = \frac{g \cdot \mu^4_c \cdot \Delta\rho}{\rho^2_c \cdot \gamma^3} = \frac{F_{viscous}}{F_{surf.tens} \cdot F_{inertia}}$$
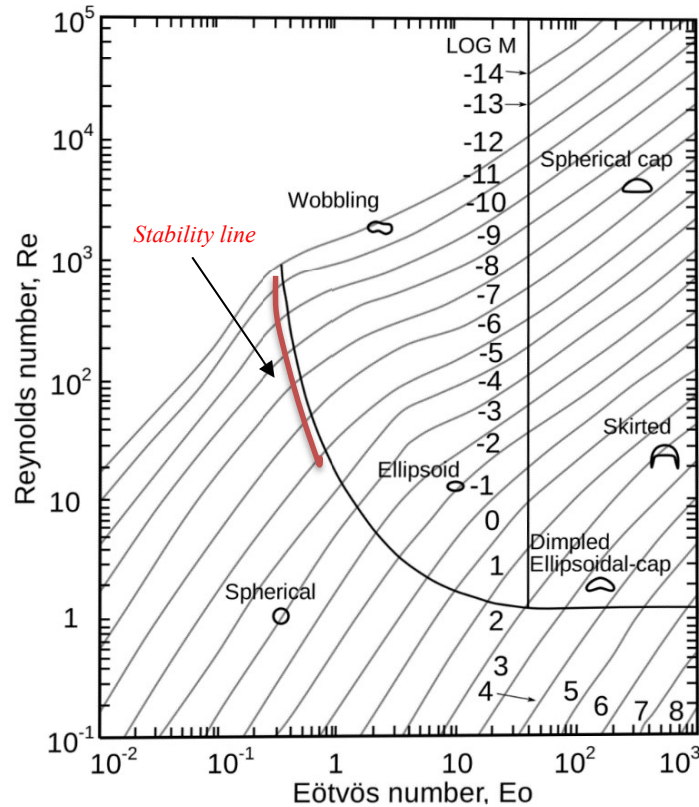
(5.30)

Figure 19 " Grace diagram."

In low Morton regions, such as liquid metal region, the line tends to be steeper (Figure 19). The Stability line is getting more and more independent to the Morton number and the Eotvos number at which instabilities occurs becomes a constant. In this region the viscous effect are negligible and the stability is controlled only by the balance of inertia and superficial forces (Weber number). Since Weber and Eotvos numbers are connected , the stability can be express also as a function of Eotvos number only.

$$Stability = f(\frac{F_{inertia}}{F_{surf.tension}}) = f(We(Eo)) = g(Eo)$$

(5.31)

The region in which the bubble passes to be a spherical-like body to a wobbling disc for different material proprieties in investigated. Figure 20 & Figure 21 suggest the transition happens almost at the same Eotvos number for all three metals (*Eo* = 1.7). This is a further proof this process in not influence by the Morton number because the viscosity effects are negligible compare to inertia and superficial ones.
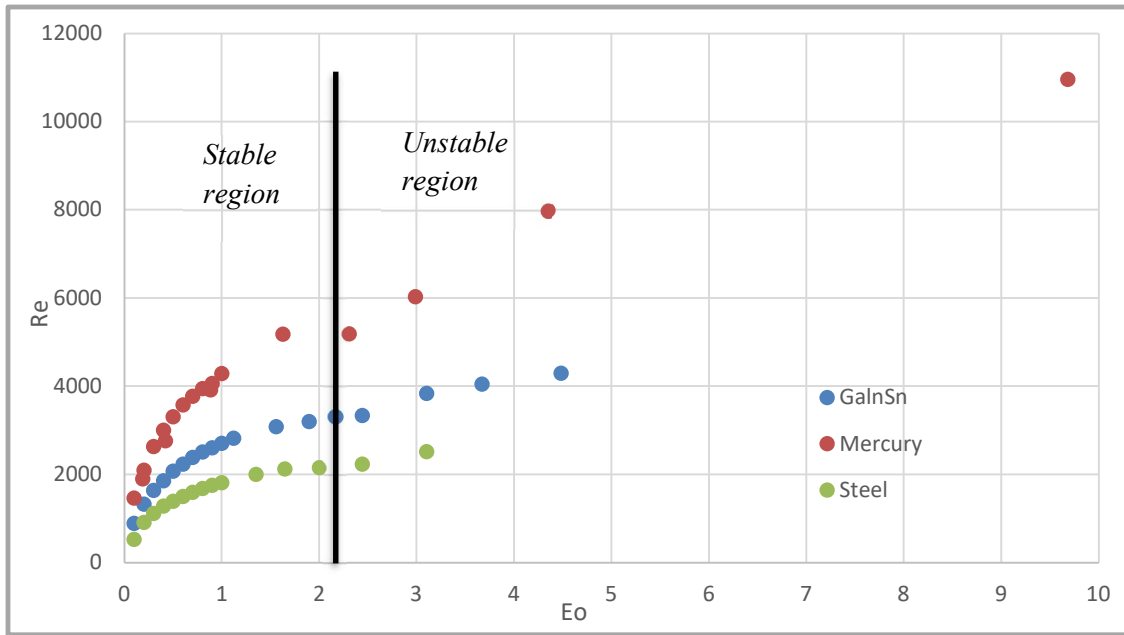
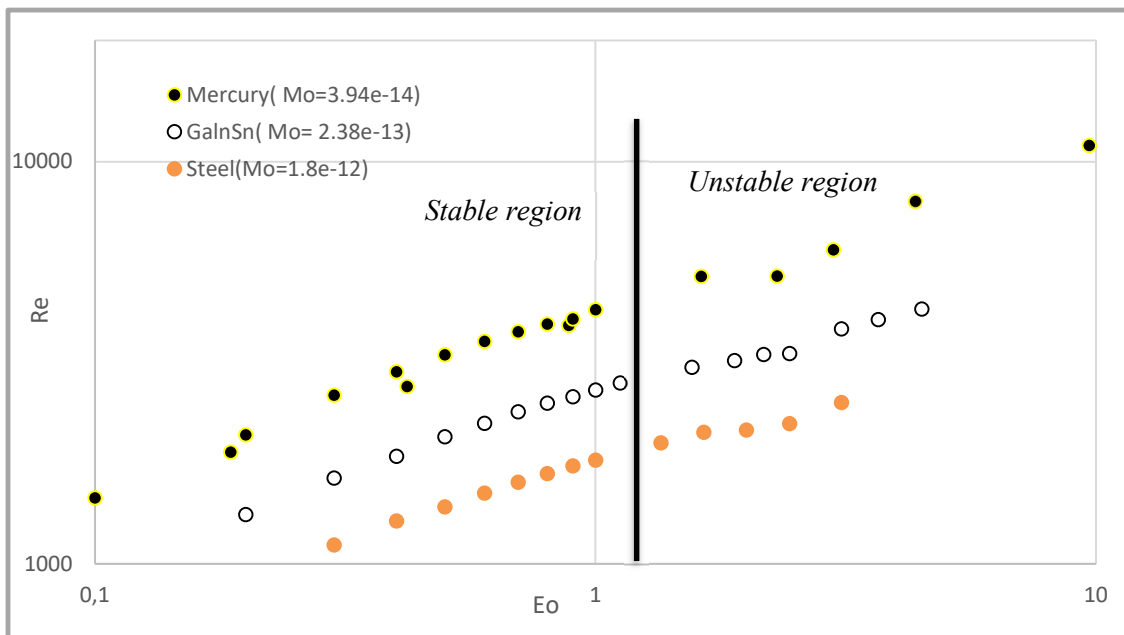*Figure 20 "Reynolds vs. Eotvos for different liquid metals."*

Figure 21 " Reynolds vs. Eotvos for different liquid metals."

6 Bubble shape without magnetic field

6.1 Introduction to the bubble aspect ratio

At the beginning of the simulation, the bubble starts to deform from a sphere in a quiescent liquid. Due to the unbalance of the gravity force and buoyancy, the bubble starts to rising by increasing the rising velocity. Figure 22 shows the velocity field observed from the Lagrangian point of view. The increase of the bubble velocity influence the pressure field on the bubble surface. The pressure on the top and on the bottom of the bubble is increased because of the decreases of the velocity. Kinematic energy is transferred into pressure. On the side of the bubble in order to preserve the volume flow, the velocity is increased producing a tunneling effect which decreases the local pressure. The new pressure filed compress the bubble on the top and on the bottom, while it elongates on the side, as illustrated in Figure 23. The macroscopic effect is the compression of the bubble which passes from a spherical shape to an ellipsoidal one.
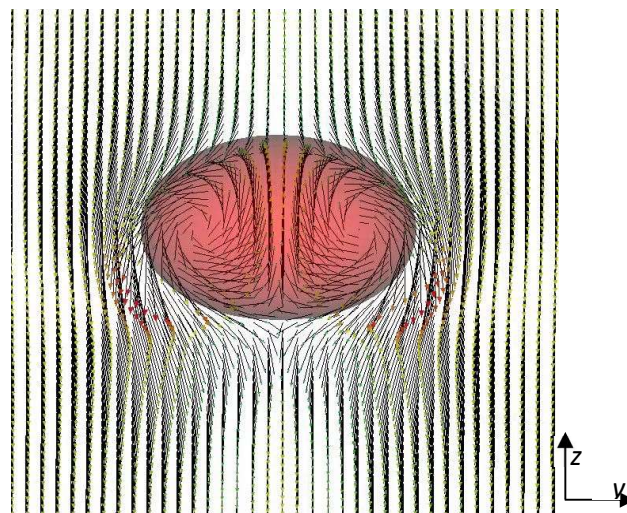

Figure 22 "Lagrangian bubble velocity field in liquid steel (D=3mm)."
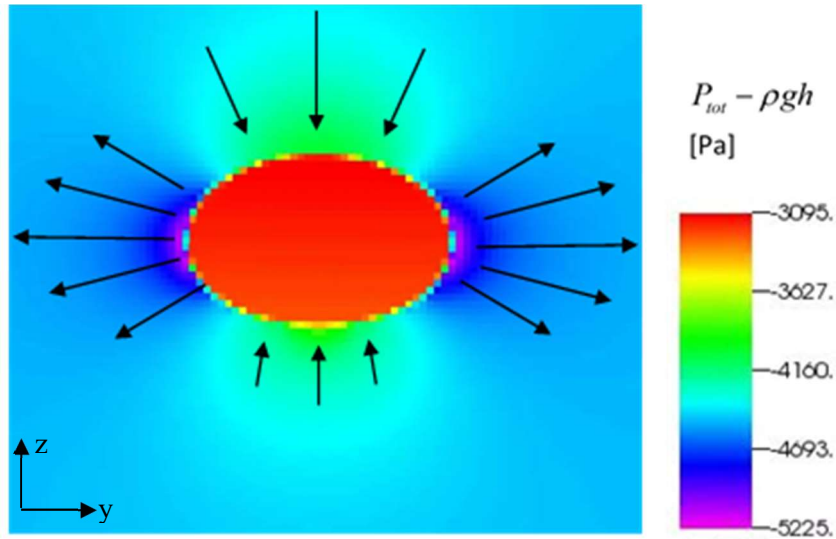
Figure 23 "Kinematic pressure field (P.tot-ρgh) around a rising bubble in liquid steel (D=3mm)."

Moore[16] proposed a simple correlation for the bubble aspect ratio X which is valid for spherical-like bubbles and loses its applicability for higher Weber numbers:

$$\chi = 1 + \frac{9}{64} \cdot We + O(We^2)$$

(6.1)

Hartunian and Sear [16] assumed that the finals bubble shape is an ellipsoid and resolve the Euler problem under different and more general conditions. The solution described in Eq. (6.2) demonstrates that Moore theory is valid only for small range of Weber number (*We* < 1.125).

$$We = 4 \cdot \chi^{-\frac{4}{3}} \cdot \left(\chi^3 + \chi - 2\right) \cdot \left[\chi^2 \cdot \sec^{-1} \chi - \left(\chi^2 - 1\right)^{\frac{1}{2}}\right]^2 \cdot \left(\chi^2 - 1\right)^{-3}$$

(6.2)
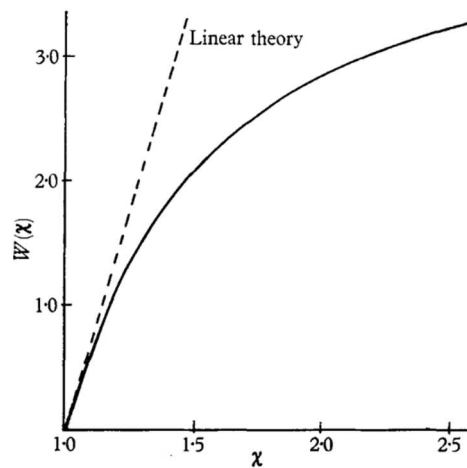
Figure 24 "Weber as function of the aspect ratio for the linear (More) and non linear (Hartunian & Sear) theory."

In the following section, we propose a new semi-analytical method for the aspect ratio of the bubble rising in liquid metals without the magnetic field.

6.2 Analytical theory

6.2.1 Force balance and curvature

Once the bubble has reached its terminal velocity, the acceleration of the system is zero and the bubble and all its components are in a momentum equilibrium $\left(\sum F = 0\right)$. The force balance of a bubble interface is proceed by knowing the inner and the outer pressure as illustrated in Figure 25.

Figure 25 "Force balance on the bubble interface."

The outer pressure is found by applying the Navier-Stokes equations along a streamline from the non-perturbed region to the interface, Eq. (6.3). Since the viscous effect is negligible, the flow field can therefore approximated as an irrotational field $\left(\nabla \times \vec{u} = 0 \rightarrow \vec{u} = \nabla \phi \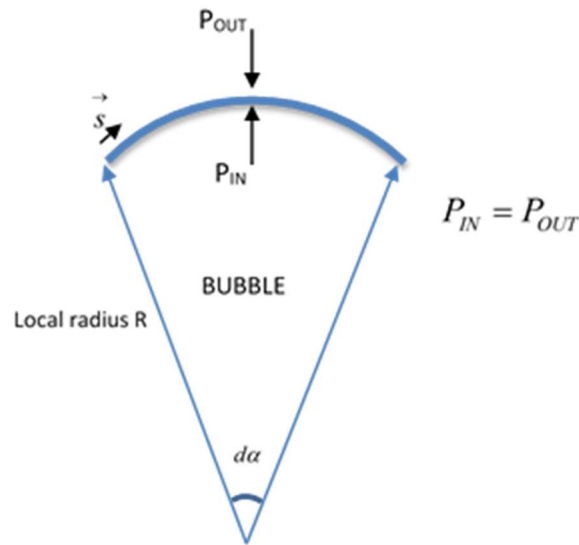right)$. Energy inside the fluid is conserved and the velocity admits a potential field ϕ. The total outer pressure is the sum of the gravitational pressure $\rho g h$, the kinematic pressure $\frac{1}{2}\rho\left(u_\infty^2 - u^2\right)$ and the local extra pressure due to the curvature of the bubble $\gamma\chi$. The gravitation force is not technically constant since it depends on the depth of the liquid but for simplification is set constant to $\rho g h$ with h the depth of the bubble center of mass. Assuming that the fluid is almost perfect inviscid, there is not any interface boundary layers and the interface tangential liquid velocity is not zero $\left(u_{//}(s) \neq 0, u_r(s) = 0 \right)$.

$$p_{out}(s) = \rho g h + \gamma\chi(s) + \frac{1}{2}\rho\left(u_\infty^2 - u^2(s)\right) \tag{6.3}$$

Applying the Navier-Stokes equations to the inner gas, the inner pressure is easily computed. Essentially, the pressure field inside the bubble is spatially constant $\nabla p = 0$.

Once the bubble has reached its terminal velocity, the shape is kept constant which means that the bubble curvature in each point is kept constant. In the same way, the velocity field across the bubble does not change. During the bubble raise up, the gravitational term linearly decreases since the depth is decreasing $\rho g [h - u_\infty \cdot t]$. In order to keep the system stable also the inner gas pressure decreases in

order to provide momentum stability at each time. Therefore, the term $p_{in}(t) - \rho g h(t)$ is a constant during the raise.

$$\chi(s) = \frac{+\frac{1}{2}\rho u^2(s) + \rho g h - P_{IN} - \frac{1}{2}\rho u_{\infty}^2}{\gamma}$$

(6.4)

Eq. (6.4) suggests the local interface curvature is linearly dependent on the kinematic pressure and inversely proportional to the surface tension coefficient. For each point of the interface $\rho g h - p_{in} - \frac{1}{2}\rho u_{\infty}^2$ is constant. Therefore, the driven factor for the computing the curvature, is the interface tangential velocity field $u_{//}(s)$. For the ideal resolution of the bubble shape problem, inviscid Euler equations have to be solved around the bubble in order to find out the tangential velocity $u_{//}$ to the surface which is needed in order to calculate the bubble curvature $\chi(s)$ according the Eq. (6.4).

Here it is proposed an equivalent method which avoids the solution of the Euler equations in ellipsoidal coordinates and provides an accurate correlation for stable ellipsoidal bubbles in inviscid liquid.

Let's consider the bubble at the first instant in which it is quiescent and has a perfect spherical shape. In this situation the velocity field is zero and the main driven force is the Archimedes force which is produced by the different hydrostatic pressure on the top on the bottom of the bubble.
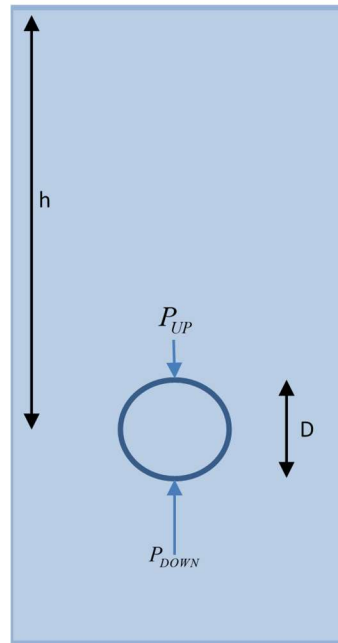
$$P_{UP} = \rho g \cdot \left(h - \frac{D}{2} \right)$$

$$P_{DOWN} = \rho g \left(h + \frac{D}{2} \right)$$

Figure 26 "Static pressure acting on the bubble."

Nevertheless, for the shape calculation the hydrostatic pressure is set for simplicity equal to $\rho g h$ on all the interface since $h \gg D$ and the relative difference between P_{UP} and P_{DOWN} is negligible (Figure 26). Setting hydrostatic pressure constant is a reasonable approximation for computing the bubble shape. It cannot be assumed in the momentum balance equation because the difference between the up and the bottom hydrostatic pressure is the driving factor of the bubble rise. By the balance of the forces acting on the surface at $t = 0$ (Figure 27) it can be established that the $p_{out} - \rho g h$, which is previously demonstrated to be kept constant during the bubble raise, is equal to the initial curvature over-pressure $\gamma \chi_0$.

$$p_{in} - \rho g h = \gamma \chi_0 \tag{6.5}$$

$$P_{IN} = P_{OUT} = \gamma \chi_o + \rho g h$$

$$P_{IN} - \rho g h = \gamma \chi_o = \frac{4\gamma}{D}$$
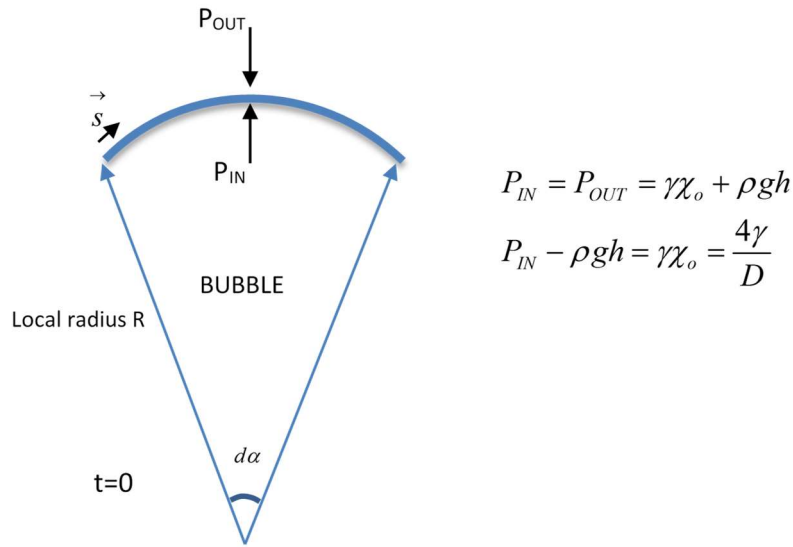
Figure 27 " Force balance on bubble interface at t=0."

Using Eq. (6.4) and Eq.(6.5), the final balance equation on the interface Eq. (6.6) tells how the local curvature behaves. It is equal to an initial constant value plus a kinematic pressure dependent value. It is clear that the velocity field is the only factor which influences the local bubble curvature. Regions with high kinematic pressure result in low curvature interface and vice-versa. Ideally the velocity field $u(s)$ can be found by solving the Euler equations for the ellipsoidal shape which clearly depends on the bubble local curvature $u(s) \rightarrow u(s, \chi(s))$. This tends to become a complex and long process.

$$\gamma \chi (s) = \gamma \chi_o + \frac{1}{2}\rho \left(u^2 (s) - u_\infty^2 \right)$$

(6.6)

6.2.2 Curvature at the top of the bubble

In our analysis the bubble shape is to be considered to be a perfect ellipsoid $\left(\dfrac{x^2}{a^2} + \dfrac{y^2}{b^2} + \dfrac{z^2}{c^2} = 1 \right)$. Since the flow is axisymmetric the bubble shape in x and y directions is the same $(a=b)$ and the ellipsoid can be perfectly characterized by only parameters *a* and *c*. In order to characterize the problem it will be necessary to solve the curvature equation on only two different points of the bubble since there are only 2 unknowns. The first point considered is the bubble stagnation point in which the kinematic pressure is the highest, Eq. (6.7). Here the fluid stops and all the kinetic energy in transmuted into pressure. It is a quite smart point to choose because the velocity is zero for every bubble shape.

$$\chi_{min} = \chi(\theta = 0) = \chi_o - \frac{1}{2}\frac{\rho \cdot u_\infty^2}{\gamma}$$

(6.7)

6.2.3 Curvature at the side of the bubble

The second point considered is the one with the highest curvature which takes place at the angle of $90°$, the curvature being defined as:.

$$\chi_{max} = \chi\left(\theta = \frac{\pi}{2}\right) = \chi_o + \frac{1}{2}\frac{\rho}{\gamma} \cdot \left(u^2\left(\frac{\pi}{2}\right) - u^2_\infty\right)$$

.   (6.8)

Here the fluid velocity, in order to satisfy the volume conservation $(\nabla \cdot u = 0)$, is increased with the consequence of producing a negative kinematic pressure on the interface which pulls out the bubble. Since only the biggest and the smallest curvature are need, how the tangential velocity is behaving in each other point is not of our interest. The major problem is finding out the tangential velocity at $90°$.

6.2.4 Tangential velocity field

First, by the solution of the Euler equations in spherical coordinates (Figure 28), it can be seen that on the interface only the tangential component of the velocity is present and not the radial one. In a perfect spherical case $u_{//}\left(\frac{\pi}{2}\right) = \frac{3}{2}u_\infty$.
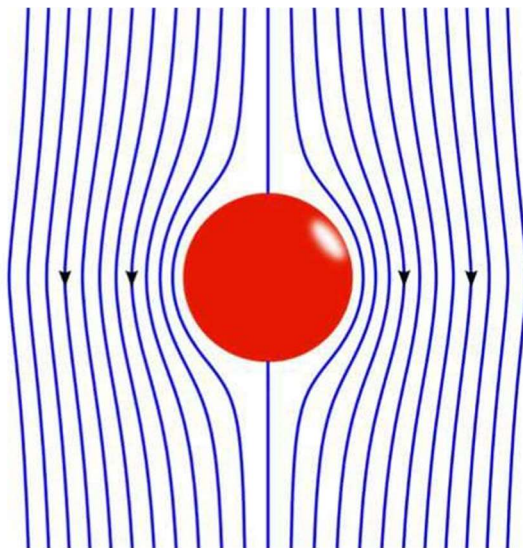
Euler incompressible Equations

$$\nabla \cdot u = 0$$

$$\rho \cdot \frac{\partial u}{\partial t} + \rho \cdot (u \cdot \nabla)u = -\nabla p + \rho g$$

Velocity field:

$$u_r(r,\theta) = u_\infty\left(1 - \frac{R^3}{r^3}\right)\cos(\theta)$$

$$u_{//}(r,\theta) = -u_\infty\left(1 + \frac{R^3}{2r^3}\right)\sin(\theta)$$

Figure 28 "Streamline of inviscid fluid around a sphere."

In the ideal case the tangential velocity decreases $\left(\propto \frac{1}{r^3}\right)$ from $\frac{3}{2}u_\infty$ to u_∞ moving away from the sphere. An equivalent model is used for the ellipsoidal bubble in which for a certain range the velocity is uniformly constant and equal to the interface tangential velocity (Figure 30). We assume that after a

certain distance the flow is not anymore perturbed by the presence of the sphere. Nevertheless, in the perturbed region, the velocity is considered spatially uniform and equal to the interface tangential velocity. By an integral volume flowrate conservation (Figure 29), the ideal "perturbed range" can be found for a spherical bubble and it is equal to $\sqrt{3} \cdot R$.
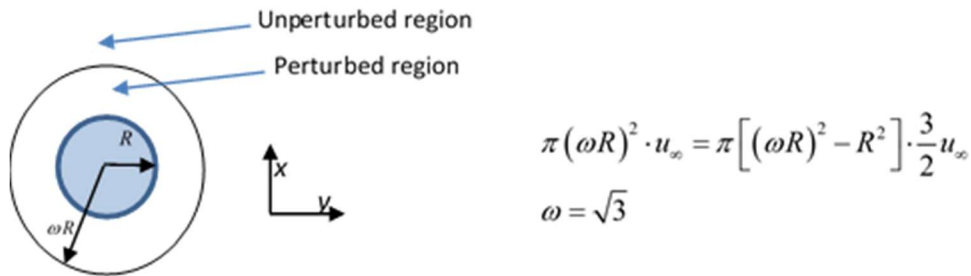

$$\pi \left(\omega R \right)^2 \cdot u_\infty = \pi \left[\left(\omega R \right)^2 - R^2 \right] \cdot \frac{3}{2} u_\infty$$

$$\omega = \sqrt{3}$$

Figure 29 "Top view of the bubble."
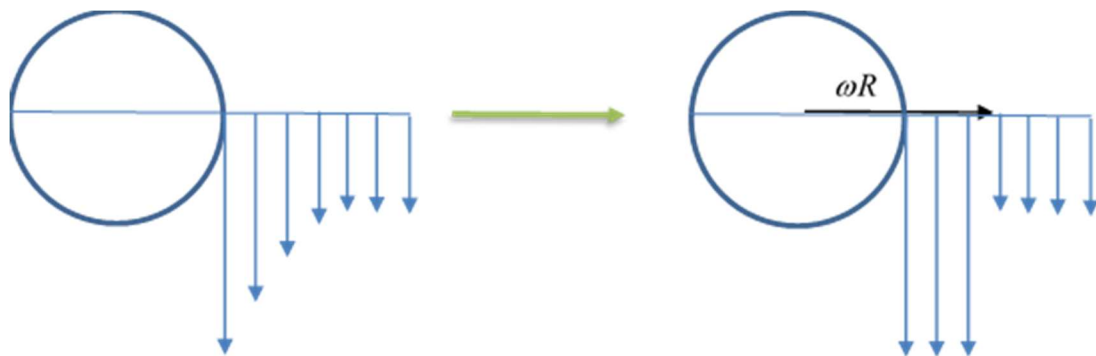
Figure 30 "Difference between real velocity field and modeled one for a spherical body."

This approach is used also for ellipsoidal bubble but with some geometrical corrections. The width of the bubble a will be dependent on its characteristic diameter $\left(D = \sqrt[3]{\dfrac{6 \cdot V_{tot}}{\pi}} \right)$ and also on the bubble aspect ratio $\left(X = \dfrac{a}{b} \right)$. Using the current definitions and assuming the bubble volume does not change in the compression, the width is found as a function of the initial diameter and the aspect ratio.

$$a = D \cdot \sqrt[3]{\frac{X}{8}}$$

(6.9)

Volume flowrate conservation Eq. (6.10) is applied to the ellipsoidal bubble (Figure 31) in order to discover the liquid side velocity $u\left(\dfrac{\pi}{2} \right)$, Eq. (6.11).

$$\pi(\omega a)^2 \cdot u_\infty = \pi\left[(\omega a)^2 - a^2\right] \cdot u\left(\frac{\pi}{2}\right)$$

(6.10)

$$u\left(\frac{\pi}{2}\right) = u_\infty \cdot \frac{\omega^2}{\omega^2 - 1}$$
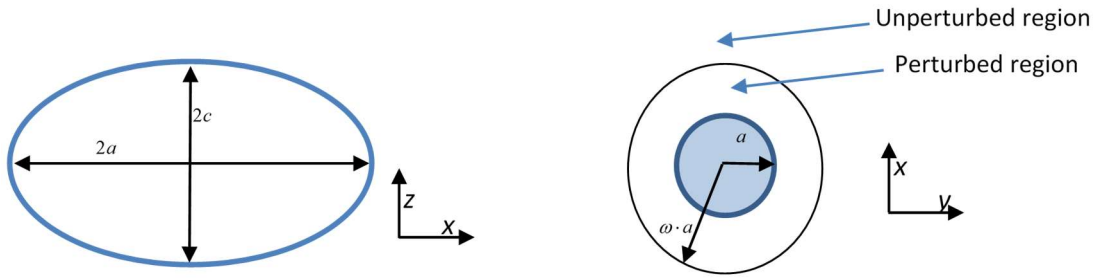
(6.11)

Figure 31 *"On the left, side representation of the ellipsoidal bubble, on the right top view of the ellipsoidal bubble."*

In the ellipsoidal case, finding out ω is the key point since it is known at priory only in the spherical case. We assume ω is a function of the shape factor X. It is every time greater than unity and it is $\omega(X = 0) = \sqrt{3}$.

We generally know that in more distorted bubbles, $u_{//}\left(\frac{\pi}{2}\right)$ is higher since amore amount of fluid is bend by the bubble presence and it entirely flow on the slide of the bubble $\frac{\partial u(\pi/2)}{\partial X} > 1$. Terminal bubble velocity u_∞ slightly decreases with the shape factor since for more distorted bubbles the drag coefficient is higher: $\frac{\partial u_\infty}{\partial X} > 1$. Therefore, according to Eq. (6.12), $\omega^2/(\omega^2 - 1)$ has to increase with X. By solving the last term, it is proved that the $\omega(X)$ monotonously decreases with X Eq. (6.13). Furthermore $\omega(X)$ reaches 1 only asymptotically.

$$\partial \frac{\frac{\omega^2}{\omega^2 - 1}}{\partial X} = \frac{2\omega \cdot \frac{d\omega}{dX} \cdot (\omega^2 - 1) - \omega^2 \cdot 2\omega \cdot \frac{d\omega}{dX}}{(\omega^2 - 1)^2} = \frac{\frac{d\omega}{dX} \cdot (-2\omega)}{(\omega^2 - 1)^2} > 0$$

(6.12)
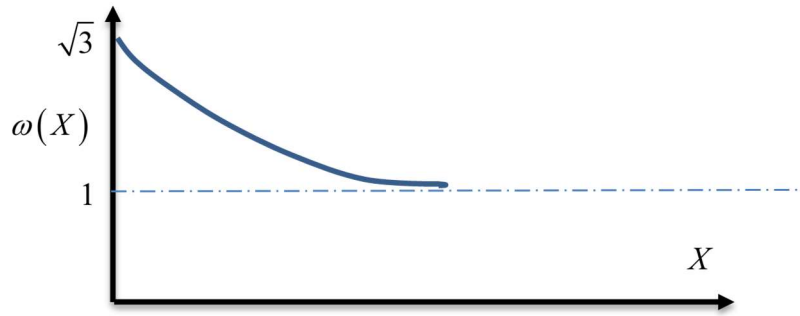
$$\frac{d\omega}{dX} < 0$$

(6.13)

Figure 32 "Possible omega function."

For practical calculation it is guess that the $\omega(X)$ follow a decrease proportional to $\dfrac{1}{X^n}$ as can be seen in Eq. (6.14). Under this assumption, the function is controlled by the n parameter which is an unknown .The n represent how fast the function tends to 1. It is a free parameter and it is guessed by comparison between theory and PSI-BOIL simulation.

$$\omega(X) \approx \frac{\left(\sqrt{3}-1\right)}{X^n}+1$$

(6.14)

6.2.5 Curvature Calculation.

Following the previous consideration the higher curvature Eq. (6.15) and the lowest curvature Eq. (6.16) can be calculated which correspond respectively at $\dfrac{\pi}{2}$ and 0 angle.

$$\chi_{max} = \chi\left(\frac{\pi}{2}\right)=\frac{4}{D}-\frac{1}{2}\cdot\frac{\rho\cdot u_\infty^2}{\gamma}\cdot\left(1-\left(\frac{\omega^2(X)}{\omega^2(X)-1}\right)^2\right)$$

(6.15)

$$\chi_{min} = \chi(0)=\frac{4}{D}-\frac{1}{2}\cdot\frac{\rho\cdot u_\infty^2}{\gamma}$$

(6.16)

From the differential calculus, the analytical expression of the aspect ratio of an ellipsoid can be found (Figure 33). In our case the velocity filed and the bubble shape are axisymmetric. There is no

dependence of any variable on $0 < \varphi < 2\pi$. The bubble is deformed in the same way on y and x direction, so $a = b$.
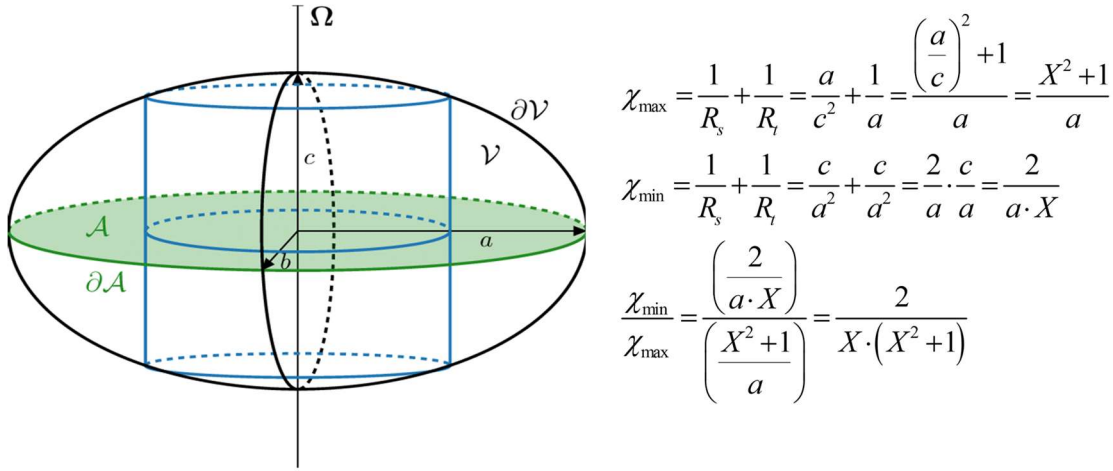

$$\chi_{\max} = \frac{1}{R_s} + \frac{1}{R_t} = \frac{a}{c^2} + \frac{1}{a} = \frac{\left(\frac{a}{c}\right)^2 + 1}{a} = \frac{X^2 + 1}{a}$$

$$\chi_{\min} = \frac{1}{R_s} + \frac{1}{R_t} = \frac{c}{a^2} + \frac{c}{a^2} = \frac{2}{a} \cdot \frac{c}{a} = \frac{2}{a \cdot X}$$

$$\frac{\chi_{\min}}{\chi_{\max}} = \frac{\left(\frac{2}{a \cdot X}\right)}{\left(\frac{X^2 + 1}{a}\right)} = \frac{2}{X \cdot \left(X^2 + 1\right)}$$

Figure 33 " Left: ellipsoidal representation of the bubble. Right: relation between bubble aspect ratio and top-side curvatures."

Substituting in the last formula the definition of max. and min. curvature for bubbles, an explicit correlation between the Weber number and the bubble aspect ratio is found. This a proof that in inviscid fluids, the bubble deformation is controlled only by the ratio between inertia and surface tension forces.

Let define $F(X)$ as Eq.(6.17) for compactness.

$$F(X) = \frac{\omega^2(X)}{\omega^2(X) - 1} \tag{6.17}$$

$$\frac{\chi_{\min}}{\chi_{\max}} = \frac{2}{X \cdot \left(X^2 + 1\right)} = \frac{4 - \frac{1}{2} \cdot \frac{\rho \cdot u_\infty^2 \cdot D}{\gamma}}{4 - \frac{1}{2} \cdot \frac{\rho \cdot u_\infty^2 \cdot D}{\gamma} \cdot \left(1 - F^2(X)\right)} \tag{6.18}$$

$$\frac{\chi_{\min}}{\chi_{\max}} = \frac{2}{X \cdot \left(X^2 + 1\right)} = \frac{4 - \frac{1}{2} We}{4 - \frac{1}{2} We \cdot \left(1 - F^2(X)\right)} \tag{6.19}$$

$$We = \frac{16 - 8X \cdot \left(X^2 + 1\right)}{2 \cdot \left(1 - F^2(X)\right) - X \cdot \left(X^2 + 1\right)} \tag{6.20}$$

Once the $\omega(X)$ is estimated, the correlation can be successfully used in Eq. (6.20). If we linearized the function in the surroundings of X=1, the Moore linear correlation is found.

Essentially, the omega function cannot be known at priori unless the Euler equations are analytically solved in ellipsoidal coordinates. This formula is valid until the bubble shape can be considered an ellipsoid. When the top curvature becomes zero, the ellipsoidal aspect ratio mathematically diverges to infinity. In order to keep this theory valid the top curvature has to be greater than zero Eq. (6.21). This condition is achieved is the bubble Weber number is less than 8 Eq. (6.22). Practically this limit is never reached because the bubble becomes instable much sooner $(We \sim 4)$.

$$\chi_{TOP} = \frac{4}{D} - \frac{1}{2} \cdot \frac{\rho \cdot u_\infty^2}{\gamma} \gg 0$$

(6.21)

$$We \ll 8$$

(6.22)

6.3 Comparison of the aspect ratio between analytical solution and PSI-BOIL

The following analytical solution has been compared with CFD results in order to determine the N parameter which fully characterizes the omega function $\omega(X)$. The aspect ratio X has been calculated for 30 simulations for 3 different sets of materials (Argon+Steel, Argon+GaInSn and Nitrogen+Mercury) within the range of $0.1 < Eo < 1$.

Unfortunately, the bubble shape is more sensitive on the grid size compared to terminal velocity. Shape factor relative error clearly depends on the ratio $\dfrac{\Delta x}{R_{min}} = \Delta x \cdot \chi_{max}$ which represents how well the grid manage to represent the bubble interface in the point with the highest curvature which is on the side of the bubble.

Grid sensitivity studies have been conducted for $Eo = 0.5$ bubble and the relative error on shape factor is almost 10% compare to a ultrafine grid simulation. Furthermore, it has been observed that the lack of accuracy of the grid leads always to an underestimation of the shape factor only. Even if the relative error should be lower for small bubbles, since they are less stretched, a conservative analysis has been adopted and a 10% relative error has been set for all the points.

The best interpolation is found for $N = 1.34$.

$$\omega(X) \approx \frac{\left(\sqrt{3}-1\right)}{X^{1.34}} + 1 \tag{6.23}$$

$$F(X) = \frac{\omega^2(X)}{\omega^2(X)-1} \tag{6.24}$$

$$We = \frac{16 - 8X \cdot \left(X^2 + 1\right)}{2 \cdot \left(1 + F^2(X)\right) - X \cdot \left(X^2 + 1\right)} \tag{6.25}$$

Eq.(6.25) precisely predicts bubble shape in inviscid regime (Figure 34). It is applicable to bubble rising in liquid metal for $0 < Eo < 1.2$. Above $Eo = 1.2$ the bubble becomes unstable, the shape is not anymore ellipsoidal and the theory in not anymore valid.
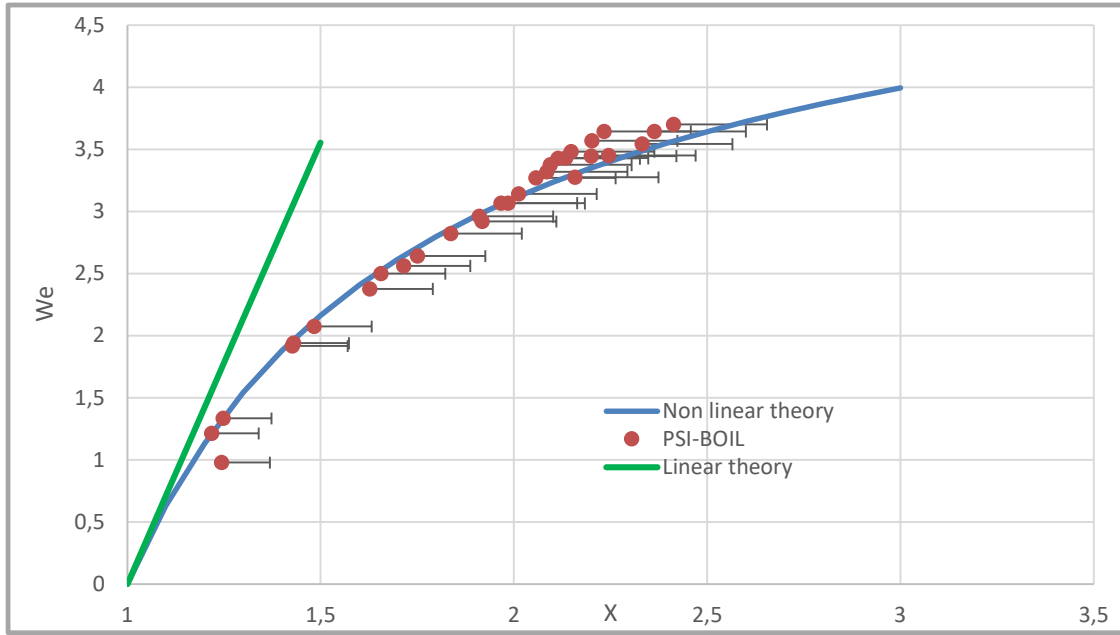
Figure 34 "Comparison between linear and non linear theory for inviscid liquid."

6.4   Bubble theory validity

In chapter 4, it is explained that the flow in the upstream of the detachment point can be modeled inviscid since the kinematic pressure is much larger than the viscous pressure. After the detachment point, viscosity effect are not anymore negligible and has to be taken into account. The pressure on the bubble is not equal only to the kinematic pressure but a viscous term appears with the effect to decreases the total pressure. For simplicity in the bubble dynamics it is assumed that in all interface points under the detachment point the velocity field does not produce any pressure change on the bubble surface. Physically it is assumed that all energy produced by the liquid deceleration is dissipated by viscous friction.

In reality, the pressure field on the bottom of the bubble is slightly different (Figure 35). Simulation shows that friction loses pressure energy mostly on region A while the pressure on region B seems to be higher and equal to the top bubble one. Therefore, it can be assumed that only on the region B the viscous pressure is negligible and the total pressure depends only on the kinematic and gravity term. Therefore $p_{tot} - \rho gh$ of the bottom point of the bubble is the same of the top point of the bubble. Both of them are equal to the kinematic pressure $\frac{1}{2} \rho u_\infty^2$.
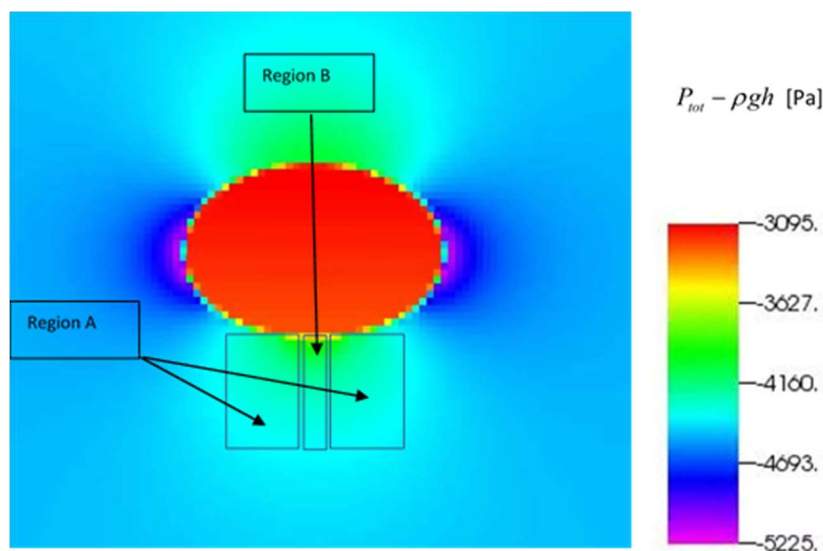

Figure 35 " Pressure field (Ptot-ρgh) around a rising bubble in liquid steel (D=3mm)."

Figure 36 represents well the real pressure distribution $p_{tot} - \rho gh$ on the bubble surface. As it can be seen, there is a pick of pressure on the bottom of the bubble (region B). This local tiny overpressure does not influence the bubble dynamics since the area considered is little and it is neglected in the force

balance equation. Nevertheless, it is determining to explain why the inviscid bubble shape theory works sufficiently well for bubbles in liquid metals.

In shape theory, the bubble is assumed to be an ellipsoid. Therefore, it has been assumed that top and bottom curvature of the bubble are equal. Even though pressure field on the upper side of the bubble is different compared to pressure field on the bottom side of the bubble, the local pressure on the highest and lowest point of the surface are equal. Since the pressure is the same, the curvature is the same and bottom and top curvature can logically be assumed equal.

$$\chi_{BOTTOM} = \chi_{TOP}$$

(6.26)

For the bubble shape theory, curvature on the top, bottom and side have to known. Bubble local curvature can be computed only if outer pressure is known. In general viscous regime, the outer pressure cannot be computed at priori because of the viscous pressure $\left(\mu \int_{\infty}^{s} \nabla^2 u \cdot dr \right)$. Fortunately the non-viscous approximation can be applied for the three points needed for the shape theory (the top, the side and the bottom of the bubble).
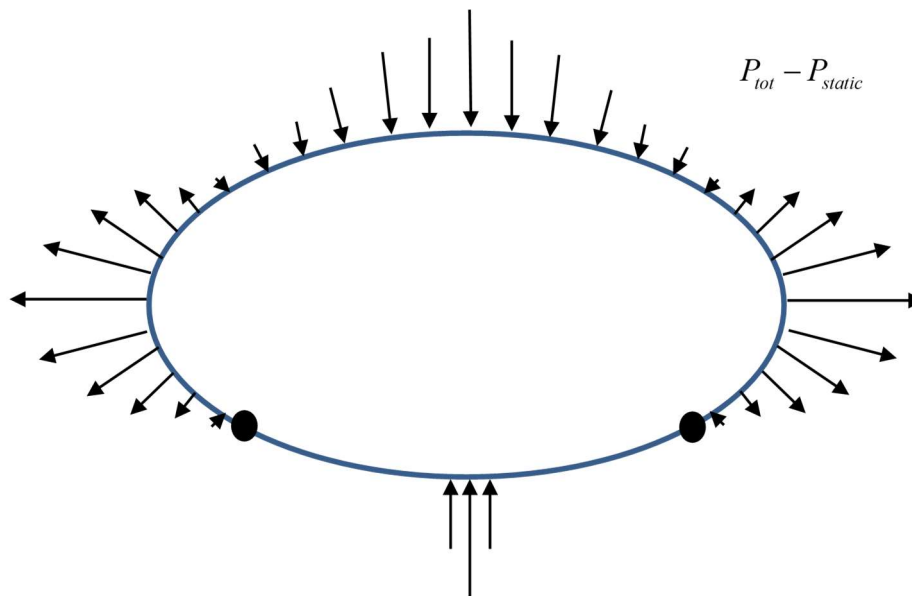

Figure 36 " Pressure field (P.tot-P.static) on bubble surface."

7 Bubble behavior in liquid metals with external magnetic field

7.1 Phenomena description

A qualitative description of the main variables of the bubble rising problem are presented. The purpose is to underline the main difference between the MHD bubble rising compared to the simple bubble rising problem and to understand how magnetic field influence bubble dynamics.

7.1.1 Velocity profile

Initially the bubble is in a quiescent situation. Due to the density difference the bubble starts to go up. During the raise-up of the bubble, a circular velocity field is produced inside and outside the bubble due to the exchange of momentum from the gas to the surrounding liquid. Figure 37 shows the velocity field is not axisymmetric anymore if an external magnetic field is applied. Recirculation process is dampened on the x sides (magnetic field direction) of the bubble.
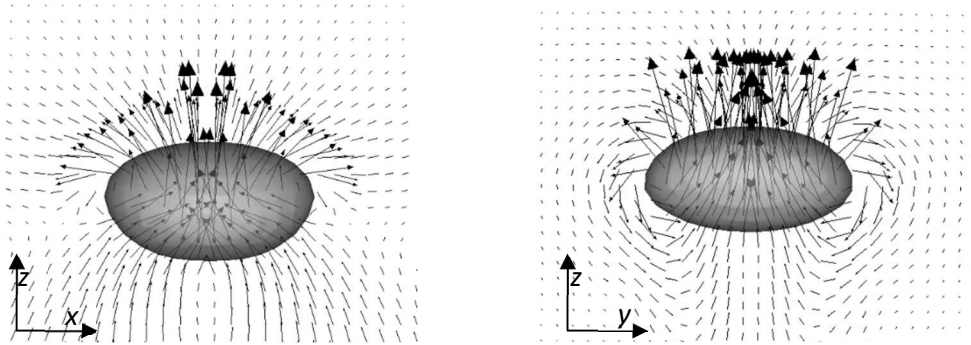

Figure 37 "Right: x-z section of Eulerian velocity profile. Left: y-z section of Eulerian velocity profile, D=3.86 mm."

7.1.2 Current density J and electric potential ϕ

Liquid metal can be considered as an excellent conductor, therefore it can be assumed that localized charge density cannot be changed and it remains zero during all the simulation ($\nabla \cdot J = 0$). An electric field E is created in order to guarantee $\nabla \cdot J = 0$.

Technically, at the beginning the Lorentz force produces a current density inside the liquid metal $J = \sigma(u \times B)$. The current density, since it is an electron flow, produces positive and negative electric change regions due to the lack and the excess of electrons. This charge density field produced, according to Coulomb law, an electric field which tries to restore the zero charge density field $J = \sigma \cdot E$. In conductors (such as liquid metals) the response time of the Electric field is almost instantaneous and therefore the system can be considered as a quasi-static equilibrium. It is interesting to note that since localized charges cannot exist, current density line has to be close $\nabla \cdot J = 0$. This means electrons move continuously on closed trajectory lines without depositing on any specific spots.

In order to guarantee the divergence of the current density, an electric potential field has to be created because the velocity gradient is not generally irrotational, Eq. (7.3).

$$J = \sigma\left(-\nabla\phi + u \times B\right)$$
(7.1)

$$\nabla \cdot J = \sigma\left(-\nabla^2\phi + \nabla \cdot \left(u \times B\right)\right) = \sigma\left(-\nabla^2\phi + B \cdot \nabla \times u - u \cdot \nabla \times B\right) = 0$$
(7.2)

$$\nabla^2\phi = B \cdot \nabla \times u$$
(7.3)

Figure 38 shows the total current density field produced in stationary condition. On the y-z plane (x=0) J is almost only present above and below the bubble and the y component is the predominant. On the x-z plane (y=0) 4 regions with high J are present and the J_y is the domain component. On the top and on the bottom of the bubble the J_y is in-coming while on the sides, J_y in out-coming. On Figure 39, a 3D schematic representation of the current density line is shown.
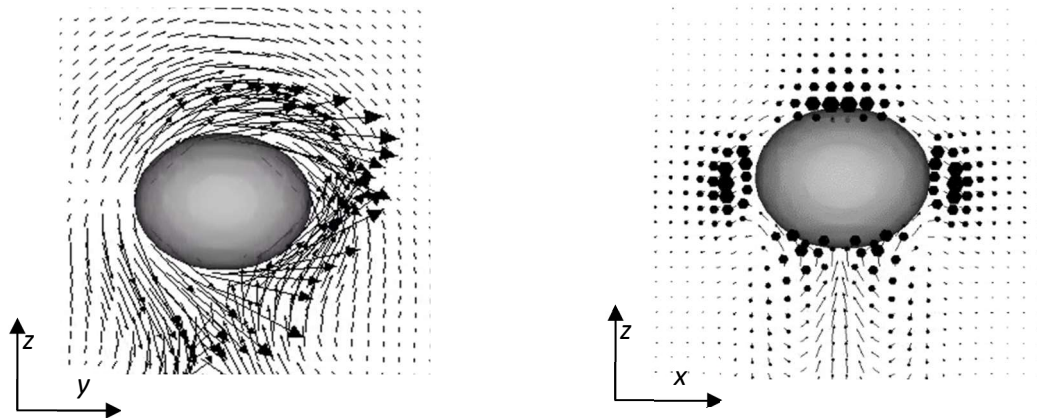

Figure 38 "Left: y-z section of current density J. Right: x-z section of J, D= 1.2mm."
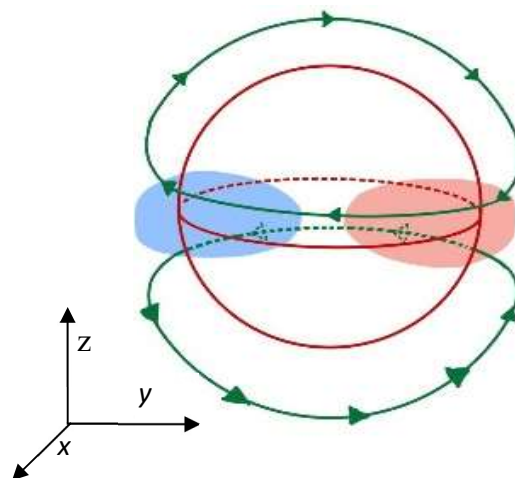

Figure 39 "3D qualitative representation of J lines."

A potential dipole is created inside the bubble during the raise-up and it remains constant when bubble reaches his terminal velocity (Figure 40). Since the bubble is an insulator, this electric potential does not create any currents inside the bubble but it produces a current in the surrounding liquid metal.
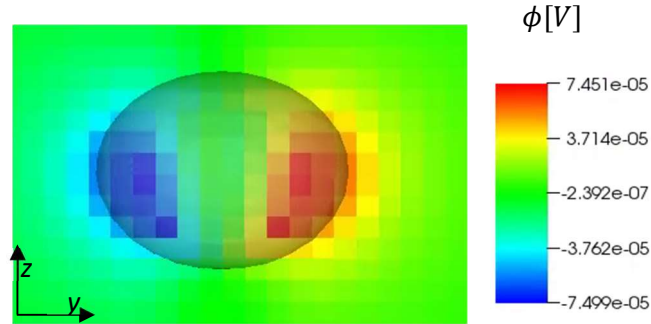
$$\phi[V]$$

Figure 40 "y-z section of the electric potential φ (D= 1.2 mm)."

From definition, the current density is the sum of two components, Eq. (7.4). The First is dependent on the Laplacian of the electrical potential Eq. (7.5) while the second is dependent on the liquid velocity field Eq. (7.6).

$$J = J_{potential} + J_{lorentz} \qquad (7.4)$$

$$J_{pot.} = -\sigma \cdot \nabla^2 \phi \qquad (7.5)$$

$$J_{lorentz} = \sigma\left(u \times B\right) \qquad (7.6)$$

The potential dependent part (Figure 41) goes from the positive to the negative pole. Its magnitude is high on the side of the bubble since $\nabla^2 \phi$ is high and it is really low on the top and the bottom of the bubble since the electric field E is almost zero. Electrical field and current density lines are the same of an electric dipole. (NB. Even if the electric field is really high inside the bubble, J is kept zero because Nitrogen is an insulant).
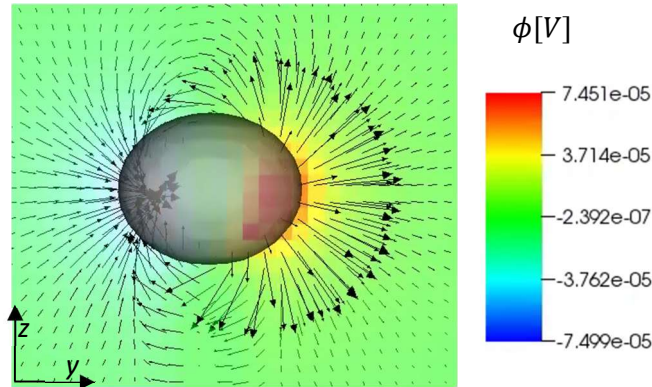
Figure 41 "y-z section of the electric potential φ and the J.pot (D= 1.2 mm)."

The Lorentz component is shown in Figure 42. It is every time perpendicular to the velocity field. It has its maximum on the top and bottom of the bubble since the velocity field is high and perpendicular to the external magnetic field. In the sides it is less relevant because the recirculation velocity is much slower and u and B are not always perpendicular to each other.
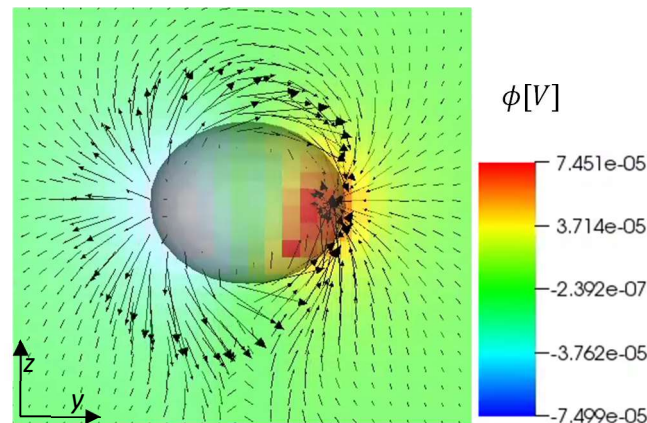

Figure 42 "y-z section of the electric potential φ and J.lorentz (D= 1.2 mm)."

7.1.3

7.1.4 Lorentz Force field distribution

Because of the simultaneous presence of an external constant magnetic field B and an inductive current J, the liquid will experiment a specific magnetic force of $F = J \times B$ [N/m³].

From many simulations it has been observed that $J_{lorenz} \gg J_{pot}$ on the top and bottom of the bubble $J = \sigma(-\nabla\phi + u \times B) \simeq \sigma(u \times B)$. Therefore, $F \simeq J \times B = u \times B \times B$. It can be shown mathematically that Lorentz force and velocity field has the same streamline but opposite direction. Therefore, Lorentz force is opposed to the liquid velocity and try to damp the recirculation movement on the top and bottom of the bubble. Physically the Lorentz force alters the pressure field across the

bubble, increasing the pressure on the top and decreasing it on the bottom. This will reduce the bubble top-bottom pressure difference which is the driving factor in the bubble raise up.

On the contrary, in sides of the bubble $J_{pot} \gg J_{lorenz}$ ($J = \sigma(-\nabla\phi + u \times B) \simeq -\sigma\nabla\phi$). In this region, the magnetic force is pushing up the surrounding liquid with the effect of reducing the velocity on the sides of bubble. As it can be seen in Figure 43, the Lorentz force is present only on the x borders of the bubble and not on the y borders. This happens because on x bubble borders, $J \perp B$ while in y borders $J \parallel B$. Therefore, the damp of the side recirculation does not take place on the y borders of the bubble.
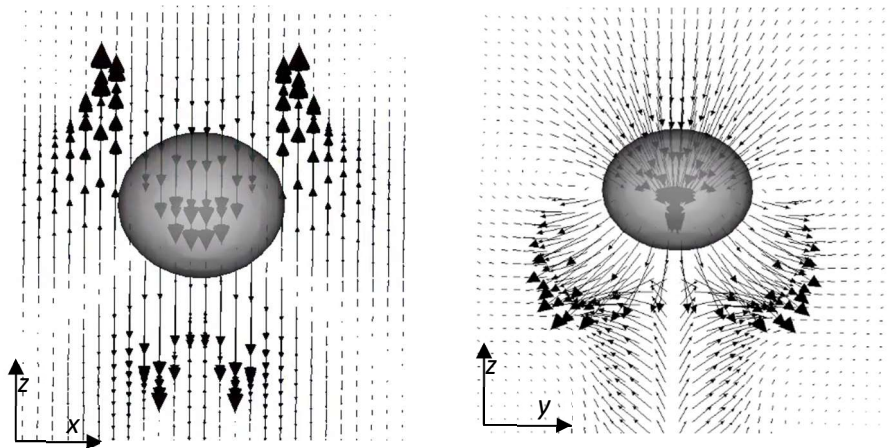

Figure 43 "Left: x-z plane of Lorentz force field. Right: y-z plane of Lorentz force field (D= 1.2 mm)."

On overall, the magnetic force tries to slowdown the recirculation processes which takes place around the bubble with the final effect of reducing the bubble rising velocity.

7.2   Force balance and governing parameters

To fully understand which are the driving dimensionless numbers $\left(\Pi_1, \Pi_2 ...\right)$ which characterize the bubble rising problem, the forces acting on the bubble have to be analyzed.

On stationary condition, a balance between volume and superficial forces is reached in the bubble. By Navier-Stokes equation, the pressure difference between two points is the sum of a kinematic, gravitational, viscous and magnetic term in stationary conditions Eq. (7.7).

$$\Delta p_{AB} = \frac{1}{2} \rho \cdot \left(u_B^2 - u_A^2\right) + \rho g \Delta h_{AB} + \mu \int_A^B \nabla^2 u \cdot dr + \int_A^B \left(J \times B\right) \cdot dr \qquad (7.7)$$

Same general considerations of the "bubble rising in liquid metal without magnetic field" can be done for the MHD case.

- In the upper part of the bubble, non-viscous approximation is still used (Figure 44) and the total pressure is the sum of the kinematic and magnetic pressure. Both components produce an overpressure which compress the bubble $\left(p_{kinematic} > 0, p_{magnetic} > 0\right)$.

- Below the detachment point, the fluid is viscous and the total pressure is the sum of a kinematic, viscous and magnetic component. Kinematic pressure is positive and leads to a compression while magnetic and viscous pressure are negative $\left(p_{kinematic} > 0, p_{magnetic} < 0, p_{visocus} < 0\right)$. Total dissipation can be assumed on the bottom of the bubble and the total pressure $p_{TOT} - p_{static}$ is kept zero as the B0 case. All the kinematic energy of the liquid is dissipated by the magnetic and viscous forces. Therefore, no energy is transferred into pressure on the bottom of the bubble. Once magnetic field increases, the bubble velocity is decreased. Figure 45 shows that kinematic pressure $\left(p_{kinematic} \propto \frac{1}{2} \rho u^2\right)$ and viscous pressure $\left(p_{visocus} \propto \mu \frac{u}{D^2}\right)$ decrease while the magnetic pressure increases $\left(p_{magnetic} \propto \sigma \cdot u \cdot B^2\right)$ with the magnetic field. Therefore, for small magnetic field viscous forces play a determining role and it dissipates all the kinematic energy alone. For enough big magnetic field the viscous forces becomes negligible also on the bottom of the bubble because all the kinetic energy is dissipated by the magnetic forces.
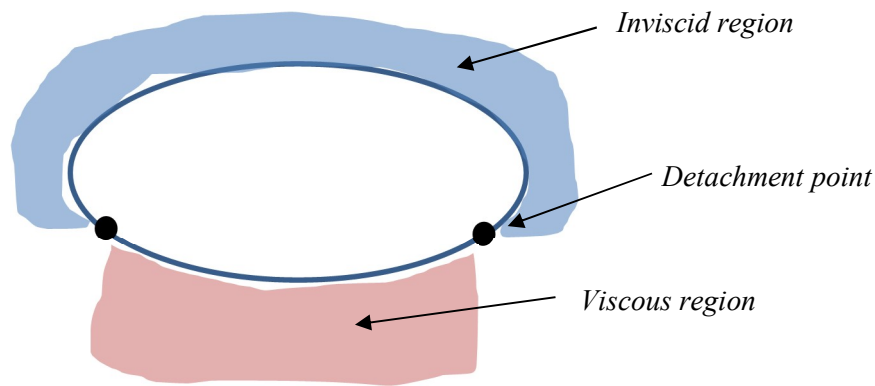
Figure 44 "Viscous & Inviscid regions around bubble. "
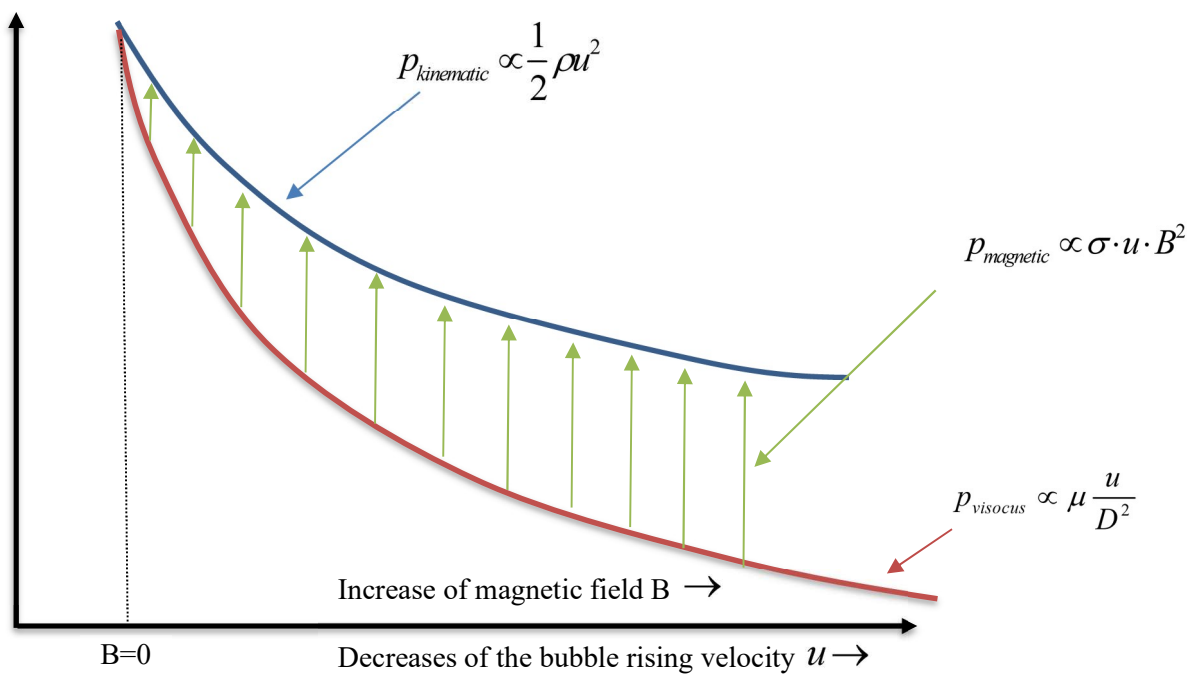
Figure 45 "Average kinematic, viscous and magnetic pressure on the bottom of the bubble for different magnetic field. "

Simulation results (Figure 46) agree with the total dissipation assumption made for the bottom of the bubble. Figure 46 shows that the pressure on the bottom of the bubble is much weaker than the pressure on the top and has no relevant impact on the drag force. Therefore, considering the bottom pressure equal to zero is a reasonable assumption and does not influence the bubble dynamics.

Figure 46 " P.tot-P.static field of a nitrogen bubble in mercury (D=3.86mm, B=1T)."

The gravitational pressure is computed apart in the buoyancy force and it does not influence the drag. Due to the high efficient recirculation process which happens inside the bubble, the shear stress field around the bubble is negligible and the 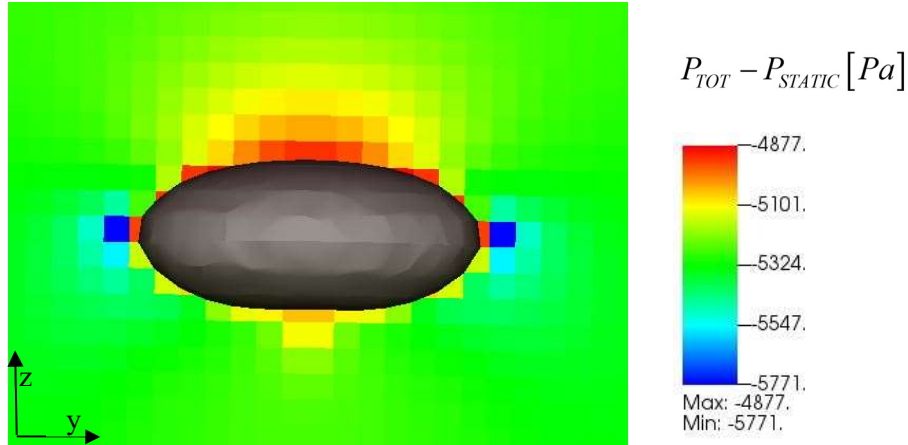drag force is computed considering only the pressure across the bubble, Eq. (7.8). The drag is computed considering only the kinematic and magnetic pressure on the top of the bubble where inviscid approximation is reasonable.

$$F_{DRAG} = \oiint (p_{tot} - p_{static}) \cdot \vec{dA} + \oiint \tau_{//} \cdot \vec{dA} \simeq \oiint (p_{tot} - p_{static}) \cdot \vec{dA} \qquad (7.8)$$

The final equation describing the bubble raise is (7.9)

$$\Delta \rho \cdot \frac{\pi D^3}{6} \cdot g = \oiint (p_{kinematic}) \cdot \vec{dA} + \oiint (p_{magnetic}) \cdot \vec{dA} \qquad (7.9)$$

The kinematic pressure is an overpressure due to the slowdown of the fluid and along the bubble surface it is $\frac{1}{2}\rho(u_\infty^2 - u^2(s))$. The liquid velocity on the bubble surface has only the component tangential $u_{//}$ to the surface while the normal component u_n is zero in order to conserve the flowrate $(\nabla \cdot u = 0)$. Local velocity on the surface is reasonably assumed to be proportional to the rising bubble velocity. $u^*\left(\vec{s}\right)$ is a unknown function which represents the dependency of the velocity on the local position, Eq. (7.10) .

$$u(s) = u^*(s) \cdot u_\infty \qquad (7.10)$$

The magnetic pressure is an over pressure due to the presence of the magnetic field. By the definition, a pressure change between two points is equal to the linear integral of $J \times B$ between the two points.

Far away from the bubble the magnetic pressure is set to zero $p_{magnetic}(r = \infty) = 0$, therefore the pressure drop correspond to the local pressure $\Delta p(s) = p(s) - p(\infty) = p(s)$ (Figure 47).

Since the current density $J = \sigma(-\nabla\phi + u \times B)$, the magnetic pressure can be expressed as a function of the electric potential, velocity and magnetic field, Eq.(7.11).

$$p(s) = \int_{\infty}^{s} J \times B \cdot ds = \int_{\infty}^{s} \sigma(-\nabla\varphi + u \times B) \times B \cdot dr = -\sigma \int_{\infty}^{s} \nabla\varphi \times B \cdot dr + \sigma \int_{\infty}^{s} u \times B \times B \cdot dr \qquad (7.11)$$

For each point of the surface, a linear integral along the liquid streamline has to be done, in order to compute the magnetic pressure.
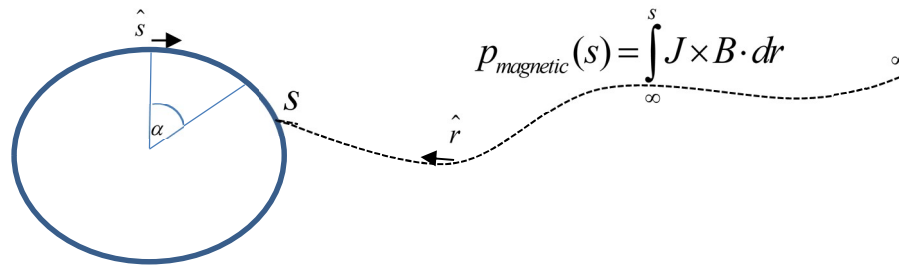
Figure 47 "Magnetic pressure definition."

Our interest it to calculate only the vertical component of the $\oiint (p_{magnetic}) \cdot \vec{dA}$ since we are interested only in the drag force. On each point of the bubble the pressure p produce a force $\vec{dF} = p \cdot \vec{dA}$ which is perpendicular to the surface. The drag force is only dependent on $\vec{dF_z} = \vec{dF} \cdot \sin(\alpha) = p \cdot dA \cdot \sin(\alpha)$. It clearly visible that pressure on the top and on the bottom of the bubble has a greater contribute then the pressure on the side whose vertical component is almost zero. Magnetic pressure on the sides of the bubble is almost irrelevant for the drag.

On the top and the bottom of the bubble the electrical potential field is almost constant $(J_{pot.} = -\sigma \cdot \nabla\varphi \simeq 0)$ and the $J \simeq J_{lorentz} = \sigma \cdot u \times B$ (Figure 48).

Figure 48 "y-z section of the electric potential φ (D= 1.2 mm)."
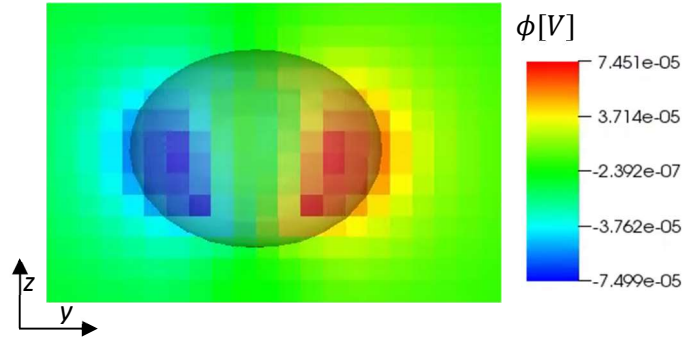
Magnetic pressure can be simplified as Eq. (7.12) :

$$p(s) = +\sigma \int_{\infty}^{s} u \times B \times B \cdot dr \tag{7.12}$$

The final vertical momentum balance equation is expressed in Eq. (7.13).

$$\Delta\rho \cdot \frac{\pi D^3}{6} \cdot g = \oiint \frac{\rho}{2}\left(u_\infty^2 - u^2(s)\right) \cdot \vec{dA} + \oiint \left(\sigma \int_{\infty}^{s} u \times B \times B \cdot dr\right) \cdot \vec{dA} \tag{7.13}$$

The velocity, the surface vector and the magnetic field are resized : $u^* = \dfrac{u(s)}{u_\infty}$, $r^* = \dfrac{r}{D}$, $\hat{i} = \dfrac{\vec{B}}{B}$

$$\Delta\rho \cdot \frac{\pi D^3}{6} \cdot g = \frac{\rho \cdot u_\infty^2}{2} \oiint \left(1 - u^{*2}(s)\right) \cdot \vec{dA} + \oiint \left(\sigma u_\infty B^2 D \cdot \int_{\infty}^{s} u^* \times \hat{i} \times \hat{i} \cdot dr^*\right) \cdot \vec{dA} \tag{7.14}$$

$$\Delta\rho \cdot \frac{\pi D^3}{6} \cdot g = \frac{\rho \cdot u_\infty^2}{2} \oiint \left(1 - u^{*2}(s)\right) \cdot \vec{dA} + \sigma u_\infty B^2 D \cdot \oiint \left(\int_{\infty}^{s} u^* \times \hat{i} \times \hat{i} \cdot dr^*\right) \cdot \vec{dA} \tag{7.15}$$

$$\Delta\rho \cdot \frac{\pi D^3}{6} \cdot g = \frac{\rho \cdot u_\infty^2}{2} \cdot \overline{\left(1 - u^{*2}(s)\right)} \cdot \pi D^2 + \sigma u_\infty B^2 D \cdot \overline{\left(\int_{\infty}^{s} u^* \times \hat{i} \times \hat{i} \cdot dr^*\right)} \cdot \pi D^2 \tag{7.16}$$

$\overline{\left(1 - u^{*2}(s)\right)}$ and $\overline{\left(\int_{\infty}^{s} u^* \times \hat{i} \times \hat{i} \cdot dr^*\right)}$ are the surface average of the respective functions. Both of them can be considered dependent only on the shape of the bubble. Since the bubble has an ellipsoidal shape, they are functions of the aspect ratio X only. Clearly, these functions are not known at priori. Furthermore, it has been observed by simulations that in MHD case the aspect ratio X still remains a

function of the Weber number only (Chap. 8). This means that these two surface average functions are dependent on the Weber number of the bubble only, Eq. (7.17) and Eq. (7.18).

$$\overline{\left(1-u*^2(s)\right)} = \frac{\oiint\left(1-u*^2(s)\right)\cdot dA}{\pi D^2} = f(X) = f(X(We)) = f(We) \tag{7.17}$$

$$\overline{\left(\int_\infty^s u*\times\hat{i}\times\hat{i}\cdot dr*\right)} = \frac{\oiint\left(\int_\infty^s u*\times\hat{i}\times\hat{i}\cdot dr*\right)\cdot dA}{\pi D^2} = g(X) = g(X(We)) = g(We) \tag{7.18}$$

By re-arranging the terms, it is found out:

$$\Delta\rho\cdot\frac{\pi D^3}{6}\cdot g = \frac{\rho\cdot u_\infty^2}{2}\cdot f(We)\cdot\pi D^2 + \sigma u_\infty B^2 D\cdot g(We)\cdot\pi D^2 \tag{7.19}$$

$$\Delta\rho D^2 g = 3\rho u_\infty^2 D\cdot f(We)\cdot +6\sigma u_\infty B^2 D^2\cdot g(We) \tag{7.20}$$

$$\frac{\Delta\rho D^2 g}{\gamma} = 3\frac{\rho u_\infty^2 D}{\gamma}\cdot f(We)\cdot +6\frac{\sigma u_\infty B^2 D^2}{\gamma}\cdot g(We) \tag{7.21}$$

$$Eo = 3We\cdot f(We)\cdot +6\frac{\sigma u_\infty B^2 D^2}{\gamma}\cdot g(We) \tag{7.22}$$

$K = \dfrac{\sigma u_\infty B^2 D^2}{\gamma}$ is a new dimensionless number which influences the bubble rising problem. It represents the ratio between inertia and magnetic forces to the surface tension forces. It can be obtained from Reynolds, Eotvos and Weber numbers Eq. (7.23):

$$K = \frac{We\cdot Ha^2}{Re} \tag{7.23}$$

Finally, the dimensionless numbers which described the system are: We, Eo and K.

Since there numbers are coupled, the system is characterized by one couple, Eq. (7.24).

$$F(We, Eo, K) = 0 \tag{7.24}$$

It is interesting to see that the total drag force is the sum of a kinematic pressure component and a magnetic pressure component. Both parts increases the drag force and decreases the bubble velocity.

The relative importance of the magnetic field is found by the relative comparison between the magnetic $We = \dfrac{\rho \cdot D \cdot u^2}{\gamma}$ and kinematic parameter $K = \dfrac{\sigma u_\infty B^2 D^2}{\gamma}$. The ratio between the two parameters leads to the Stuart number N which is the most representative value. Stuart number represents the relative important of the magnetic forces compared to the inertia forces for the bubbly vertical dynamics, Eq. (7.25).

$$\frac{K}{We} = \frac{\dfrac{\sigma \cdot u_\infty \cdot B^2 \cdot D^2}{\gamma}}{\dfrac{\rho \cdot D \cdot u_\infty^{\ 2}}{\gamma}} = \frac{\sigma \cdot B^2 \cdot D}{\rho \cdot u_\infty} = N = \frac{Ha^2}{\mathrm{Re}}$$

$$(7.25)$$

7.3   Terminal rising velocity under magnetic field

Bubbles in liquid metals have been simulated with PSI-BOIL and compared with Wang's experimental results [6]. Wang experimental results might be considered more reliable compare to Mori's one since the Ultrasound Doppler Velocimetry (UDV) technique used by Wang is generally more precise than the Electrical Triple Probe (ETP) used in 1977 by Mori [5].

Many different bubbles (*Eo* = 1.12, 1.35, 2.44, 3.67, 3.1, 4.48) have been simulated with different applied magnetic fields in order to compare PSI-BOIL results with experimental one.

From the results it has been shown that for little bubbles (*Eo* < 1.6) the velocity is monotony decreasing with magnetic field (Figure 49). The major effect of the Lorentz force applied to the bubble is the reduction of recirculation of the liquid across the bubble. In this case, the bubble trajectory is straight even without the external magnetic field, therefore the trajectory straightening caused by the magnetic field is clearly non present.

For enough big bubbles (*Eo* > 1.6), in absence of external magnetic field instabilities phenomena take place and the bubble raise-up is not anymore axisymmetric. Bubble oscillates in x and y direction and in shape (Figure 50). For those bubbles, the applied magnetic field produces two interesting phenomena. Lorentz force decreases recirculation inside the bubble and damp the bubble rising velocity, but simultaneously it straights the trajectory on the z direction. Those are two competitive events for the vertical rising velocity. The straightening of the trajectory is very B sensitive which means the trajectory is strongly straitened also with low magnetic field while the decreases of the recirculation is almost linear dependent with *B*. Velocity behavior for big bubbles is not monotonous. Velocity first increases because of the damp of instability, it reaches a maximum and then decreases because of the damp of the recirculation (Figure 49). The magnetic field at which maximum occurs and velocity itself increase if the initial instability of the trajectory is higher.

In conclusion we can declare that the not monotonous behavior of the velocity vs. *B* is possible only for bubbles which have non straight trajectory without magnetic field which is a condition achieved by only enough big bubbles (*Eo* > 1.6).
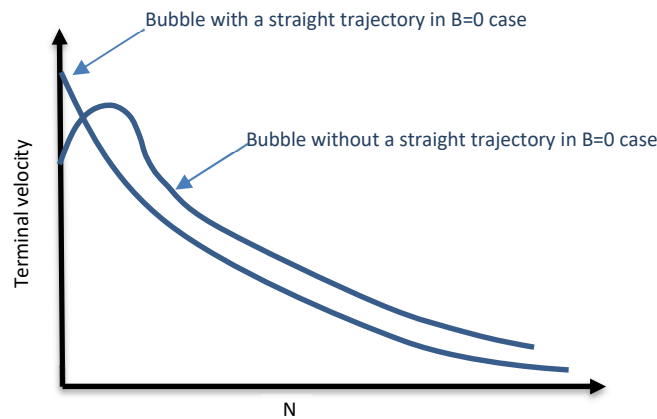
Figure 49 "Graphical illustration of Velocity vs. Stuart number for stable and unstable bubbles."
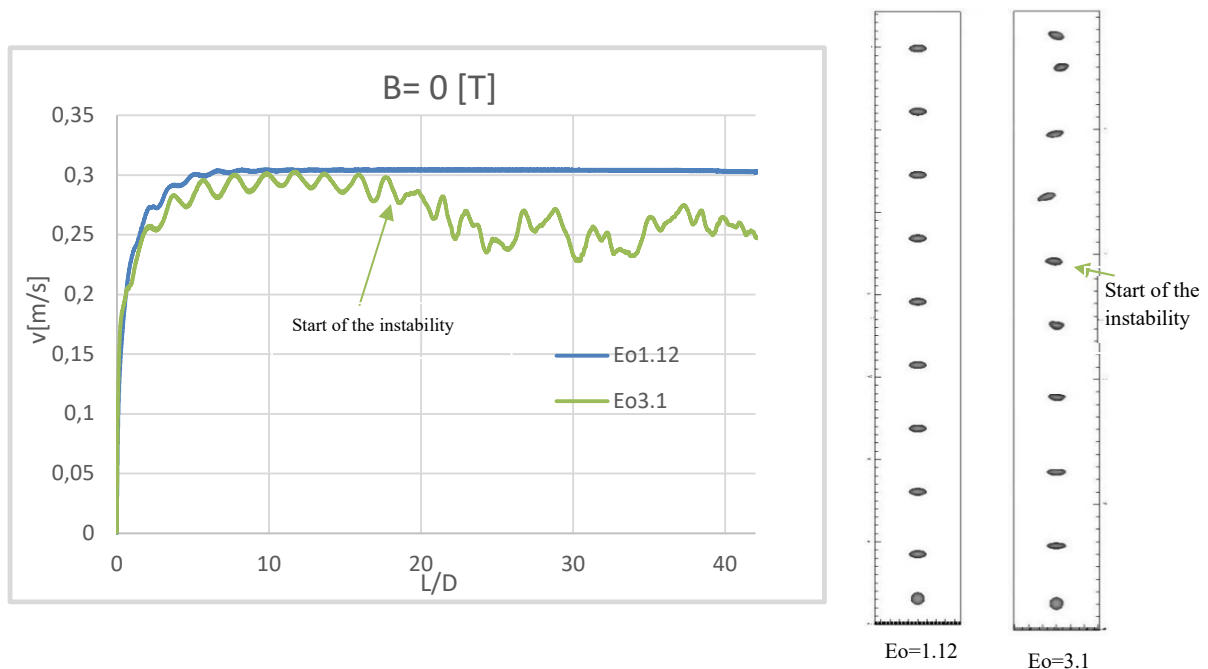

Figure 50 "Left: Velocity for Eo=1.12 and 3.1 bubbles without magnetic field. Right: x-z section of bubble trajectory (left : Eo= 1.12 right: Eo=3.1)."

Results of this simulation presents some differences with Wang experiments results. In Wang experiment, the non-monotonous behavior of the velocity versus the Stuart number N is clearly visible for all bubbles sizes while in PSI MHD only for big bubble (*Eo* > 1.6) (Figure 52). In Wang experiment, therefore also the little bubbles experience instability phenomena during the rise which curve the rising trajectory. This additional instability are caused by the non ideal initial condition of the Wang experiment in which the bubbles are produced by an inlet nozzle. When the bubble detaches, its initial velocity is not zero, the bubble shape is not spherical but it presents some little compression and the velocity field in the surrounding is not zero. These minor effects play a major role in the bubble evolution and lead to a non straight trajectory even for little bubbles.[17].
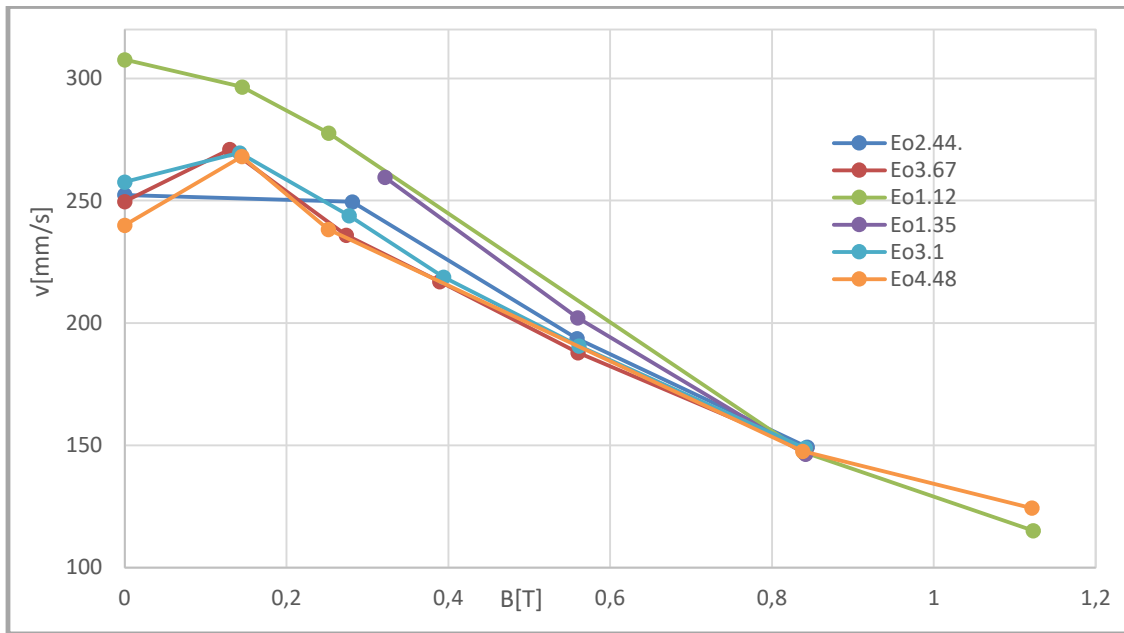
Figure 51 "Terminal velocity as a function of the transverse applied magnetic field for different bubble sizes (proprieties: Argon bubble in GaInSn)."

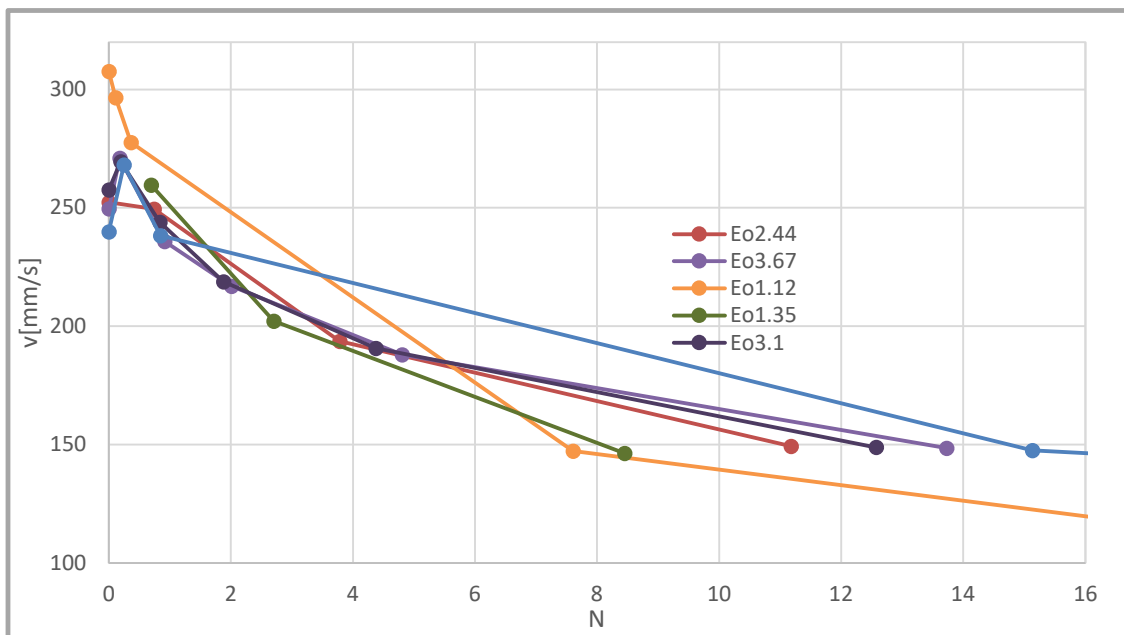*Figure 52 "Terminal velocity vs. Stuart Number for different bubbles sizes (Argon bubble in GaInSn)."*

Manage to characterize bubble velocity for little Stuart Number is quite challenging due to possible instability phenomena which might take place. Instead, for strong magnetic field ($N > 0.8$) it is clearly visible a monotonous decrease of the velocity with N for all bubbles.

All the velocities of the PSI-BOIL simulations are plotted in Figure 53 for different Stuart numbers (N>0.8) and compared to experiment results (Wang). It can be noticed that the trend of the simulation is coherent with experiments results. On average, although the CFD terminal rising velocity is higher than the experiment one for all *N*. The most creditable explanation is the fact that in real GaInSn there are many impurities which modify the liquid behavior and the liquid proprieties. Impurities are deposited on the liquid-gas interface, they decrease the recirculation process which takes place inside the bubble with a consequent increases of the drag force applied to the bubble. The experiment velocity tends so to be decreased.

Wang provide an experimental correlation (7.26) which can be considered a generalized Mendelson formula in the presence of strong magnetic field ($N > 0.8$).

$$\text{Wang correlation: } u_{TLM} = 0.932 \cdot \sqrt{\frac{2\gamma_l}{\rho_l D} + \frac{gD}{2}} \cdot N^{-0.254} \qquad (7.26)$$
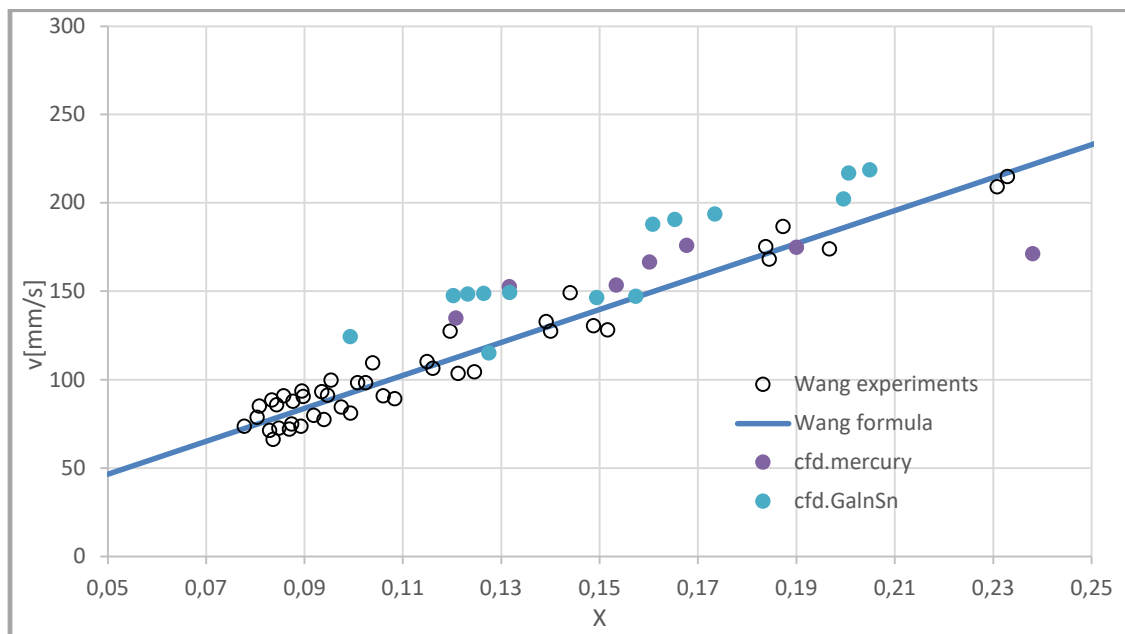
Figure 53 "Comparison between Wang experimental correlation and PSI-BOIL results."

In order to provide a CFD correlation for MHD of the rising bubble problem in "high purity liquid metal" an interpolation between PSI-BOIL results have been conducted. A multiple linear regression model using the Mendelson velocity formula and Stuart number allows us to find the 2 parameters A and B which characterize the correlation Eq. (7.27). Results from CFD simulations with mercury, liquid steel and GaInSn have been used in order to produce the correlation Eq. (7.28). The R^2 of the interpolation is 0.8151. Therefore there is a good agreement between results of simulations with different material propriety which is a proof of the universally efficiency of the PSI-BOIL correlation.

$$u_{TLM} = A \cdot \sqrt{\frac{2\gamma_l}{\rho_l D} + \frac{gD}{2}} \cdot N^{-B}$$

(7.27)

Figure 54 " Comparison between Wang correlation and PSI-Boil correlation."

PSI-Boil correlation: $u_{TLM} = 0.9267 \cdot \sqrt{\frac{2\gamma_l}{\rho_l D} + \frac{gD}{2}} \cdot N^{-0.176}$
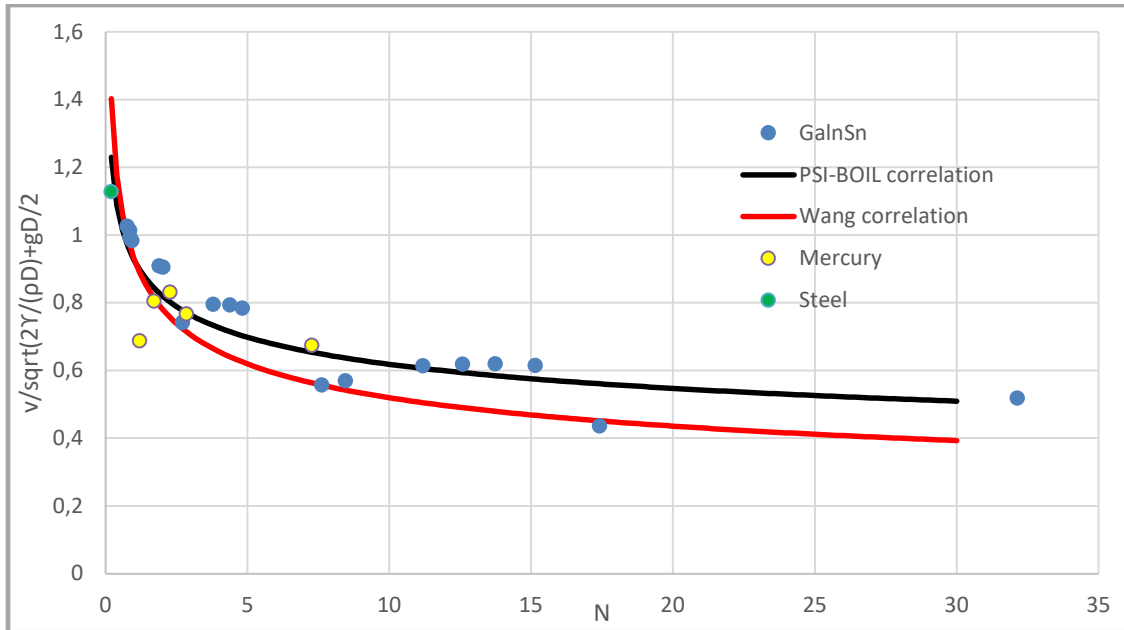
(7.28)

The similar tendency of the PSI correlation compared to the Wang can be considered as an experimental validation of the PSI-BOIL in the "bubble flow in liquid metal environment in presence of transverse magnetic field" (Figure 54). The discrepancy between the software and the experiments results are caused by impurities inside the liquid metal which are not modeled in the software.

7.4 Stability of bubble under magnetic field

Velocity oscillation are directly connected to bubble shape oscillation. When a bubble is compressed on z direction, the contact area with the liquid increases and so the drag force. The bubble starts to feel a strong deceleration which decreases its local velocity. On the contrary, a bubble elongated on the z direction assumes a hydrodynamic shape which decreases the drag Force and produce an acceleration which increases the local velocity. Bubble oscillations can be roughly expressed as harmonic oscillations when highest velocity is reached by the compressed shape and the lowest velocity is reached by the elongated shape.

During the rise, the bubble passes from a spherical shape to a final ellipsoidal shape. Bubble velocity increases and the pressure field on bubble surface is changed. As it known, bubble local curvature depends on the local kinematic pressure. Velocity field around the bubble produces a compressive pressure field on the top and bottom of the bubble and a tensile pressure field on the bubble side (Figure 56). The magnitude of the pressure field is proportional to u_∞^2. Macroscopically, the bubble is deformed by the kinematic pressure field.
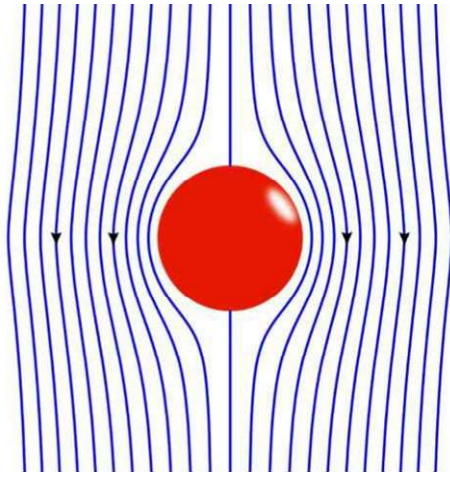

Figure 56 "Lagrangian velocity profile."
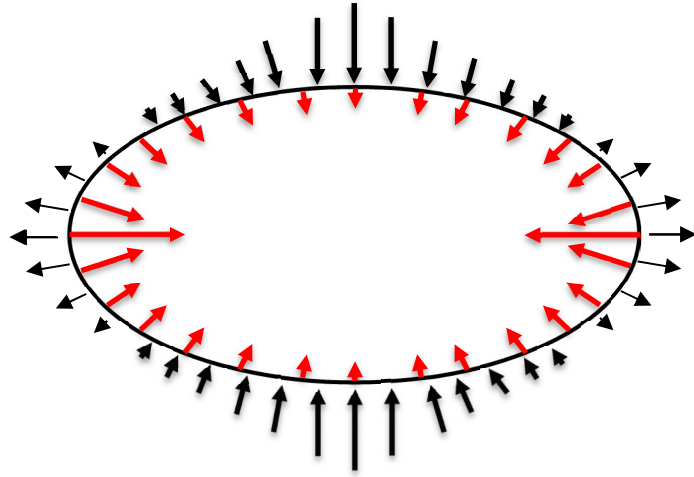
Figure 56 "Representation of surface tension (red) and kinematic pressure (black) forces acting on a rising bubble."

Bubble stability is studied at the terminal bubble velocity. For simplicity, curvature of the top of the bubble is studied (Figure 57). At equilibrium, the top curvature is fixed and controlled by only the kinematic overpressure (7.29). We want to studied how the local curvature is affected by an instantaneous variation of the rising velocity. $(du \rightarrow d\chi)$. A force balance on the top interface is made after the system has been perturbed, Eq. (7.30).

$$p_{in} = \rho g h + \frac{1}{2} \rho \cdot u_\infty^2 + \gamma \cdot \chi \qquad \text{at t=0} \tag{7.29}$$

$$p_{in}(t + dt) = \rho g h(t + dt) + \frac{1}{2} \rho \cdot u_\infty^2(t + dt) + \gamma \cdot \chi(t + dt) + \frac{dm}{dA} \cdot a \tag{7.30}$$

$$p_{in} = \rho g h + \frac{1}{2} \rho \cdot (u + du)^2 + \gamma \cdot (\chi + d\chi) + \frac{dm}{dA} \cdot a \tag{7.31}$$

$$p_{in} = \rho g h + \frac{1}{2} \rho \cdot (u + 2u \cdot du + du^2) + \gamma \cdot (\chi + d\chi) + \frac{dm}{dA} \cdot a \tag{7.32}$$

Using Eq. (7.29) which represents initial forces equilibrium, Eq. (7.32) is simplified in Eq. (7.33).

$$\rho u \cdot du + \gamma \cdot d\chi + \frac{dm}{dA} \cdot a = 0 \qquad (7.33)$$

dm stands for the local mass of fluid surrounding the interface, dA stands for the local interface area and a stand for the interface acceleration. dm scales with D^3 and dA with D^2. The term $\frac{dm}{dA}$, which can be considered the inertia of the system, scales with D. For small bubbles it is negligible and there is an instantaneous response of the local curvature to the bubble velocity variation. For these bubbles, instabilities are almost impossible because the system response time of the system tends to zero. For big bubble ($Eo > 1.5$), instead, $\frac{dm}{dA}$ is not negligible and produced a delay of the response. Once the $\frac{dm}{dA}$ becomes bigger, the response time of the system increases and the amplitude of the bubble oscillation increases. Physically an increase of the kinematic pressure cannot change immediately the bubble curvature because it has also to accelerate the surrounding liquid first, which is the inertia of the system. Therefore, big bubbles tend to be instable due to their inertia.
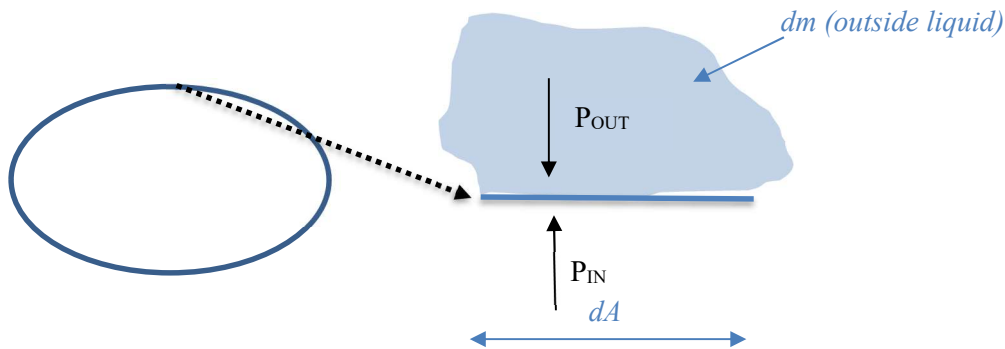
Figure 57 "Force balance on the top of the bubble."

Once an external magnetic field is applied, simulations show that bubble stability is increased (Figure 58).A possible explanation why magnetic field enhances bubble stability can be found analyzing the sensitivity of the curvature respect the bubble velocity. The major effect of the external magnetic field is the reduction of the terminal velocity. If the terminal velocity is reduced, the sensitivity of the curvature respect the velocity is reduced, Eq. (7.34). Therefore, for small velocities, the curvature is less sensitive respect the velocity and the system is more stable.

$$d\chi = -\frac{\rho}{\gamma} u_\infty \cdot du - \frac{1}{\gamma} \frac{dm}{dA} \cdot a \qquad (7.34)$$

Finally, the application of an external magnetic field manage to stabilize also big bubble because it significantly reduces the bubble rising velocity and make curvature less sensitive respect the bubble

velocity. Generally, bubbles instabilities in liquid metals regime happens at Eo=1.5 for a B=0 case. Nevertheless, the more strong is the applied magnetic field, the higher will be the transitional Eotvos from stable to unstable regime.

An other possible explanation of the enhancement of the stability caused by magnetic field can be found analyzing the vortex structure behind the bubble. Zhang [11] shows that also weak magnetic fields significantly reduce the vortex structure behind the bubble and promote trajectory and shape stability.
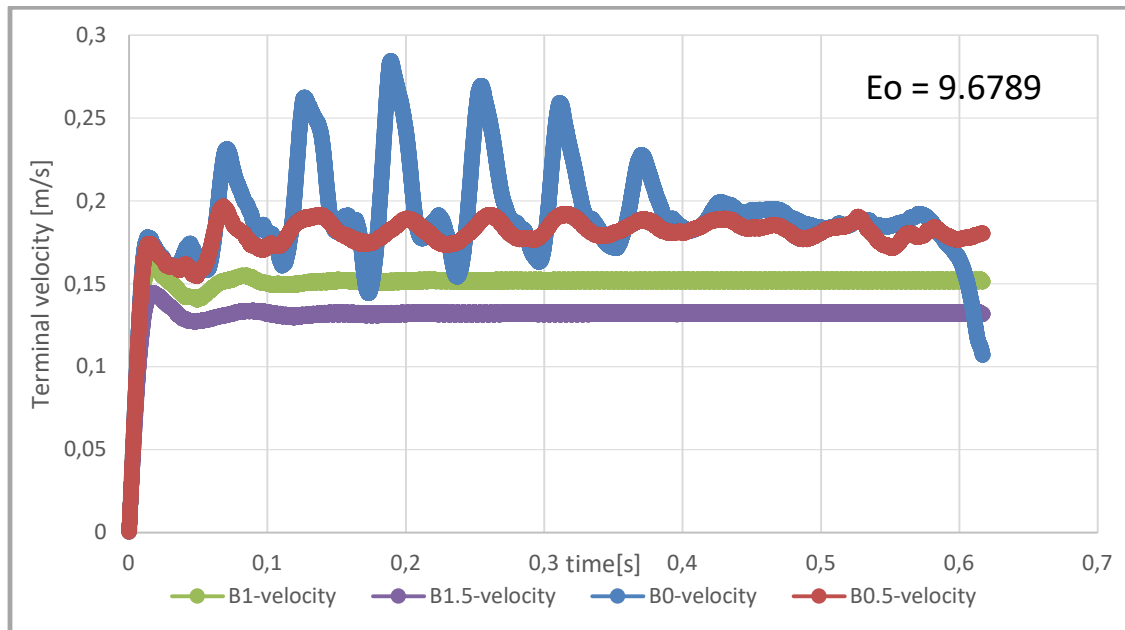
Figure 58 "Velocity vs time for different external magnetic field B."

7.4.1 Bubble trajectory

For the bubbles with enough high Eotvos number with the condition $B = 0$, the velocity flow field in not axisymmetric anymore because 3D dependence instability phenomena happen. Bubble trajectory is not straight anymore because small movements on the x-y plane take place. This is produced by the same instability processes which produce bubble shape oscillations.

By applying an external transverse magnetic field, the trajectory is becoming straight back because all instability phenomena are eliminated (Figure 59).
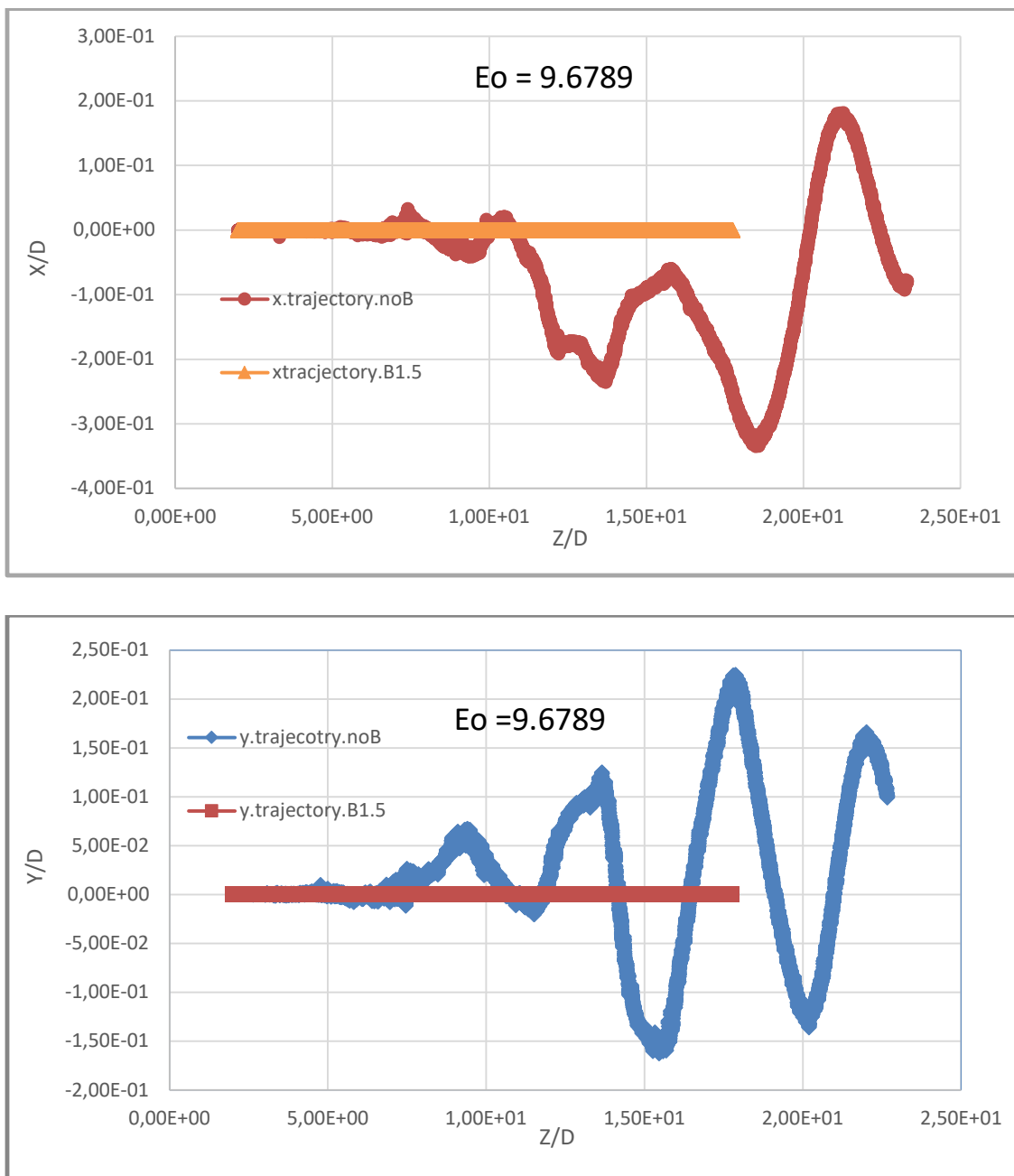
Figure 59 "Bubble trajectory with and without external magnetic field."

8   Bubble Shape with magnetic field

8.1 Simulation results

Simulations suggest external magnetic field influences bubble shape behavior. Bubble shape can be approximated as an ellipsoid $\left(\dfrac{x^2}{a^2} + \dfrac{y^2}{b^2} + \dfrac{z^2}{c^2} = 1 \right)$ $X_x = \dfrac{a}{c}$ and $X_y = \dfrac{b}{c}$ are defined as dimensionless parameters which characterize bubble compression.
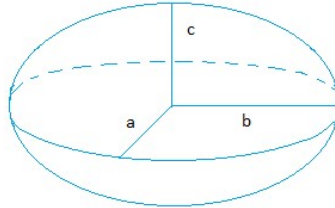
Figure 60 "Ellipsoidal representation of the bubble."

Simulations of nitrogen bubbles in liquid mercury have been conducted. In Figure 61 terminal bubble $X = \dfrac{X_x + X_y}{2}$ is plotted as the function of Eotvos number for different external magnetic fields.
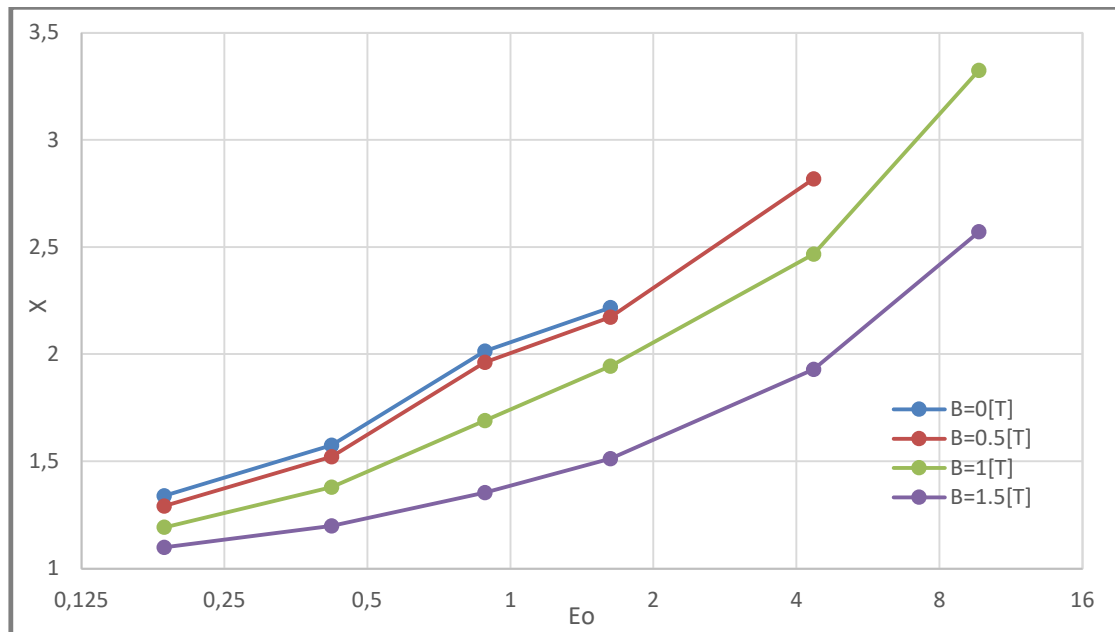
Figure 61 " X vs Eo for different external magnetic field."

For a fixed external magnetic field, *X* increases with *Eo*. The final bubble shape is produced by a balance between buoyancy forces proportional to D^3 and superficial forces proportional to D^2. It has been previously established [chap. 5] that for liquid metals the Weber number monotonously increases with Eotvos and that the shape factor *X* increases with Weber number [chap. 6]. Therefore, a positive trend of *X* vs. *Eo* is clear.

 For weak or zero external magnetic field, the $X(Eo)$ does not have a clear trend. This is mainly because of instability phenomena which cause for Eo>1.5 bubble's oscillation in shape and in velocity. For high B problem, the rising velocity is remarkably reduced, the drag force is less predominant and therefore the bubble is less stretched (X is reduced).If the applied magnetic field is large enough ($B > 1$ T), a parabolic trend ($X \simeq Log(Eo)^2$)can be observed. This clear trend is possible due to the lack of instability phenomena which are dampened by the B_{ext}.

For little bubbles (Figure 62), surface tension forces are predominant and the shape is almost a sphere. In this case, the bubble shape is weakly dependent on B_{ext}. Littles bubbles have a low Weber number, due to their little diameter, which causes the X to be almost 1. For those bubble the linear Shape theory is applicable $\left(X = 1 + \dfrac{9}{64} \cdot We \right)$ and suggests that in this region the shape factor weakly depends on the Weber number. Once the magnetic field is applied, the velocity of the bubble is significantly reduced and so the Weber number. Since there is a weak dependency of X on We, X is not strongly affected by the external magnetic field.

For big bubbles (Figure 62), instead, the linear shape theory is not applicable anymore and the Shape factor is becoming more dependent on We. For these bubbles, the external magnetic field reduced the terminal Weber and decreases more significantly the shape factor.
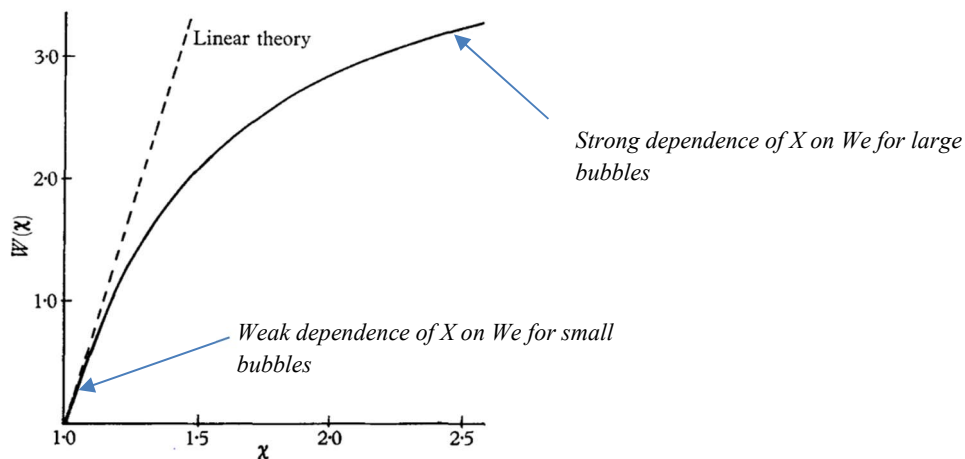
Figure 62 "Bubble aspect ratio vs. Weber."

External magnetic field decreases the terminal Weber number and so the shape factor X. It seams that the shape factor X is almost only dependent on the Weber number also under the presence of external magnetic field (Figure 63) because all the lines in Figure 63 are converging, especially for little bubbles. Therefore, the bubble shape theory for bubble in liquid metal without external magnetic field $X = (We)$ can be used also for the bubble rising problem under external transverse magnetic field. The external

magnetic field produces a Lorentz force field acting on the liquid surrounding the bubble. The main effect of the Lorentz force is the reduction of the recirculation which decreases the rising bubble velocity and Weber number. It seems, as first approximation, that the shape factor is still controlled by only the Weber number also under the presence of external magnetic field. Figure 63 suggests that this approximation is valid for most of the points
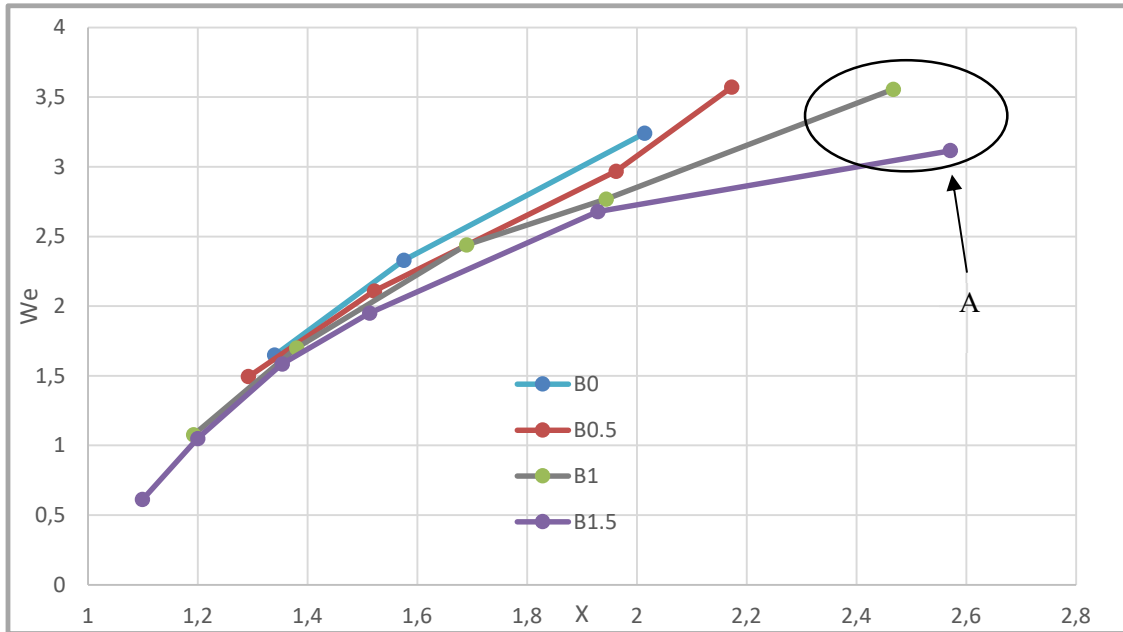
Figure 63 "We vs. X for different applied magnetic fields."

Nevertheless, bubbles with big diameters under strong magnetic field seem to behave differently (A). In order to understand why these bubbles behave differently, an analytical approach has be used. In the next section an analytical MHD bubble shape theory is established by basic principles with the purpose to explain big seizes bubbles behavior under strong magnetic field.

8.2   New analytical solution for bubble aspect ratio under magnetic field

8.2.1   Force balance and curvature definition

In order to compute the bubble aspect ratio X, the bubble curvature $\chi(s)$ has to be known. The bubble curvature is found in each point of the bubble surface by a force balance between inner and outer pressure forces $p_{in} = p_{out}$. The analytical solution for the bubble aspect ratio in the magnetic field is almost equal to the one without the magnetic field, but a new pressure term has to be taken into account in the outer-pressure. This term is the magnetic pressure:

$$p_{magnetic} = \int_{\infty}^{s} J \times B \cdot dr .$$

(8.1)

The viscous pressure $\mu \int_{\infty}^{s} \nabla^2 u \cdot dr$ is, as usual, negligible since the problem can be considered inviscid.

It has been previously established in the B0 case that inner pressure and gravitational pressure do not affect the bubble curvature since their difference is constant during the rise. Same consideration can be done for MHD case and therefore the kinematic and the magnetic pressure are the only components which influence the local bubble curvature, Eq. (8.5).

$$p_{out} = \rho g h + \frac{1}{2} \rho \cdot \left(u_{\infty}^2 - u^2(s) \right) + \gamma \cdot \chi(s) + \int_{\infty}^{s} J \times B \cdot dr$$

(8.2)

$$p_{in} = p_{out}$$

(8.3)

$$p_{in} = \rho g h + \frac{1}{2} \rho \cdot \left(u_{\infty}^2 - u^2(s) \right) + \gamma \cdot \chi(s) + \int_{\infty}^{s} J \times B \cdot dr$$

(8.4)

$$\chi(s) = \frac{ + \frac{1}{2} \rho \left(u^2(s) - u_{\infty}^2 \right) + \rho g h - p_{in} - \int_{\infty}^{s} J \times B \cdot dr }{ \gamma }$$

(8.5)

By studying the pressure balance on bubble interface at first instant where it is perfectly spherical, it can be found $p_{in} - \rho g h = \gamma \chi_o = \dfrac{4\gamma}{D}$. Therefore, the curvature equation can be re-arranged as Eq. (8.6)

..

$$\chi(s) = \frac{\chi_0 + \frac{1}{2}\rho\left(u^2(s) - u_\infty^2\right) - \int_\infty^s J \times B \cdot dr}{\gamma} \tag{8.6}$$

In order to find the bubble aspect ratio, a procedure analog to the B=0 case is carried out. The curvature on the top and on the sides of the bubble is proceed and compared to ellipsoidal curvature in order to find out the aspect ratio X. Nevertheless, there are some physical differences which have to be taken into account.

The flow field around the bubble $\vec{u}(s)$ and the Lorentz force $F = J \times B$ are not axisymmetric field. This means that the compression on the x and y plane are different and they will lead to different aspect ratios $\left(X_x \neq X_y\right)$. From simulations it has been seen a higher compression on the y plane (perpendicular to the magnetic field) $X_y > X_x$. The reason why the two aspect ratios are different is because the bubble curvature on the x side of the bubble and the curvature on the y side of the bubble are different $\left(\chi_X(\theta = 90) \neq \chi_Y(\theta = 90)\right)$. To compute the average aspect ratio $\overline{X}$, it should be used the arithmetic average between the bending radii a and b, Eq. (8.7).

$$\overline{X} = \frac{X_y + X_x}{2} = \frac{\frac{b}{c} + \frac{a}{c}}{2} = \frac{\frac{b+a}{2}}{c} \tag{8.7}$$

Simulations shows X_x and X_y have a relative difference than less than 5% for all bubble sizes, therefore averaging on the curvature and averaging on the radii leads to similar results. For simplicity, in this analysis the side curvature χ_{SIDE} is computed as the arithmetic average between the curvature on x and y side, Eq. (8.8).

$$\chi_{SIDE} = \frac{\chi_X(\theta = 90^o) + \chi_y(\theta = 90^o)}{2} \tag{8.8}$$

Once χ_{TOP} and χ_{SIDE} are computed, the bubble is considered to be axisymmetric in order to find the bubble average aspect ratio $\overline{X}$.

Procedure followed:

1. Compute curvature on the top of the bubble χ_{TOP}
2. Compute curvature on the x-side of the bubble χ_{SIDE}
3. Compute curvature on the y-side of the bubble χ_{SIDE}
4. Compute side curvature by averaging x and y side curvature
5. Consider an equivalent axisymmetric bubble with the same top χ_{TOP} and side curvature χ_{SIDE}
6. Compute bubble aspect ratio $\overline{X}$ of the equivalent axisymmetric bubble

$$\chi_{max} = \frac{1}{R_s} + \frac{1}{R_t} = \frac{a}{c^2} + \frac{1}{a} = \frac{\left(\frac{a}{c}\right)^2 + 1}{a} = \frac{X^2 + 1}{a}$$

$$\chi_{min} = \frac{1}{R_s} + \frac{1}{R_t} = \frac{c}{a^2} + \frac{c}{a^2} = \frac{2}{a} \cdot \frac{c}{a} = \frac{2}{a \cdot X}$$
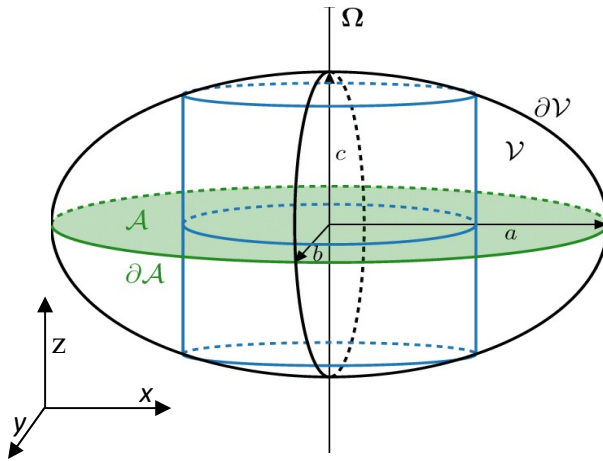
$$\frac{\chi_{min}}{\chi_{max}} = \frac{\left(\frac{2}{a \cdot X}\right)}{\left(\frac{X^2 + 1}{a}\right)} = \frac{2}{X \cdot \left(X^2 + 1\right)}$$

Figure 64 "Elliptic representation of the bubble."

8.2.2 Side velocity field

In this analysis the bubble reference system is considered and a Lagrangian velocity is studied. On the side of the bubble, the liquid velocity is increased because it experimented a convective acceleration due to the restriction of the flow section. In fact, on the bubble's side a tunneling effect happens. By a macroscopic flow conservation around the bubble, it can be established that the average velocity $\overline{u\left(90^o\right)}$ on the bubble side depends only on the bubble rising velocity u_∞ and on the geometry of the system. Therefore, it is not influenced directly by the magnetic field presence. Nevertheless, as told before, the flow field is not axisymmetric and the local side velocity in each point in not equal to the average one. Simulations suggest that the velocity on the y-side is slightly higher compared to the velocity on the x-side. On the x-side of the bubble the magnetic force $F = J \times B$ produces an additional

delta pressure which make the path difficult to follow by the liquid. On the y-sides of the bubble the magnetic force increases the pressure drop and makes the path more easy for the liquid. The liquid flowrate which passes around the bubble is the same of a *B = 0* case but the liquid experiment a higher resistance on the x-sides compare to the y-side. Logically there is more liquid passing on the y-side compared to the x-side.

The magnetic difference between point A and point B (y-side of the bubble) is positive since the magnetic pressure has the same versus of the liquid $(F \cdot dr > 0)$. This overpressure increases the total overpressure between A and B, and make the path more easy to follow by the liquid, Eq. (8.9). Physically higher velocity on the y-side is observed as shown in Figure 65.

$$\Delta p_{A \rightarrow B} = \int_A^B J \times B \cdot dr > 0 \tag{8.9}$$
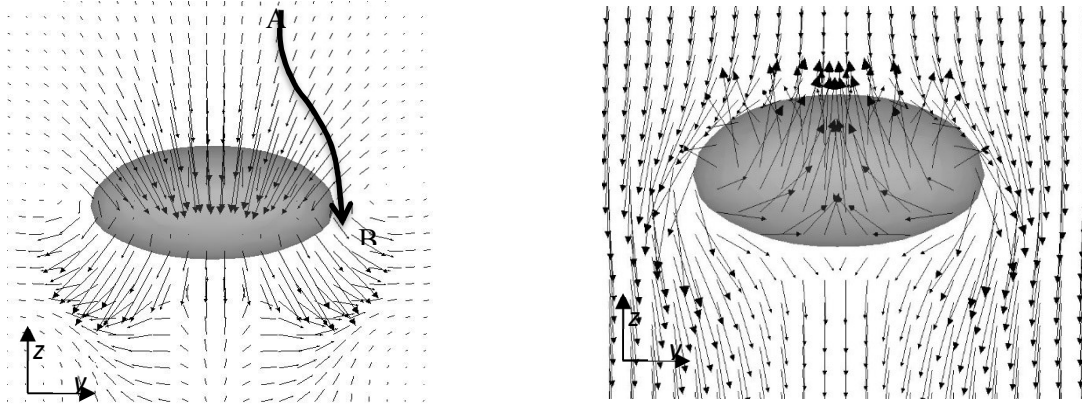
Figure 65 " y-z plane(x=0) of the Lorentz force (left). y-z plane(x=0) of the velocity field (right) ."

On the contrary the magnetic pressure between points C and D (x-side of the bubble) is lower since, for a certain region, the magnetic force and the streamline have opposite verses $(F \cdot dr < 0)$. The magnetic pressure drop between C and D will decreases the total pressure drop and makes the path more difficult to follow by the liquid, Eq. (8.10). Physically a lower velocity is observed on the x-side. Furthermore, it is demonstrated in the next paragraph that the magnetic overpressure on the x-side of the bubble is zero $\left(\Delta p_{magnetic} (\infty \rightarrow D) = p_{magnetic}(D) = 0 \right)$, see Figure 66.

$$\Delta p_{C \rightarrow D} = \int_C^D J \times B \cdot ds < \Delta p_{A \rightarrow B} \tag{8.10}$$
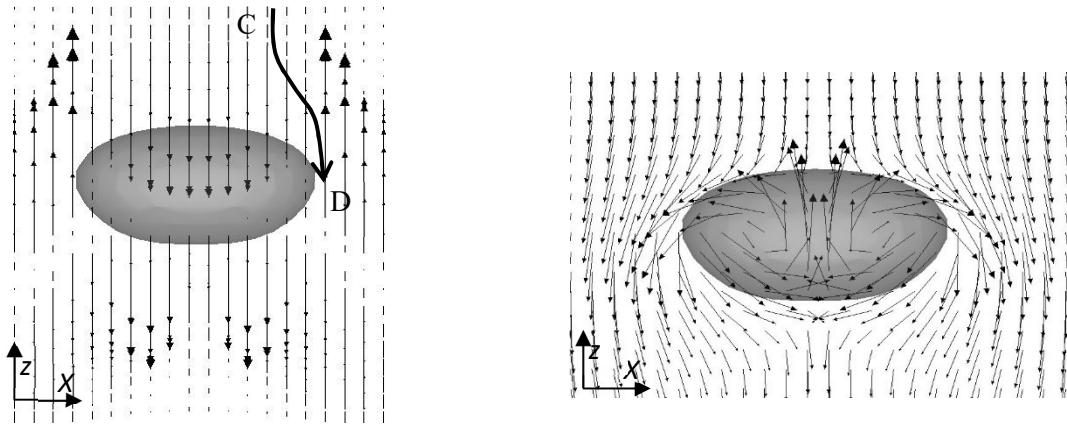
Figure 66 "x-z plane (y=0) of the Lorentz force(left). x-z plane(y=0) of the velocity field (right). "

In conclusion, different velocity fields are present on the x and y sides of the bubble. Nevertheless, simulations show the difference is quantitatively negligible and the liquid velocity field can be consider axisymmetric for simplicity. Therefore, same relations of the case $B = 0$ can be used in order to compute the velocity on the bubble side:

$$u\left(\theta = \frac{\pi}{2}\right) = u_{\infty} \cdot F(X)$$

, (8.11)

where $F(X)$ is defined as:

$$F(X) = \frac{\omega^2(X)}{\omega^2(X) - 1}$$

, (8.12)

and $\omega(X)$ is:

$$\omega(X) \approx \frac{\left(\sqrt{3} - 1\right)}{X^{1.34}} + 1$$

. (8.13)

8.2.3 Curvature at the top of the bubble

The lowest curvature appears at the top of the bubble since the highest pressure is observed on the liquid side around the top of the bubble. The simulation results show that the flow is irrotational in this region. Eq.(8.14) is a vector identity for irrotational flows.

$$u \cdot \nabla u = \frac{1}{2}\nabla u^2 + (\nabla \times u) \times u = \frac{1}{2}\nabla u^2 \tag{8.14}$$

The top of the bubble is a stagnation point $(u(s)=0)$. Here the simulation shows that the electric potential is spatially uniformly constant, i.e. $\nabla\phi=0$, which means that the $J = \sigma(-\nabla\varphi + u \times B) \cong \sigma(u \times B)$ and the Lorentz force $F = \sigma(u \times B \times B)$. As it can be seen in Eq. (8.15), both kinematic and magnetic pressure increase the outside pressure and tries to decreases the bubble local curvature.

$$\chi(s) = \frac{\gamma\chi_0 - \frac{1}{2}\rho u_\infty^2 - \sigma\int_\infty^s u \times B \times B \cdot dr}{\gamma} \tag{8.15}$$

In order to compute the magnetic over-pressure $\left(\sigma\int_\infty^s u \times B \times B \cdot dr\right)$, the magnetic force is integrated along a fluid streamline from infinity to the top of the bubble (Figure 67). The liquid streamline is vertical and has the same direction of the Lorentz force, so the integral become a simple scalar integral of the velocity.
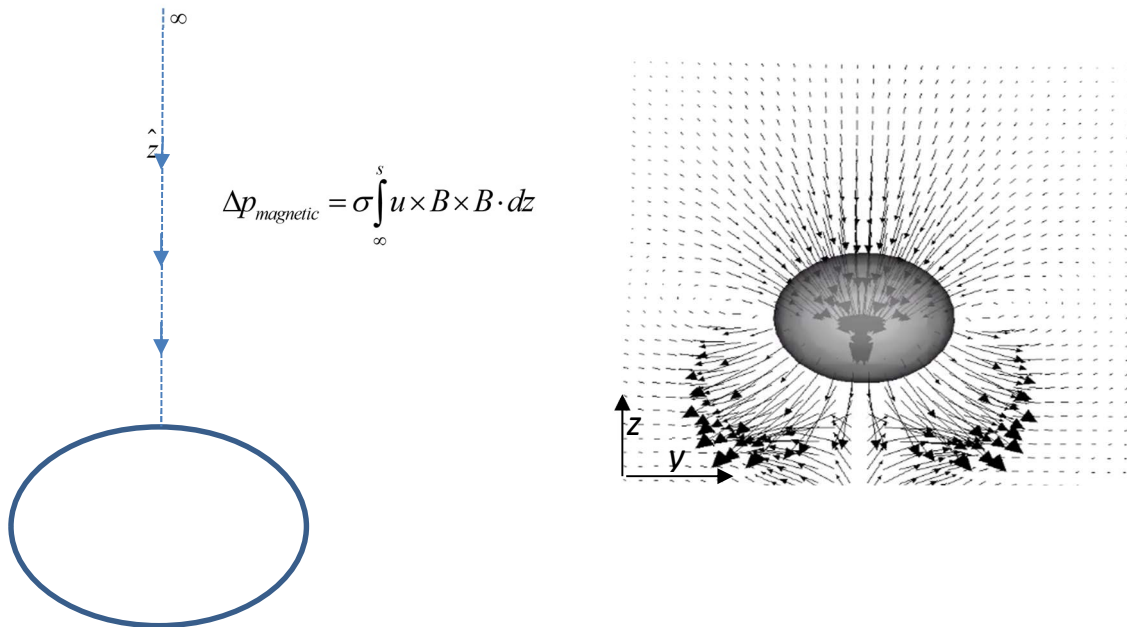

Figure 67 "z-y (x=0) section of the Lorentz Force (right)."

In the liquid above the bubble, the velocity field is irrotational and the velocity field admits a scalar potential δ . Actually, the velocity field can be expressed as Eq. (8.16).

$$\vec{u} = (u_x, u_y, u_z) = \left(\frac{\partial \delta}{\partial x}, \frac{\partial \delta}{\partial y}, \frac{\partial \delta}{\partial z} \right)$$

(8.16)

Therefore, the linear integral of the velocity is a function of only the velocity potential on the top of the bubble, Eq. (8.17). Unfortunately, a universal velocity potential cannot be analytically found for the MHD bubble rising problem.

$$\int_{\infty}^{s} u(z) \cdot dz = \int_{\infty}^{s} \frac{\partial \delta}{\partial z} \cdot dz = \delta(s) - \delta(\infty) = \delta(s)$$

(8.17)

In the region close to the integration line the flow is almost vertical $(u_z \gg u_x, u_y)$ for all z. Since the flow is vertical, also the magnetic force is vertical $F = \sigma(u \times B \times B)$. The magnetic force depends only on z and can be considered axisymmetric. In this tiny region, surrounding the integration line, all the forces are axisymmetric and therefore also the flow field. In the surroundings of on the integration line the flow field has the same shape of the B=0 case and the magnetic velocity potential can be approximated as the B0 velocity potential which is analytically known, Eq. (8.18).

$$\delta_{magnetic}(r, \vartheta) \approx \delta_{no-magnetic}(r, \vartheta) = -u_\infty R \cdot \left(\frac{r}{R} + \frac{1}{2} \left(\frac{R}{r} \right)^2 \right) \cdot \cos(\vartheta)$$

(8.18)

$$u_z = \frac{\partial \delta}{\partial z} = -u_\infty \left(1 - \frac{R^3}{z^3} \right)$$

(8.19)

The velocity field just found is the Lagrangian velocity Eq. (8.19) of the fluid. Since the magnetic force depends on the Eulerian velocity field, it is computed as Eq. (8.21).

$$\vec{u}_{Lagrangian} = \vec{u}_{Euler} - \vec{u}_\infty$$

(8.20)

$$u_{z.Euler} = -u_\infty \left(1 - \frac{R^3}{z^3} \right) + u_\infty = u_\infty \cdot \frac{R^3}{z^3}$$

(8.21)

The velocity on the top of the bubble decreases $\propto \frac{1}{z^3}$ from u_∞ to zero. In ellipsoidal bubble the z semi-axis a is different from R due to bubble contraction $\left(a = D \cdot \sqrt[3]{\frac{X}{8}} \right)$. The velocity field is expressed (8.22):

$$u_z = u_\infty \cdot \frac{a^3}{z^3}$$

(8.22)
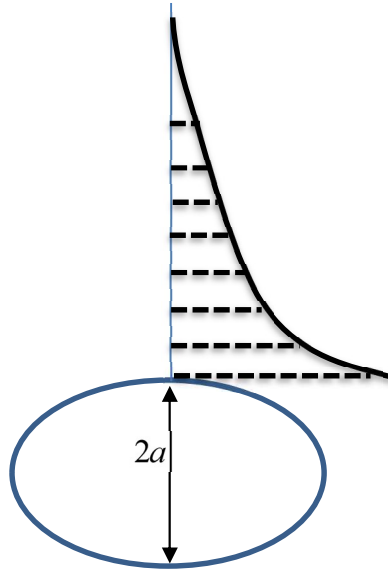
Figure 68 "Eulerian velocity magnitude on the top of the bubble."

The magnetic overpressure can be finally computed as Eq. (8.23).

$$\Delta p_{magnetic} = \sigma \int_\infty^a u \times B \times B \cdot dz = \sigma B^2 \cdot \int_\infty^a u(z) \cdot dz = \sigma B^2 u_\infty \cdot \int_\infty^a \frac{a^3}{z^3} dz = \frac{\sigma B^2 u_\infty a}{2}$$

(8.23)

Since $a = D \cdot \sqrt[3]{\dfrac{X}{8}}$, the overpressure can be arranged as function of initial quantities, Eq. (8.24).

$$\Delta p_{magnetic} = \frac{\sigma B^2 u_\infty D}{2} \cdot \sqrt[3]{\frac{X}{8}}$$

(8.24)

The top curvature can be expressed as Eq. (8.25):

$$\chi_{TOP} = \chi_0 + \frac{-\dfrac{1}{2}\rho u_\infty^2 - \dfrac{\sqrt[3]{X}}{4} \cdot \sigma B^2 u_\infty D}{\gamma}$$

(8.25)

8.2.4 X-Side Curvature

In order to calculate the curvature on the x side of the bubble, the local magnetic overpressure has to be calculated. The key point is to integrate MHD Navier-Stokes equations from far away to the point of

interest $(\infty \to P)$ in order to find how much the magnetic pressure changes (Figure 69). Since the magnetic force is not an irrotational field, the integration line has to be chosen carefully in order to make the calculi as much easy as possible. By considering steady state inviscid flow, the momentum equation can be re arranged as Eq. (8.28) (gravitational term is not considered since it has no impact on bubble shape). As it can be observed in Figure 69, the electric potential field ϕ is zero everywhere on the x-z plane (y=0). The $\nabla^2\phi$ is also zero since the potential field is constant. By Eq. (7.3) it can be demonstrated that the velocity field is irrotational $(\nabla \times u = 0)$.

$$\frac{\partial \rho u}{\partial t} + (u \cdot \nabla)u = -\nabla p + \mu \nabla^2 u + \rho g + J \times B$$

(8.26)

$$\frac{1}{2}\nabla u^2 + (\nabla \times u) \times u = -\nabla p + J \times B$$

(8.27)

$$\frac{1}{2}\nabla u^2 = -\nabla p + u \times B \times B$$

(8.28)

If the flow is irrotational, Bernoulli equation can be applied to any two points, also not belonging to the same streamline, Eq. (8.28). Since the potential is constant the magnetic force is simplified $(F = \sigma \cdot u \times B \times B)$.

The magnetic force is integrated from E to F (which is not a fluid streamline) in order to compute the magnetic overpressure on the x-side of the bubble. By the definition, the magnetic force does not have the x component since it has to be perpendicular to the external magnetic field. Therefore, the magnetic over-pressure on the x-side of the bubble is zero.
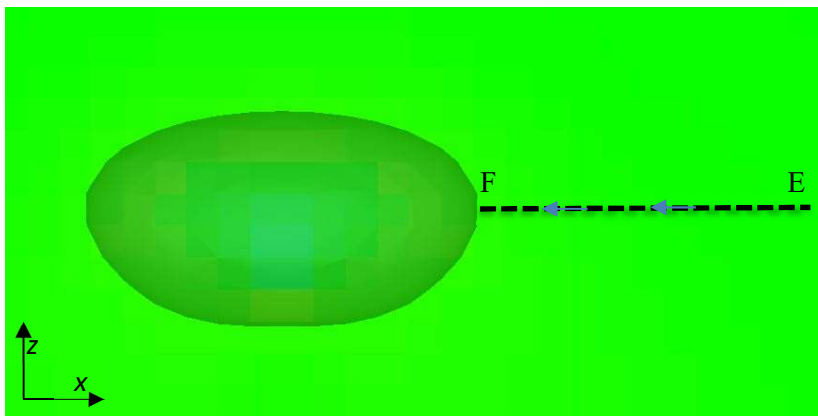
$$p_F = \int_E^F F \cdot d\hat{x} = \int_E^F F_x \cdot dx = 0$$

Figure 69 "x-z section (y=0) of the electrical potential field."

The x-side curvature has the same formula of the $B = 0$ case. Magnetic field does not affect directly the curvature and the kinematic pressure is the only component. The x-side curvature can be expressed as Eq. (8.29).

$$\chi_{X-SIDE} = \chi\left(\frac{\pi}{2}\right) = \chi_o - \frac{1}{2} \cdot \frac{\rho \cdot u_\infty^2}{\gamma} \cdot \left(1 - F^2(X)\right)$$

(8.29)

8.2.5 Y-Side Curvature

In order to compute the overpressure on the y-side of the bubble, the same procedure of the x-side case is used. Overpressure is found by a linear integration of the Navier-Stokes equations from far away to the bubble interface $(A \rightarrow B)$. The linear integral has been chosen along the y direction. In this region, the integration line is perpendicular to the liquid flow. As it can be seen in Figure 70, the electrical potential field is not zero $(\phi \neq 0)$ on the y-side of the bubble. Using Eq.(7.3), it is found that the flow field is not irrotational $(\nabla \times u \neq 0)$.

$$\frac{\partial \rho u}{\partial t} + \rho\left(u \cdot \nabla\right)u = -\nabla p + \mu \nabla^2 u + \rho g + J \times B$$

(8.30)

$$\frac{1}{2}\rho \nabla u^2 + \rho\left(\nabla \times u\right) \times u = -\nabla p + J \times B$$

(8.31)

$$\frac{1}{2}\rho \nabla u^2 + \rho\left(\nabla \times u\right) \times u = -\nabla p + \sigma\left(-\nabla \phi + u \times B\right) \times B$$

(8.32)

$$\frac{1}{2}\rho \nabla u^2 + \rho\left(\nabla \times u\right) \times u = -\nabla p - \sigma \nabla \phi + \sigma\left(u \times B \times B\right)$$

(8.33)

$$\Delta p_{AB} = \frac{1}{2}\rho \cdot \left(u_B^2 - u_A^2\right) - \sigma \int_A^B \nabla \phi(y) \cdot dy + \sigma \int_A^B \left(u \times B \times B\right) \cdot dy - \rho \int_A^B \left(\nabla \times u \times u\right) \cdot dy$$

(8.34)

The Lorentz magnetic pressure and the electrical potential pressure are analyzed separately. Since the flow-field is not irrotational and the integration line is not a streamline, there is a new component proportional to the rotor of the velocity field $\left(\int_A^B \left(\nabla \times u \times u\right) \cdot dy\right)$. The overpressure which influence the

bubble shape is the sum of a kinematic, electrical, Lorentz and rotational components, Eq. (8.34).

$$\Delta p_{kinematic} = \frac{1}{2}\rho \cdot \left(u_B^2 - u_A^2\right)$$

$$\Delta p_{electrical} = -\sigma \int_A^B \nabla\phi(y) \times B \cdot dy$$

$$\Delta p_{lorentz} = \sigma \int_A^B \left(u \times B \times B\right) \cdot dy$$

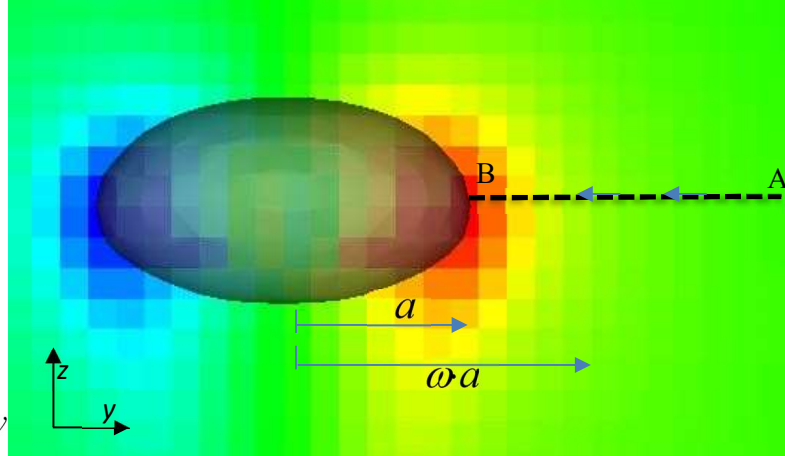$$\Delta p_{rotational} = -\rho \int_A^B \left(\nabla \times u \times u\right) \cdot dy$$

Figure 70 "y-z section (x=0) of the electric potential field."

The kinematic component depends only on the two velocities. For computing the velocity on the bubble side, axisymmetric approximation is adopted and the final pressure drop is Eq. (8.35).

$$\Delta p_{kinematic} = \frac{1}{2}\rho u_\infty^2 \left(1 - F^2(X)\right) \tag{8.35}$$

The Lorentz component $\Delta p_{lorentz} = \sigma \int_A^B \left(u \times B \times B\right) \cdot dy$ is zero. The Lorentz force $F = \sigma \left(u \times B \times B\right)$ is mathematically parallel to the velocity field in each point. On the border of the bubble, the velocity and also the Lorentz force have only a z component. The vector F is perpendicular to the integration line in each point $\left(F \perp d\hat{y}\right)$. Therefore, the Lorentz overpressure is zero.

The potential component can be processed as Eq. (8.36).

$$\Delta p_{electrical} = -\sigma \int_A^B \nabla\phi(y) \times B \cdot dy = -\sigma \int_A^B \left(0, -B \cdot \frac{\partial\phi}{\partial z}, -B\frac{\partial\phi}{\partial y}\right) \cdot (0, dy, 0) = +\sigma B \cdot \int_A^B \frac{\partial\phi}{\partial z}(y) \cdot dy \tag{8.36}$$

All point on the integration line are maximum points for the electrical potential on the z direction. Therefore $\frac{\partial\phi}{\partial z} = 0$ for each point on the line. The electrical overpressure is zero.

The rotational component can be processed as Eq. (8.37):

$$\Delta p_{rotational} = -\rho \int_A^B (\nabla \times u \times u) \cdot dy \qquad (8.37)$$

From Eq.(8.38) we found there is a proportionality between $\nabla^2 \phi$ and $\nabla \times u$ in each point since the liquid metal is a perfect conductor.

$$\nabla^2 \phi = B \cdot \nabla \times u \qquad (8.38)$$

$$\nabla^2 \phi = (B,0,0) \cdot \left(\frac{\partial u_z}{\partial y} - \frac{\partial u_y}{\partial z}, \frac{\partial u_z}{\partial x} - \frac{\partial u_x}{\partial z}, \frac{\partial u_y}{\partial x} - \frac{\partial u_x}{\partial y} \right) \qquad (8.39)$$

On the integration line u_x and u_y are zero and no variable depends on the x position. After some arrangement, the vector identity becomes a scalar identity, Eq. (8.41).

$$\nabla^2 \phi = (B,0,0) \cdot \left(\frac{\partial u_z}{\partial y} - \frac{\partial u_y}{\partial z}, 0, 0 \right) \qquad (8.40)$$

$$\nabla^2 \phi = B \left(\frac{\partial u_z}{\partial y} - \frac{\partial u_y}{\partial z} \right) \qquad (8.41)$$

By analyzing the $\nabla \times u \times u$ on the integration line, it follows Eq. (8.42):

$$\nabla \times u \times u = \left(\frac{\partial u_z}{\partial y} - \frac{\partial u_y}{\partial z}, 0, 0 \right) \times (0,0,u_z) = \left(0, \left[\frac{\partial u_z}{\partial y} - \frac{\partial u_y}{\partial z} \right] \cdot u_z, 0 \right) = \left(0, \frac{\nabla^2 \phi}{B} \cdot u_z, 0 \right) \qquad (8.42)$$

$\nabla \times u \times u$ is a vector which has only a y component. Therefore, the vector integral $\int_A^B (\nabla \times u \times u) \cdot dy$ becomes the scalar integral $\int_A^B |\nabla \times u \times u| \cdot dy$.

By any loss of generality it can be said Eq. (8.43) & Eq. (8.44):

$$\int_A^B (\nabla \times u \times u) \cdot dy = \int_A^B |\nabla \times u \times u| \cdot dy = \frac{1}{B} \int_A^B \nabla^2 \phi \cdot |u| \cdot dy \qquad (8.43)$$

$$\Delta p_{rotational} = -\frac{\rho}{B} \int_A^B (\nabla^2 \phi \cdot u_z) \cdot dy = -\frac{\rho}{B} \int_\infty^{\omega a} (\nabla^2 \phi \cdot u_z) \cdot dy - \frac{\rho}{B} \int_{\omega a}^a (\nabla^2 \phi \cdot u_z) \cdot dy \qquad (8.44)$$

In region with $r < \omega \cdot a$ the flow field is perturbed by the bubble, the velocity field is rotational and the electric field $(E = -\nabla \phi)$ is present. In region with $r > \omega \cdot a$ the flow is not influence by the bubble presence, the velocity field is spatially constant and irrotational. In this region, therefore, also the $\nabla^2 \phi$ is zero $\left(\dfrac{\rho}{B} \int\limits_{\infty}^{\omega a} \nabla^2 \phi \cdot u_z \cdot dy = 0 \right)$.
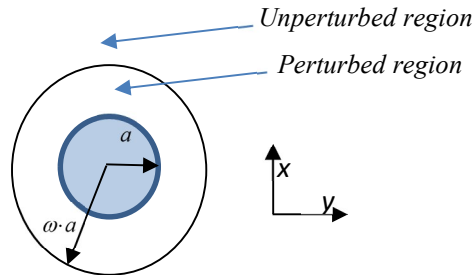

Figure 71 "Top view of the bubble."

The rotational contribution to the total pressure is given only by the perturbed region only, Eq. (8.45).

$$\Delta p_{rotational} = -\frac{\rho}{B} \int\limits_{\omega a}^{a} \left(\nabla^2 \phi \cdot u_z \right) \cdot dy \qquad (8.45)$$

Technically in the perturbed region, both the velocity and the potential vary with the distance. Nevertheless in the "Bubble Shape Theory" chapter an equivalent model has been adopted (Figure 72). In this model the velocity in the perturbed region is constant and equal to the surface velocity $u\left(90^o\right)$. From real velocity field and modeled one, the liquid flowrate is preserved.
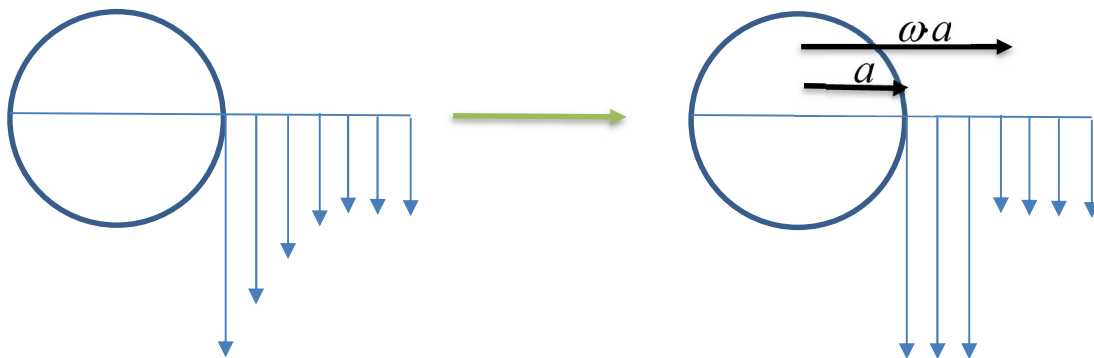

Figure 72 "Difference between real velocity field and modeled one for a spherical body."

By definition: $\int\limits_{\omega a}^{a} u(y) \cdot dy = u\left(90^o\right) \cdot \left(\omega - 1\right) a$

Under the approximation that the real velocity does not change to rapidly on y direction, the upper formula can be simplified in Eq. (8.46):

$$\Delta p_{rotational} = -\frac{\rho}{B}\int_{\omega a}^{a}\left(\nabla^2\phi \cdot u_z\right)\cdot dy \approx -\frac{\rho \cdot u\left(90^0\right)}{B}\int_{\omega a}^{a}\nabla^2\phi(y)\cdot dy \tag{8.46}$$

On the integration line the electric potential in on its maximum along the x and z axis, which mean that $\frac{\partial \phi}{\partial x}$ and $\frac{\partial \phi}{\partial z}$ are zero on the line. Since they are maximum the concavity of the function is negative and $\frac{\partial^2 \phi}{\partial x^2}$ and $\frac{\partial^2 \phi}{\partial z^2}$ are < 0 for each point of the integration line (Figure 73).
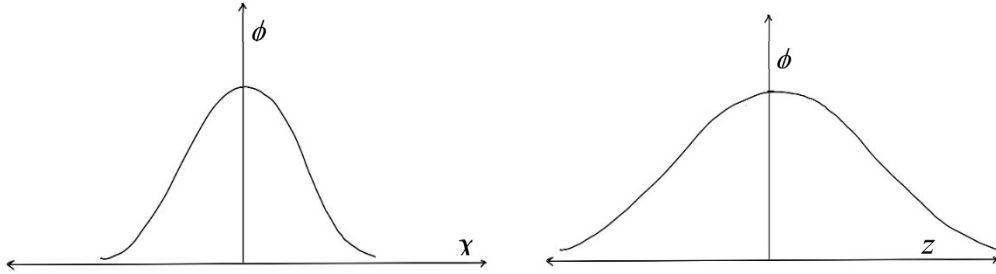

Figure 73 "Qualitative representation of the electric potential vs x on the integration line for any y (left). Qualitative representation of the electric potential vs z on the integration line for any y (right)."

$$\Delta p_{rotational} \approx -\frac{\rho \cdot u\left(90^0\right)}{B}\int_{\omega a}^{a}\left(\frac{\partial^2 \phi}{\partial x^2}+\frac{\partial^2 \phi}{\partial y^2}+\frac{\partial^2 \phi}{\partial z^2}\right)\cdot dy \tag{8.47}$$

$$\Delta p_{rotational} \approx -\frac{\rho \cdot u\left(90^0\right)}{B}\left[\int_{\omega a}^{a}\left(\frac{\partial^2 \phi}{\partial x^2}+\frac{\partial^2 \phi}{\partial z^2}\right)\cdot dy + \int_{\omega a}^{a}\frac{\partial^2 \phi}{\partial y^2}\cdot dy\right] \tag{8.48}$$

The last term can be proceed as Eq. (8.49):

$$\int_{\omega a}^{a}\frac{\partial^2 \phi}{\partial y^2}\cdot dy = -\int_{\omega a}^{a}\frac{\partial}{\partial y}E_y \cdot dy = E_y\left(\omega a\right)-E_y\left(a\right)=0 \tag{8.49}$$

The electric field at the distance a and ωa from the bubble center is zero, since the electric potential is flat (Figure 74). Therefore, the last term is zero and it does not influence the rotational overpressure.
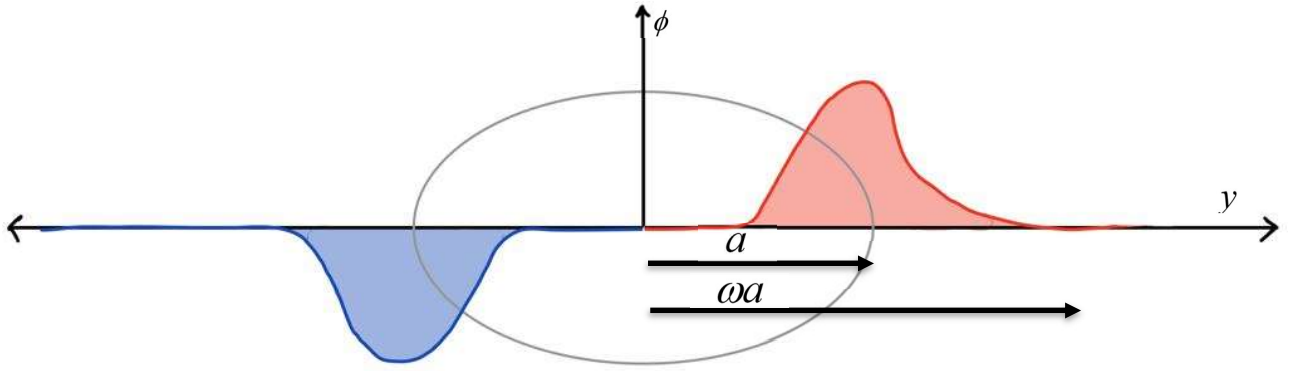
Figure 74 "Electrical potential vs. y (x=0,z=0)."

The final expression of the rotational overpressure is Eq. (8.51):

$$\Delta p_{rotational} \approx -\frac{\rho u\left(90^0\right)}{B} \cdot \int_{\omega a}^{a}\left(\frac{\partial^2 \phi}{\partial x^2}+\frac{\partial^2 \phi}{\partial z^2}\right)\cdot dy \qquad (8.50)$$

$$\Delta p_{rotational} \approx \frac{\rho u\left(90^0\right)}{B} \cdot \int_{a}^{\omega a}\left(\frac{\partial^2 \phi}{\partial x^2}+\frac{\partial^2 \phi}{\partial z^2}\right)\cdot dy \qquad (8.51)$$

Since $\dfrac{\partial^2 \phi}{\partial x^2}+\dfrac{\partial^2 \phi}{\partial z^2}$ are negative in each point, the linear integral will be negative as well. The rotational component leads to an under-pressure on the y-side of the bubble. This under-pressure appears only in the y-side and not on the x-side and it is the main reason of the different elongation on the x-y plane. Rotational overpressure pulls the bubble only on the y side. This is the reason why $X_Y > X_X$.

Finally the y-side curvature can be computed as Eq. (8.53):

$$\chi(s) = \chi_0 + \frac{\Delta p_{KIN} + \Delta p_{ROT}}{\gamma} \qquad (8.52)$$

$$\chi_{Y-SIDE} = \chi_0 + \frac{\dfrac{1}{2}\rho u_\infty^2\left(1-F^2(X)\right)+\dfrac{\rho u_\infty \cdot F(X)}{B}\cdot \int_{a}^{\omega a}\left(\dfrac{\partial^2 \phi}{\partial x^2}+\dfrac{\partial^2 \phi}{\partial z^2}\right)\cdot dy}{\gamma} \qquad (8.53)$$

8.2.6 Aspect ratio Calculation

Now, since the x-side and y-side curvature are computed, the average side curvature is computed as Eq. (8.54).

$$\chi_{SIDE} = \frac{\chi_{X-SIDE} + \chi_{Y-SIDE}}{2} = \chi_0 + \frac{\frac{1}{2}\rho u_\infty^2 \left(1 - F^2(X)\right) + \frac{\rho u_\infty \cdot F(X)}{2B} \cdot \int\limits_a^{\omega a} \left(\frac{\partial^2 \phi}{\partial x^2} + \frac{\partial^2 \phi}{\partial z^2}\right) \cdot dy}{\gamma} \tag{8.54}$$

The rotor overpressure is a pressure component present only on the y-side of the bubble. Its presence is essential to explain why the y aspect ratio and x aspect ratio are different. Nevertheless, the relative difference between X_Y and X_X is less than 5 % for all the bubble computed. This mean that the $\Delta p_{rot.}$ does exist but it has not a strong macroscopic influence on the final aspect ratio. It can be said that the side curvature is mainly controlled by the kinematic pressure, Eq. (8.55) $\left(\Delta p_{kinematic} \gg \Delta p_{rot.}\right)$.

$$\frac{1}{2}\rho u_\infty^2 \left(1 - F^2(X)\right) \gg \frac{\rho u_\infty \cdot F(X)}{B} \cdot \int\limits_a^{\omega a} \left(\frac{\partial^2 \phi}{\partial x^2} + \frac{\partial^2 \phi}{\partial z^2}\right) \cdot dy \tag{8.55}$$

$$\chi_{SIDE} = \chi_0 + \frac{\frac{1}{2}\rho u_\infty^2 \left(1 - F^2(X)\right)}{\gamma} \tag{8.56}$$

One the average side curvature and the top curvature are computed, the bubble shape can be considered for simplicity axisymmetric and the final aspect ratio can be calculated. Same relation of the B0 case are used in this section.
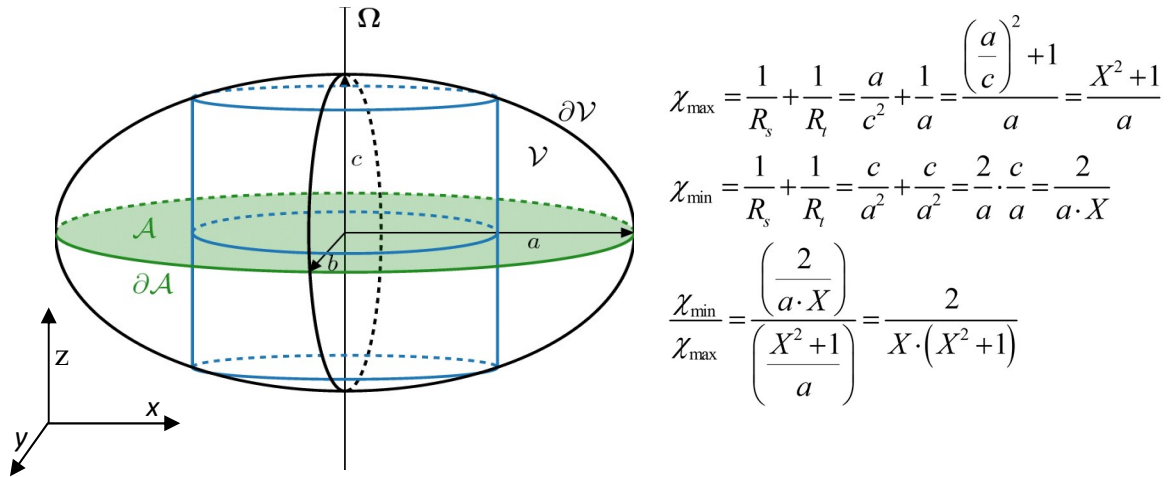

$$\chi_{max} = \frac{1}{R_s} + \frac{1}{R_t} = \frac{a}{c^2} + \frac{1}{a} = \frac{\left(\frac{a}{c}\right)^2 + 1}{a} = \frac{X^2 + 1}{a}$$

$$\chi_{min} = \frac{1}{R_s} + \frac{1}{R_t} = \frac{c}{a^2} + \frac{c}{a^2} = \frac{2}{a} \cdot \frac{c}{a} = \frac{2}{a \cdot X}$$

$$\frac{\chi_{min}}{\chi_{max}} = \frac{\left(\frac{2}{a \cdot X}\right)}{\left(\frac{X^2 + 1}{a}\right)} = \frac{2}{X \cdot \left(X^2 + 1\right)}$$

Figure 75 "Analytical relation between top and bottom curvature and aspect ratio for a symmetric ellipsoid."

Under this reasonable approximation, the final aspect ratio can be computed as Eq. (8.57).

$$\frac{\chi_{min}}{\chi_{max}} = \frac{\chi_{TOP}}{\chi_{SIDE}} = \frac{2}{X \cdot \left(X^2 + 1\right)} = \frac{4 - \frac{1}{2} \cdot \frac{\rho \cdot u_\infty^2 \cdot D}{\gamma} - \frac{\sqrt[3]{X}}{4} \cdot \frac{\sigma B^2 u_\infty D^2}{\gamma}}{4 - \frac{1}{2} \cdot \frac{\rho \cdot u_\infty^2 \cdot D}{\gamma} \cdot \left(1 - F^2(X)\right)} \tag{8.57}$$

101

$$\frac{2}{X \cdot \left(X^2 + 1\right)} = \frac{4 - \dfrac{1}{2} \cdot We - \dfrac{\sqrt[3]{X}}{4} \cdot K}{4 - \dfrac{1}{2} \cdot We \cdot \left(1 - F^2(X)\right)}$$

(8.58)

$$\frac{2}{X \cdot \left(X^2 + 1\right)} = \frac{16 - 2We - \sqrt[3]{X} \cdot K}{16 - 2We \cdot \left(1 - F^2(X)\right)}$$

(8.59)

By re-arranging terms, the Eq. (8.60) is found.

$$We = \frac{8X\left(X^2 + 1\right) - 16}{X\left(X^2 + 1\right) + 2\left(F^2(X) - 1\right)} - K \cdot \frac{X^{\frac{4}{3}}\left(X^2 + 1\right)}{2X\left(X^2 + 1\right) + 4\left(F^2(X) - 1\right)}$$

(8.60)

The final Weber number is the sum of two term. The first term is the same as the analytical solution for the $B = 0$. The second term is magnetic field dependent. It is interesting to note that $\dfrac{X^{\frac{4}{3}}\left(X^2 + 1\right)}{2X\left(X^2 + 1\right) + 4\left(F^2(X) - 1\right)}$ is always positive for any aspect ratio X. Therefore the $We(X)$ under the presence of a magnetic field will be lower compare to $We(X)$ for $B = 0$ case for any aspect ratio:

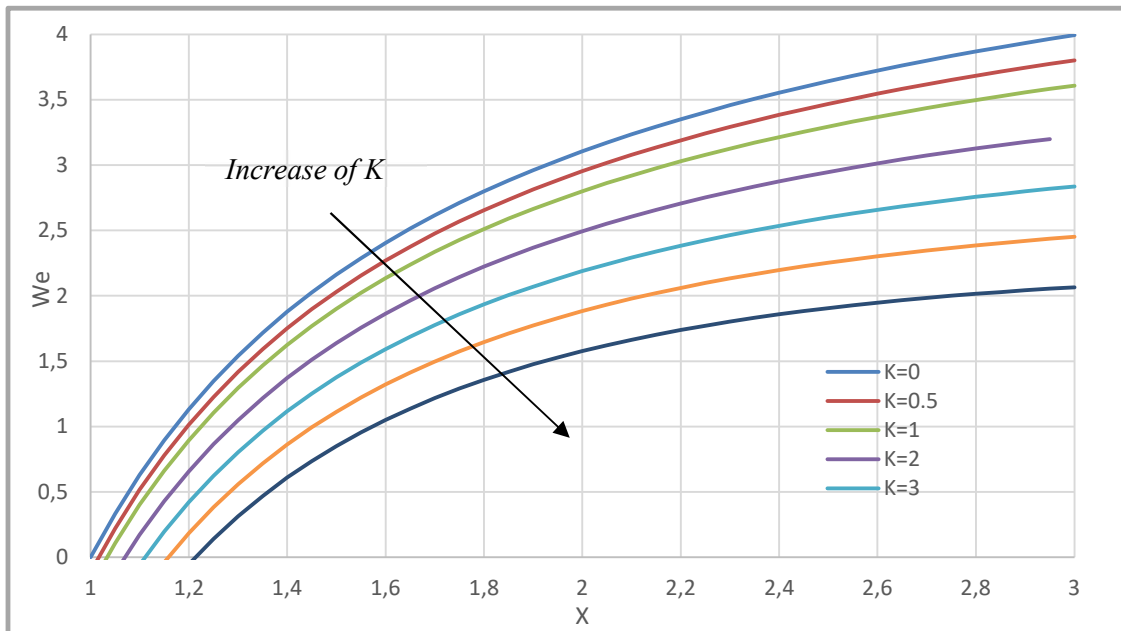$We(X, K_1) < We(X, K_2)$ for $K_1 > K_2$ for $\forall X$.

Figure 76 "We(X) under different K."

Once the Weber number and the *K* for the bubble are known, the aspect ratio can be easily found from Figure 76. In other words, the aspect ratio is the function of *We* and *K*:

$$X = F(We, K)$$

(8.61)

The dimensionless parameter $K = \dfrac{\sigma u_\infty B^2 D^2}{\gamma}$ represents the presence of the magnetic overpressure action on the top of the bubble. As it is shown in Eq.(8.58), the numerator is the sum of a Weber dependent part and a K dependent part. If We is much greater than K, the magnetic pressure component is negligible and the *We* (*X*, *B* = 0) shape function can be used. Once again the number which represents the relative importance of the magnetic forces compared to the kinematic ones is the Stuart number $N = \dfrac{K}{We}$.

$$N \ll 1$$

(8.62)

$$\frac{\sigma B^2 D}{\rho u_\infty} \ll 1$$

(8.63)

The above formula suggests that the analytical solution for *B* = 0 is still valid especially for small bubble (small *D*) or for weak magnetic field (small B^2).

8.2.7 Comparison of aspect ratio between analytical solution and PSI-BOIL

The new analytical solution for the aspect ratio under magnetic field is compared with the computed result of PSI-BOIL in this section. As it can be seen in Figure 77, low *X* region is characterized generally by little diameters. In this region all the line are converging to the B0 case line. This is due to the fact that, since the bubble are small, the Stuart parameter is small $\left(N \propto D\right)$. Furthermore, *B* = 0.5 line is really close to the B0 line because for these bubbles the Stuart number is really low $\left(N \propto B^2\right)$. For both cases the Stuart number is little and the analytical solution for *B* = 0 is applicable.

Nevertheless, for large bubble under strong magnetic field (A), magnetic pressure starts to play an important role and the analytical solution for the case without magnetic field (*B* = 0) is not able to precisely predict bubble aspect ratio.
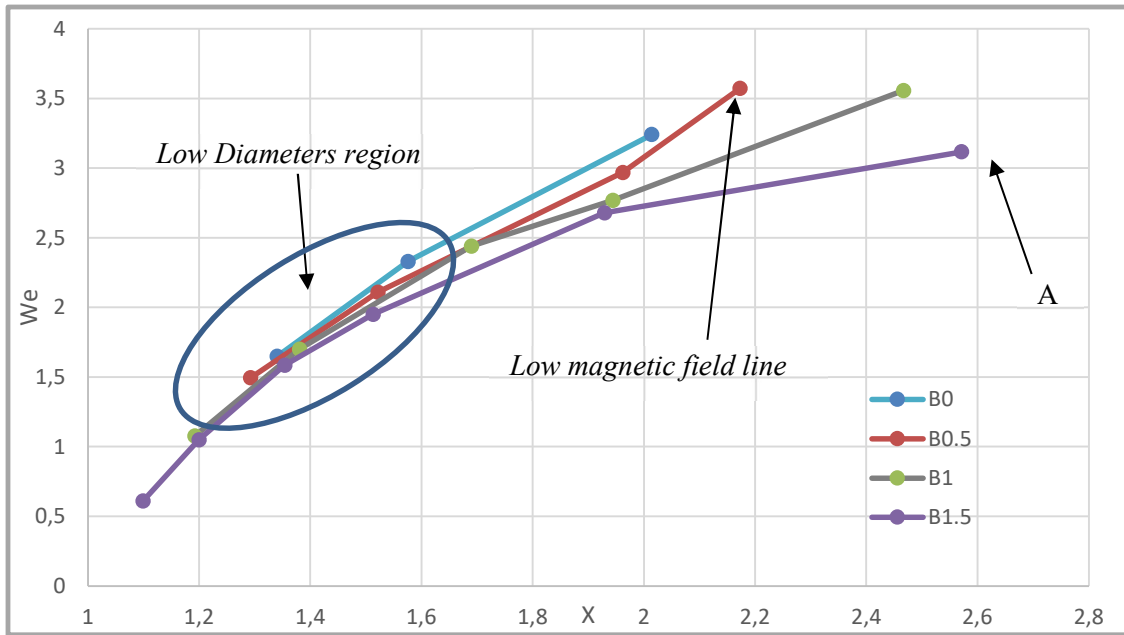
Figure 77 "We as the function of X for different applied magnetic fields."

8.3   Non uniform x-y elongation

During the raise-up the bubble deformed from spherical to a stretched shape. In order to conserve the volume, a contraction on z direction leads to an expansion on the x-y plane. As discussed before, the application of a strong B_{ext} reduced the final X. Therefore, the bubble x-y elongation is less strong compared to a $B_{ext} = 0$ case.

In the case of $B = 0$, the only driven factor is the kinematic pressure. An overpressure on the top and bottom of the bubble is produced while an under-pressure on the sides of the bubble is created. This lead to an axisymmetric compression of the bubble.

Under the presence of an external magnetic field, the rising bubble phenomena is not an axisymmetric process and the magnetic pressure plays also a important role. As discussed before the velocity field on x and y plane is different because the anisotropy of the Magnetic force ($F = J \times B$). On all the simulations a higher elongation on the y direction ($\perp B$) compare to x direction ($\parallel B$) has been found. Magnetic pressure affects the bubble shape in an indirect and direct way.

- Magnetic force influence the velocity field around the bubble and changes the kinematic under-pressure the bubble experiments on its side (Figure 78). The z component of the Lorentz force decreases the velocity of the liquid only on the x-sides of the bubble and not on the y-sides. Lorentz force therefore decreases the magnitude of the kinematic overpressure on the x-side. This will produce a lower kinematic under-pressure on the x-side of the bubble which produce a low elongation on the x direction.
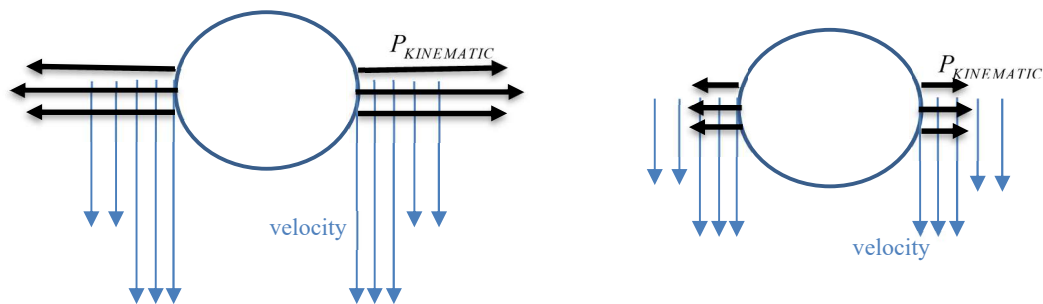

Figure 78 "(Left)y-z section of Kinematic pressure and velocity on bubble sides under external magnetic field. (Right):x-z section of Kinematic pressure and velocity on bubble sides under external magnetic field ."

- The dominating phenomenon which makes the bubble's compression not symmetric is the rotational pressure $\Delta p_{rot.}$ which, as demonstrated before, is un under-pressure present only on the y-side of the bubble Eq. (8.64).

$$\Delta p_{rotational} \approx \frac{\rho u\left(90^0\right)}{B} \cdot \int_{a}^{\omega a} \left(\frac{\partial^2 \phi}{\partial x^2} + \frac{\partial^2 \phi}{\partial z^2} \right) \cdot dy \tag{8.64}$$

Furthermore, the bubble shape tends to be not completely ellipsoidal under strong magnetic field. A satisfactory explanation can be found studying the x and y component of the Lorentz Force acting on the bubble surface. From the magnetic force definition $F = J \times B$, since the B has only the x component, the F has to be perpendicular to B in each point and therefore $F_x = 0$. Instead, the F_y exists and produced a compressive stress field on the top of the bubble and a tensile stress field on the bottom (Figure 81).
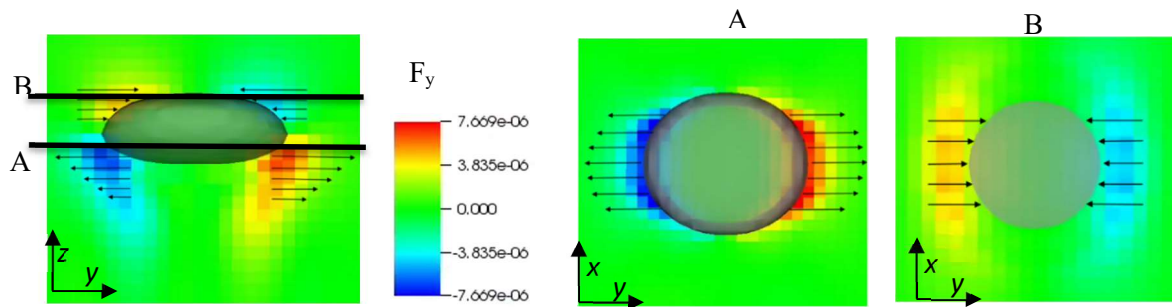

Figure 81"y-z plane of Fy of Lorentz force (D= 5.76 mm)." *Figure 81 "[A] y-x plane of Fy of Lorentz Force (D= 5.76 mm). "* *Figure 81 " [B] y-x plane of Fy of Lorentz Force (D= 5.76 mm)."*

Since only the y component is present, the deformation takes place only on the y-sides of the bubble while the x-side are kept constant. Figure 82 shows that the x-z and y-z section of the bubble are slightly different.
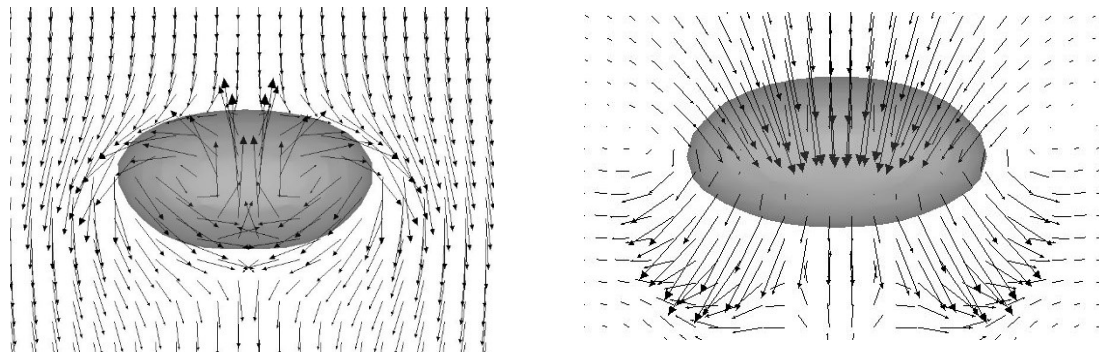

Figure 82 "On the left x-z(y=0) section of the bubble, on the right y-z(x=0) section of the bubble."

8.4   Limitation of the analytical solution for the bubble aspect ratio under magnetic field

The analytical solution for the bubble aspect ratio assumes the bubble shape tends to be ellipsoidal. In this approach, the top and bottom bubble curvature are assumed to be the same. As it is known, bubble local curvature depends on the outer kinematic and magnetic pressure:

$$\chi(s) = \frac{\gamma \chi_0 - \frac{1}{2}\rho u_\infty^2 - \sigma \int_\infty^s u \times B \times B \cdot dr}{\gamma}.$$
(8.65)

Both the top and the bottom of the bubble can be considered stagnation points and therefore in both points the kinematic pressure is equal to $\frac{1}{2}\rho u_\infty^2$. Nevertheless, in reality the magnetic pressures on the top and bottom of the bubble are different. As it can be seen in Figure 83, on the top of the bubble the magnetic force produced an overpressure $\left(F_{lorentz} \cdot dr > 0\right)$ while on the bottom of the bubble the magnetic force produced un under-pressure $\left(F_{lorentz} \cdot dr < 0\right)$. On the top the Lorentz force is facing the surface while on the bottom it points outwards. In the analytical solution for the bubble aspect ratio under the magnetic field, the magnetic pressure acting on the top of the bubble is precisely predicted while no consideration are made for the bottom.

In the MHD shape theory, magnetic pressure on the bottom is considered positive and equal to the top magnetic pressure. This approximation is necessary made to consider the bubble ellipsoidal and to compute the aspect ratio but, with this approximation, the total pressure on the bottom is overestimated and the bottom curvature is underestimated.
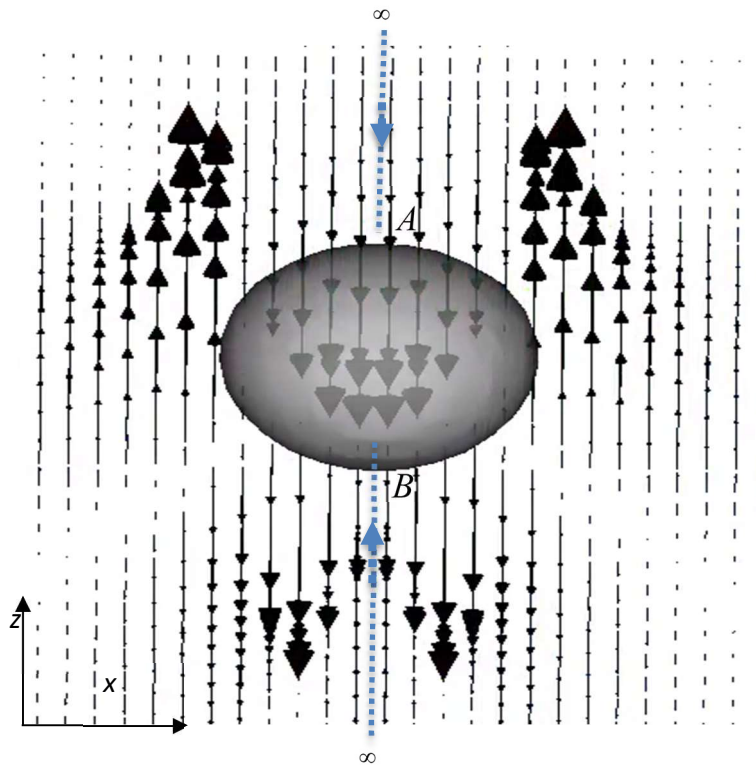
$$P_{A-magnetic} = \int_{\infty}^{A} F_{magnetic} \cdot ds > 0$$

$$P_{B-magnetic} = \int_{\infty}^{B} F_{magnetic} \cdot ds < 0$$

$$P_{A-magnetic} > 0 > P_{B-magnetic}$$

Figure 83" x-z plane of Lorentz force field (D= 1.2 mm)."

In MHD shape theory the ellipsoid is reconstructed by knowing the top curvature χ_{TOP} and the side curvature χ_{SIDE}. Figure 84 shows that the real bubble aspect ratio is lower than the one predicted by the theory. Therefore, the MHD shape theory leads to slightly overestimate the aspect ratio.
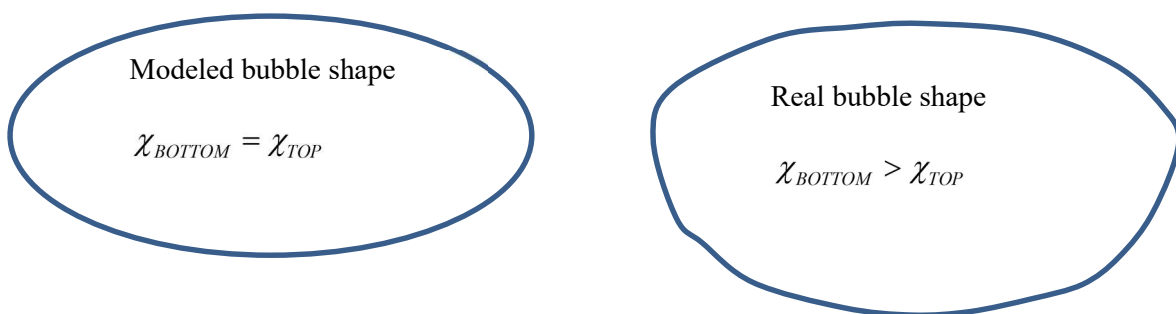
Figure 84 " Difference between model and real bubble shape."

The error between real aspect ratio and the modeled one increases if the importance of the magnetic pressure over the kinematic pressure increases. Therefore, this "systematic error" on the aspect ratio monotonously increases with the Stuart number $\left(N = \dfrac{K}{We} \right)$. Once the magnetic pressure become the predominant force $(N \gg 1)$, the MHD shape theory does not produced reasonable results because the

bubble cannot anymore assumed to be ellipsoidal anymore. The ellipsoidal theory work well for simple bubble in liquid metals because bottom and top curvature are equal since they depends only on the kinematic pressure. In the cases with magnetic field, top and bottom curvature are influenced also on the Lorentz force. The magnetic force produces an overpressure on the top and an under-pressure on the bottom. Therefore, top and bottom curvature cannot be approximated to be the same and MHD shape theory losses it efficiency for high N case. Basically, the Lorentz force is not symmetric respect the z axis but points down everywhere. Therefore, magnetic pressure on the top and bottom of the bubble have different sign and elliptical theory becomes no more valid.

9 Conclusions

In this study, Computational Fluid Dynamics (CFD) simulation was used to derive full understanding of a bubble rising in liquid metals with and without the presence of an external magnetic field. More precisely, the bubble rising velocity and the bubble deformation were investigated using the CFD/HMD code, PSI-BOIL.

First a rising bubble in liquid metal without magnetic field was undertaken, and the predicted terminal rising velocity was compared to the Tomiyama's correlation. The simulation results feature that the drag coefficient is controlled by only the Eotvos number for the large bubbles, which shows the same tendency as Tomiyama's correlation. Then, a semi-analytical model for the bubble shape deformation was newly derived for liquid metal and compared with simulation results. The result shows that inviscid approximation works satisfactory well for bubbles in liquid metal, and the bubble shape deformation is controlled only by the Weber number. Furthermore, a new stability criterion for bubbles in liquid metal regime was proposed. In the proposed criterion, the bubble stability in liquid metal considered is not controlled by the Morton number but only by Eotvos number. Transition from ellipsoidal to wobbling disc shape takes place at the fixed Eotvos number ($Eo = 1.7$).

Second, a single bubble rising in liquid metals under the presence of an external horizontal magnetic field was simulated for three systems with different combination of materials: argon-GaInSn, nitrogen-mercury and ar-iron. A generalized velocity correlation, which can be applied for a rising bubble under horizontal magnetic field, was proposed by modifying the Mendelson equation. The simulation results showed that weak magnetic field ($N < 0.8$) slightly increases the bubble rising velocity for larger bubble ($Eo > 1.7$), while stronger magnetic field ($N > 1$) causes the decrease of the velocity regardless the bubble sizes. The bubble shape deformation was explained and discussed in detail. An analytical MHD bubble shape theory was derived and compared with the experiments in order to explain how shape deformation is influenced by the bubble size and by the applied magnetic field. The influence of the magnetic field on the bubble stability was studied as well by basic principles, in which a horizontal magnetic field enhances the stability of the bubble, straightens the bubble trajectory and reduces the velocity and shape oscillation.

References

1. Kang, I.S.; Leal, L.G. The drag coefficient for a spherical bubble in a uniform streaming flow. *The Physics of Fluids* **1988**, *31*, 233-237, doi:10.1063/1.866852.
2. Hadamard, J.S. Mouvement Permanent Lent d'une Sphere Liquide et Visqueusedans un Liquide Visqueux. *C. R. Acad. Sci.* **1911**, *152*.
3. Tomiyama, A.; Kataoka, I.; Zun, I.; Sakaguchi, T. Drag Coefficients of Single Bubbles under Normal and Micro Gravity Conditions. *JSME International Journal Series B* **1998**, *41*, 472-479, doi:10.1299/jsmeb.41.472.
4. Mendelson, H.D. The prediction of bubble terminal velocities from wave theory. *AIChE Journal* **1967**, *13*, 250-253, doi:https://doi.org/10.1002/aic.690130213.
5. Mori, Y.; Hijikata, K.; Kuriyama, I. Experimental study of bubble motion in mercury with and without a magnetic field. *Journal of Heat Transfer* **1977**, *99*, 404-410, doi:10.1115/1.3450710.
6. Wang, Z.H.; Wang, S.D.; Meng, X.; Ni, M.J. UDV measurements of single bubble rising in a liquid metal Galinstan with a transverse magnetic field. *International Journal of Multiphase Flow* **2017**, *94*, 201-208, doi:https://doi.org/10.1016/j.ijmultiphaseflow.2017.05.001.
7. Jin, K.; Kumar, P.; Vanka, S.P.; Thomas, B.G. Rise of an argon bubble in liquid steel in the presence of a transverse magnetic field. *Physics of Fluids* **2016**, *28*, 093301, doi:10.1063/1.4961561.
8. Zhang, C.; Eckert, S.; Gerbeth, G. Experimental study of single bubble motion in a liquid metal column exposed to a DC magnetic field. *International Journal of Multiphase Flow* **2005**, *31*, 824-842, doi:https://doi.org/10.1016/j.ijmultiphaseflow.2005.05.001.
9. Zhang, C.; Eckert, S.; Gerbeth, G. The flow structure of a bubble-driven liquid-metal jet in a horizontal magnetic field. *Journal of Fluid Mechanics* **2007**, *575*, 57-82, doi:10.1017/S0022112006004423.
10. Shibasaki, Y.; Ueno, K.; Tagawa, T. Computation of a rising bubble in an enclosure filled with liquid metal under vertical magnetic fields. *ISIJ International* **2010**, *50*, 363-370, doi:10.2355/isijinternational.50.363.
11. Zhang, J.; Ni, M.-J. Direct simulation of single bubble motion under vertical magnetic field: Paths and wakes. *Physics of Fluids* **2014**, *26*, 102102, doi:10.1063/1.4896775.
12. Chorin, A.J. Numerical solution of the Navier-Stokes equations. *Math. Comp.* **1968**, *22*, 745-762.
13. Harlow, F.H.; Welch, J.E. Numerical calculation of time-dependent viscous incompressible flow of fluid with free surface. *Phys. Fluids* **1965**, *8*, 2182-2189.
14. Roe, P.L. Characteristic-based schemes for the Euler equations. *Annu. Rev. Fluid Mech.* **1986**, *18*, 337-365, doi:doi:10.1146/annurev.fl.18.010186.002005.
15. Zhang, J.; Ni, M.-J.; Moreau, R. Rising motion of a single bubble through a liquid metal in the presence of a horizontal magnetic field. *Physics of Fluids* **2016**, *28*, 032101, doi:10.1063/1.4942014.
16. MOORE, D.W. The rise of a gas bubble in a visocus liquid. *Department of Mathematics, University of Bristol* **1958**.
17. Tomiyama, A.; Celata, G.P.; Hosokawa, S.; Yoshida, S. Terminal velocity of single bubbles in surface tension force dominant regime. *International Journal of Multiphase Flow* **2002**, *28*, 1497-1519, doi:https://doi.org/10.1016/S0301-9322(02)00032-0.
18. Haas, T.; Schubert, C.; Eickhoff, M.; Pfeifer, H. A Review of Bubble Dynamics in Liquid Metals. *Metals* **2021**, *11*, doi:10.3390/met11040664.

19. Clift, R.; Gauvin, W.H. Motion of entrained particles in gas streams. *The Canadian Journal of Chemical Engineering* **1971**, *49*, 439-448, doi:https://doi.org/10.1002/cjce.5450490403.

20. Abbassi, W.; Besbes, S.; Aissia, H.; Champagne, J.-Y. Study of the rise of a single/multiple bubbles in quiescent liquids using the VOF method. *Journal of the Brazilian Society of Mechanical Sciences and Engineering* **2019**, *41*, doi:10.1007/s40430-019-1759-y.

21. Kobayashi, H. Large eddy simulation of magnetohydrodynamic turbulent duct flows. *Physics of Fluids* **2008**, *20*, 015102, doi:10.1063/1.2832779.

22. Yen, C.H.; Hui, U.J.; We, Y.Y.; Sadikin, A.; Nordin, N.; Taib, I.; Abdullah, K.; Mohammed, A.N.; Sapit, A.; Razali, M.A. Numerical study of flow past a solid sphere at high Reynolds number. *IOP Conference Series: Materials Science and Engineering* **2017**, *243*, 012042, doi:10.1088/1757-899x/243/1/012042.

23. Lamb, H. Hydrodynamics, 6th ed. *Cambridge University Press.* **1932**.

24. Legendre, D. On the relation between the drag and the vorticity produced on a clean bubble. *Physics of Fluids* **2007**, *19*, 018102, doi:10.1063/1.2430645.

25. SEARS, R.A.H.W.R. On the instability of small gas bubbles moving uniformly in various liquids. *Graduate School of Aernautical Engineering , Cornell University, Ithaca* **1957**.

26. Denner, F.; van Wachem, B.G.M. Numerical time-step restrictions as a result of capillary waves. *Journal of Computational Physics* **2015**, *285*, 24-40, doi:https://doi.org/10.1016/j.jcp.2015.01.021.

27. Kordač, M.; Košek, L. Helium bubble formation in Pb-16Li within the breeding blanket. *Fusion Engineering and Design* **2017**, *124*, doi:10.1016/j.fusengdes.2017.05.100.

28. Liu, Z.; Li, B. Large-Eddy Simulation of Transient Horizontal Gas–Liquid Flow in Continuous Casting Using Dynamic Subgrid-Scale Model. *Metallurgical and Materials Transactions B* **2017**, 10.1007/s11663-017-0947-3, doi:10.1007/s11663-017-0947-3.

29. Mistrangelo, C.; Bühler, L. Magnetohydrodynamic flows in liquid metal blankets for fusion reactors. *PAMM* **2017**, *17*, 115-118, doi:https://doi.org/10.1002/pamm.201710033.

30. Murawski, K. Numerical solutions of magnetohydrodynamic equations. *Bulletin of the Polish Academy of Sciences. Technical Sciences* **2011**, *59*, doi:10.2478/v10175-011-0027-9.

31. Zahm, A.F. Flow and Drag Formulas for Simple Quadrics, report,. *University of North Texas Libraries, UNT Digital Library,* **1979**.

---

i